ABSTRACT

Title of Thesis: CFD Analysis of a Slatted
UH-60 Rotor in Hover

Degree Candidate: Yashwanth Ram Ganti

Degree and Year: Master of Science, 2012

Thesis directed by: Associate Professor James D. Baeder
Department of Aerospace Engineering

The effect of leading-edge slats (LE) on the performance of a UH-60A rotor in hover was studied using the OverTURNS CFD solver. The objective of the study was to quantify the effect of LE slats on the hover stall boundary and analyze the reasons for any potential improvement/penalty. CFD predictions of 2-D slatted airfoil aerodynamics were validated against available wind tunnel measurements for steady angle of attack variations. The 3-D CFD framework was validated by comparing predictions for the baseline UH-60A rotor against available experimental values. Subsequent computations were performed on a slatted UH-60A rotor blade with a 40%-span slatted airfoil section and two different slat configurations. The effect of the slat root and tip vortices as they convect over the main blade element was captured using appropriately refined main element meshes and their impact on the slatted rotor performance was analyzed. It was found that the accurate capture of the slat root and tip vortices using the refined meshes made a significant difference to the performance predictions for the slatted rotors. The calculations

were performed over a range of thrust values and it was observed that the slatted rotor incurred a slight performance penalty at lower thrust and was comparable to the baseline rotor at higher thrust conditions. It was also found that shock induced separation near the blade tip was the limiting factor for the baseline UH-60 rotor in hover, causing an increase in rotor power and resulting in a reduction of figure of merit for the baseline rotor at higher thrust values. The shock induced separation occured outboard of the slat tip and therefore limited the performance of the slatted rotors as well. Overall, the study provides useful insights into effects of leading edge slats on rotor hover performance, aerodynamics and wake behavior.

CFD Analysis of a Slatted UH-60 Rotor in Hover

by

Yashwanth Ram Ganti

Thesis submitted to the Faculty of the Graduate School of the
University of Maryland, College Park in partial fulfillment
of the requirements for the degree of
Masters of Science
2012

Advisory Committee:

Associate Professor James D. Baeder Chairman/Advisor
Professor Inderjit Chopra
Professor Sung Lee

Acknowledgments

First, I would like to express my deepest gratitude to my advisor, Dr. James Baeder, for his valuable suggestions and continued guidance throughout the course of this work. His intellectual prowess combined with seemingly infinite patience and a very scientific approach towards research have served as a constant inspiration throughout the course of my graduate studies and I will deeply cherish the experience of working under him for the rest of my life. I would also like to thank my committee members, Dr. Inderjit Chopra and Dr. Sung Lee for their contributions to this thesis.

Special thanks to Shivaji Medida for his suggestions, guidance and support during the course of this work. I am grateful to Dr. Asitav Mishra for helping me with the usage of the CFD solver. I would also like to mention the help that I received from Dr. Shreyas Ananthan and Dr. Vinod Lakshminarayanan on understanding the working details of the OverTURNS solver. Sebastian and Ananth have always been around for a discussion and I have thoroughly enjoyed their company. I have been fortunate to befriend many remarkable individuals during my stay at UMD. I would like to thank Mathieu, Taran, Pranay, Sid, Bharath and Debo for their friendship and support. In addition, I would also like to thank my friends Megha, Anu and Sruthi for their unflinching support during times thick and thin.

Finally, this acknowledgment would not be complete without the mention of my family back home in India, who have been a constant source of love and support.

Table of Contents

List of Tables

List of Figures

NOMENCLATURE

a	Speed of sound, ft s^{-1}
A	Rotor disk area, πR^2, ft^2
c	Rotor chord, ft
C_D	2-D drag coefficient
C_{d_0}	Profile drag coefficient
C_L	2-D lift coefficient
C_M	2-D pitching moment coefficient
C_N	Blade normal force coefficient
C_P	Pressure coefficient
C_T	Rotor thrust coefficient, $T/(\rho A \Omega^2 R^2)$
C_Q	Rotor shaft torque coefficient, $Q/(\rho A \Omega^2 R^3)$
FM	Rotor Figure of Merit, $\frac{C_T^{3/2}}{sqrt(2)C_Q}$
N_b	Number of blades
r	Radial distance of a rotor spanwise station, ft
R	Rotor radius, ft
Re	Reynolds number, Vc/ν
V	Velocity, ft s^{-1}
u_t	Tangential velocity, ft s^{-1}
U_∞	Freestream velocity, ft s^{-1}
M	Mach number, V/a
M_∞	Freestream Mach number, U_∞/a
α	Sectional angle of attack, deg
α_s	Shaft tilt angle, deg
θ_0	Collective pitch, deg
θ_{1c}, θ_{1s}	Lateral and longitudinal cyclic, deg
μ	Advance ratio, $V_\infty/\Omega R$
ν	Kinematic viscosity, ft^{2}s^{-1}

ρ	Flow density, slugs ft^{-3}
σ	Rotor solidity, $N_b c / \pi R$
ψ	Azimuth angle, deg
Ω	Rotor rotational speed, rad s^{-1}
CFD	Computational Fluid Dynamics
CSD	Computational Structural Dynamics
DS	Dynamic Stall
LE	Leading Edge
TE	Trailing Edge

Chapter 1

Introduction

Enhancing rotorcraft performance over a wide range of flight conditions is a challenge that designers are constantly looking to address. The requirements from the next generation of rotorcraft include an increase in payload, range and endurance and a reduction in fuel consumption while being more maneuverable compared to the present generation of rotary wing vehicles. These requirements translate into an increase in the maximum available thrust from the rotor and an increase in rotor efficiency (Lift-to-Drag L/D ratio). Existing rotors are designed to provide a balance between forward flight and hover performance, with hover being one of the unique capabilities of rotorcraft. The factors limiting rotor performance can be different in hover and forward flight. For example, to take off and hover at high altitudes, there would be a demand for higher maximum lift from the rotor. On the other hand, there is a large disparity in the flow environments encountered on the advancing and retreating sides of a rotor in forward flight, as shown in Fig. 1.1.

The advancing side of the rotor operates in a high-speed low angle of attack regime while the retreating side experiences operates in a low-speed high angle of attack environment. For efficient operation, the advancing side requires thinner blade sections for a low profile drag coefficient (C_{d_0}), which is strongly influenced by transonic/compressible effects. To balance the advancing blade lift, the retreat-
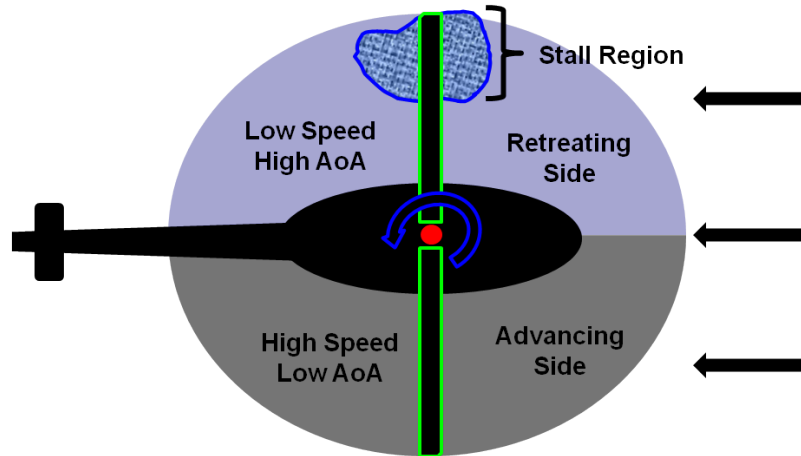
Fig. 1.1: Contrasting flow conditions on the advancing and retreating sides of a rotor disk

ing blade requires thicker airfoil sections, which are capable of sustaining larger maximum lift coefficient ($C_{L_{max}}$) values and therefore are limited by the airfoil stall characteristics. The retreating blade stall has significant implications on rotorcraft performance with the increased drag in the stall regime imposing a large performance penalty. In addition, the large increase in nose-down pitching moment gives rise to larger sectional torsional loads which are transmitted to the pitch-link and cause fatigue which can possibly result in failure.

The problem of relating airfoil sectional characteristics to rotor thrust capability has received considerable attention in the literature. McHugh [2] measured the thrust limits on a 10-foot diameter CH-47B model rotor in the Boeing 20-by-20 ft V/STOL wind tunnel. The rotor lifting limit was determined to be caused by blade stall. Fig. 1.2 is an example figure showing the thrust limits for a UH-60A rotor across a range of flight speeds. The arrow indicates the change in rotor thrust with

increasing collective angle at a given flight speed and the thrust limit of the rotor is called the McHugh's Stall Boundary. In addition, the changes in the rotor flow environment on the advancing and retreating sides require relating the rotor thrust limits to not only the static airfoil properties but also to the unsteady or dynamic component of lift caused by the periodic variation in local angle of attack. This was recognized by McCloud and McCullough [3], who found in their tests of a full scale H-21 rotor that a rotor can provide more thrust than that which would be calculated using the maximum static lift coefficient of the constituent airfoil sections. In addition, they also found that a second rotor which had airfoil sections with a higher $C_{L_{max}}$ provided a higher thrust compared to the first rotor thus establishing a relationship between the static characteristics of an airfoil and the dynamic lifting properties of a rotor.
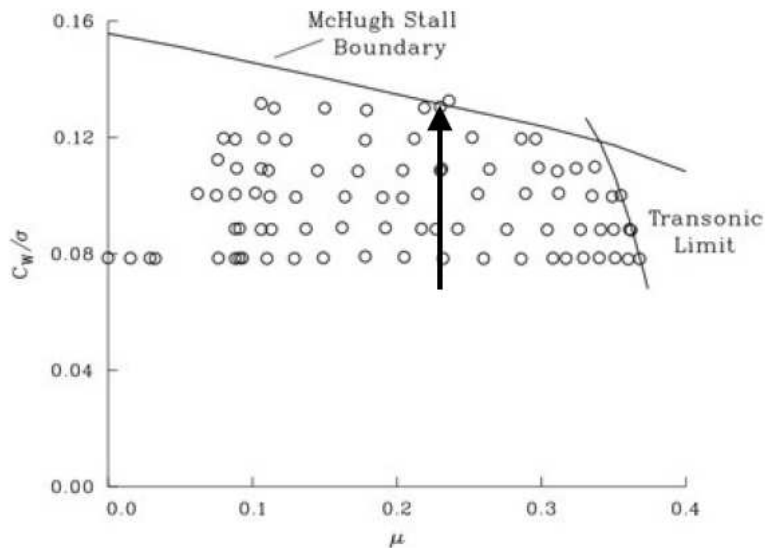
Fig. 1.2: Thrust limits for a UH-60A Rotor [1]

The stall arising on the retreating side of the rotor due to the unsteady changes

3

in angle of attack across a rotor revolution is called Dynamic Stall (DS) and has been the subject of extensive studies over the past 50 years. The book by Leishman [4] provides a detailed explanation of the phenomenon. McCroskey and colleagues [5, 6, 7] performed extensive wind tunnel tests to determine the DS characteristics of eight different airfoil sections. Bousman [1] used this test data to better understand the airfoil design characteristics and flow parameters affecting augmented lift in dynamic stall and the associated drag and moment penalties. Based on the obtained results he observed that all the single element airfoils showed similar DS characteristics and that substantial improvements using single element airfoils would be very hard to achieve. Limited experimental and analytical testing of multi-element airfoils showed potential for increased lift without a significant drag or moment penalty.

Various concepts have been proposed over the years for the purpose of alleviating the various adverse effects associated with DS. Some of these concepts focused on obtaining better lift characteristics while some tried to address the problem of reducing the pitching moment. Martin et al. [8] conducted 2-D wind tunnel and CFD tests on a Variable Droop Leading Edge (VDLE) VR-12 airfoil section and demonstrated a decrease in the drag and pitching moment associated with severe dynamic stall. Chandrasekhara et al. [9] and Sahin et al. [10] analyzed the potential benefits of a Dynamically Deforming Leading Edge (DDLE), the former using wind tunnel measurements and the latter using a compressible 2-D Navier-Stokes solver. Flow control using pulsating jets [11] and leading-edge suction [12] have also been studied to mitigate some of the adverse effects of dynamic stall. Actively controlled blade element concepts such as Trailing Edge Flaps (TEF) have also been studied

extensively for rotorcraft applications [13, 14, 15], using both experimental and computational techniques. The TEF is an attractive concept because of its high control authority and low actuation power but its contribution to militating dynamic stall is limited because of the indirect effect on leading edge aerodynamics since TEFs affect DS by either modifying the trajectory of the DS vortex or by changing the elastic twist through a moment effect. One additional multi-element airfoil concept that has been proposed is an airfoil with Leading Edge Slats and the current work focuses on analyzing LE slats as applied to a hovering rotor. The aerodynamics of LE slats and some of the previous work on applying LE slats to rotorcraft blades will be discussed in the upcoming sections.

1.1   Leading Edge Slats

Leading Edge Slats are used extensively on fixed-wing aircraft to improve the maximum lift coefficient at low speeds. LE slats with their ability to delay stall and increase the value of the maximum lift coefficient can be expected to meet the twin objectives of achieving higher thrust values to help take-off at high altitudes, while working within the available power limits and a reduction in structural loads occurring due to retreating blade stall. To better understand the working of the LE slat as a high-lift device, it is worthwhile to understand the flow physics associated with multi-element airfoils.

1.1.1 Multi-Element Airfoil Flow Physics

In his seminal review paper [16], A.M.O. Smith postulated that a multi-element airfoil would always produce more lift compared to a single element airfoil. To be more general, he stated that "an airfoil with n+1 elements would always produce more compared to an airfoil with n elements". In addition, he also identified five major effects of the slat-main element gap (or) slot. Three of these are inviscid effects and two are viscous effects and are explained briefly in this section.

1. Slat effect (inviscid)

2. Circulation effect (inviscid)

3. Dumping effect (inviscid)

4. Off-surface pressure recovery effect (viscous)

5. Fresh boundary layer effect (viscous)

The inviscid effects can be visualized easily if every lift producing element were to be replaced using a point vortex (neglecting thickness effects), similar to thin-airfoil theory, as shown in Fig. 1.3. The *Slat effect* from the forward element causes a reduction in the effective flow angle at the LE of the downstream element due to the induced effect of the point vortex. This reduces the pressure peak on the downstream element and protects it from separation. Similarly, the *Circulation effect* is due to the point vortex of the downstream element causing a larger flow angle at the TE of the upstream element. The *Kutta Condition* which requires the flow to leave the

TE smoothly results in a larger value for the circulation on the upstream element and hence larger lift. Closely related to the *Circulation effect* is the third inviscid effect, the *Dumping effect*: because the trailing edge of an upstream element is in a region of velocity higher than the freestream, there is a higher discharge velocity of the boundary layer into the wake than there would be if there were no downstream elements present. This higher velocity reduces the pressure rise impressed on the boundary layer and reduces the likelihood of separation.
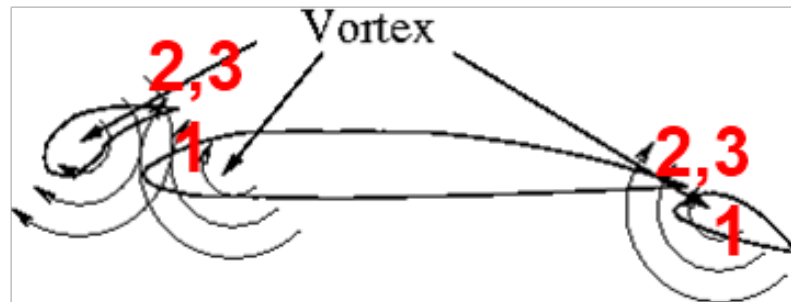
Fig. 1.3: Inviscid effects on a Multi-Element Airfoil

The first viscous effect is the *off-surface pressure recovery* states that wakes can withstand larger adverse pressure gradients compared to boundary layers. The BL on the slat leaves the trailing edge at a velocity higher than the freestream and becomes a wake and the recovery back to freestream conditions is more efficient away from contact with a wall. The *Fresh Boundary Layer effect* simply states that multiple thin boundary layers are better than a single thick one, since thin boundary layers can sustain larger pressure gradients than thicker ones. The work of A.M.O Smith was instrumental in explaining the physics behind the working of multi-element airfoils, especially LE slats. Indeed, such configurations have been in

existence on fixed wing aircraft from as early as the 1920s. The next section looks at some of the previous efforts to incorporate LE slats onto rotorcraft blades.

1.1.2   Previous Work on LE Slats for Rotorcraft Applications

Early studies [17, 18] using a NACA15320 slat on a VR-7 airfoil (Fig. 1.4(a)) showed an improvement in the steady lift and reduction in dynamic stall hysteresis over the single element but the tests also showed an increased drag penalty for the slatted airfoil at low angles of attack. Noonan et al [19] investigated the effects of using two slotted configurations (C106 and C210) (shown in Fig. 1.4(b)) on a RC(6)-08 tip airfoil. The tests were conducted across a range of Mach numbers (0.20-0.88). Comparing their results against a transonic code, they found a 29-61% increase in the maximum lift over the baseline single element airfoil, but also a 150% increase in the drag. These slatted airfoils were then applied to the 85-100% radius region of a model HIMARCS-I rotor, which was tested in the NASA Langley TDT [20]. The results showed a 15-25% increase in the stall boundary, accompanied by power reductions at higher thrust and advance ratios but a 10-20% power penalty at lower thrust values. Carr et al. [21] conducted extensive tests to determine the effects on compressibility on the suppression on dynamic stall using the above slatted configuations.

The problem of alleviating the drag penalty for a slatted airfoil at lower lift values was addressed through computational design and optimization studies. Narramore et al. [22] combined a potential flow/integral boundary layer solver and an
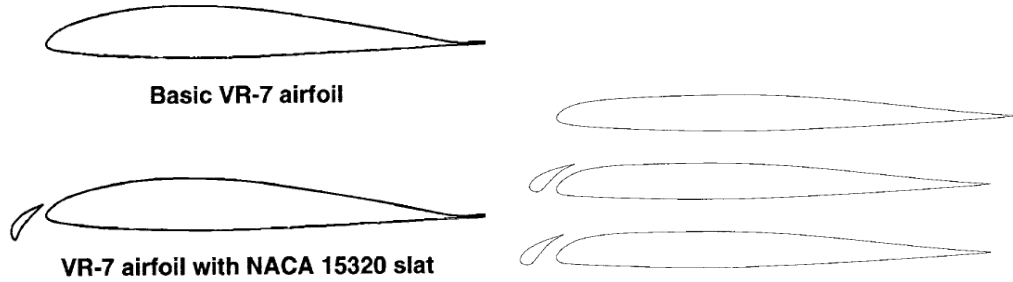
(a) NACA 15320 Slat on a VR-7 Airfoil [17] (b) Top: RC(6)-08 baseline airfoil. Middle: C106 slat. Bottom : C210 slat [21]

Fig. 1.4: Early slatted configurations for rotorcraft applications

inverse design tool to develop new slatted airfoil geometries. The C106 slat mentioned earlier was used as the starting point for the inverse design study and the new slatted configuration called the A3C (Fig. 1.5) was the output. Analysis of the new design using the OVERFLOW [23] code showed a 3% increase in maximum lift and a 47% decrease in the minimum drag over the C106 slat. This new configuration was applied to a UH-60A rotor and analyzed using the comprehensive code CAMRAD [24] and demonstrated a 25% increase in the maximum thrust but still incurred a significant power penalty at low thrust conditions.

More recently, researchers at Sikorsky and United Technologies Research Center (UTRC) designed several slat configurations with the aid of CFD analysis [25]. The slatted airfoil used was the aforementioned A3C airfoil and Navier-Stokes optimization studies were conducted with the slat position (x, y) and the angle of the slat relative to the main-element as the design variables. The objective functions chosen were $C_{L_{max}}$ at $M = 0.35$ and C_{D_0} at $M = 0.7$, indicative of the need to

maximize lift on the retreating side of a rotor and to minimize the drag on the advancing side. A second study was conducted to tailor the shape of the main-element airfoil in the vicinity of the leading 1/4 chord region. The starting shape was the SC1094R8 airfoil used in the mid-span region of the UH-60A rotor blade. Two of the slat configurations, the so-called S-1 and S-6 and the new airfoil section, the SC2110, are shown in Fig. 1.6, along with the original SC1094R8 section. The S-1 slat had the lowest drag while the S-6 slat had the highest maximum lift coefficient. These configurations were then applied to a model rotor from 50% to 90% radius locations and tested in the NASA Langely Trasonic Dynamic Tunnel (TDT) [26] and the results were compared against those from a comprehensive analysis code. Results indicated an increase in the rotor stall boundary but a decrease in the effective rotor L/D_e due to increased drag at the lower thrust conditions. The performance of the slatted rotor was compared against the model baseline rotor at advance ratios of μ = 0.30 and 0.38 respectively.

Mishra [27] built upon the UTRC study using a coupled CFD-CSD method-
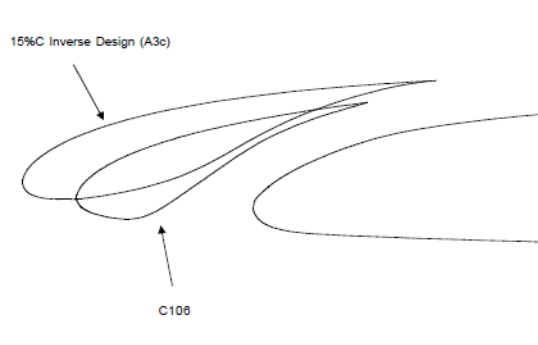
Fig. 1.5: Optimization of LE Slats to reduce drag [24]
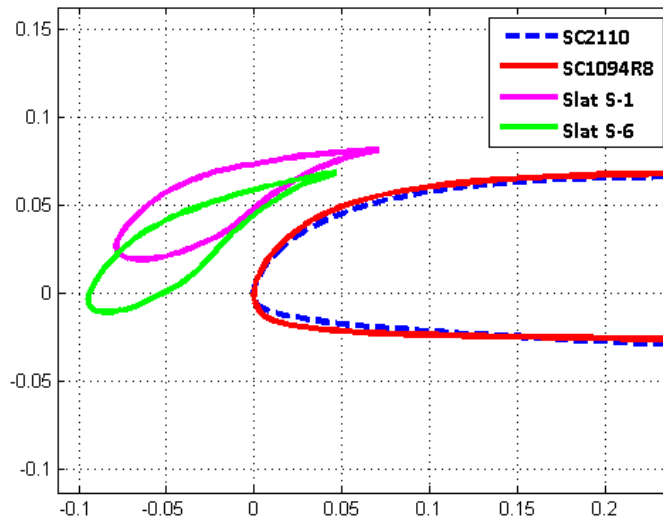
Fig. 1.6: S-1 and S-6 slat configurations [25]

ology to analyze the performance of the above mentioned slatted configurations, applied to a UH-60A rotor operating in a high-altitude, high-thrust flight condition (Counter C9017 in the UH-60A Airloads database [28]). Moving slat configurations, with the slat at different positions on the advancing and retreating positions were explored. Results showed an improvement in the alleviation of dynamic stall and a reduction in the vibratory loads.

1.2 Motivation

From the discussion so far, it is clear that LE slats represent an attractive proposition to mitigate some of the adverse effects associated with the phenomenon of Dynamic Stall. Most of the experimental and analytical studies have therefore focused on forward flight performance of LE slat, where dynamic stall is one of

11

the limiting phenomena. Hover is a capability which is unique to rotorcraft and represents an equally important flight condition which merits thorough analysis. Traditional analysis methodologies rely on simple aerodynamic models which use some form of table lookup to compute the aerodynamic coefficients. These type of analyses are widely used in industry primarily because of their low computational cost and quick turnaround time. However, while analyzing relatively less studied and exotic configurations such as LE slats, a high fidelity method, which more accurately captures the effect of these configurations on rotor and wake aerodynamics should be employed. A CFD solver, which computes the flow field from first principles by solving the Navier-Stokes equations is generally the tool of choice.

1.3 Previous Work on the UH-60A Rotor in Hover

1.3.1 Experimental Work and Flight Testing

The UH-60A rotor is among the most analyzed in the history of rotorcraft, as indeed is the UH-60A helicopter. During the 1980s, NASA and the U.S Army put together a plan for multiple rotor tests with extensive airload measurements on the blades. The program was envisioned in three stages, the first comprising of model scale rotor tests, the second a full scale flight test of the rotor and the third being the same rotor tested in a wind tunnel. The full scale UH-60 was tested in flight 1993-94 and the results are a part of what is now called the UH-60 Airloads Database [28, 29]. Prior to the flight test, as a part of the model rotor test program, Lorber et al. [30] conducted experiments on a 17.5% scale model under

hovering conditions in the Sikorsky model rotor hover test facility. Measured quantities included detailed wake flow visualization and extensive blade surface pressure measurements along with the usual balance measurements for rotor performance. This same model rotor was later tested in the German-Dutch wind tunnel (Duits-Nederlandse Windtunnel;DNW) [31], both in hover and at several advance ratios. Shinoda et al. [32] conducted hover tests of a full scale UH-60A rotor in the NASA Ames 80-by-120 Foot Wind Tunnel, with the rotor blades mounted on the Large Rotor Test Apparatus (LRTA). Prior to the airloads program flight tests, the U.S Army Aviation Engineering Flight Activity (AEFA) conducted hover and forward flight tests at Edwards AFB, on different UH-60A aircraft, with each aircraft corresponding to a different production year. Most recently [33], NASA and the U.S. Army completed a full-scale wind tunnel test of the UH-60A airloads rotor, including the pressure-instrumented blade. This test, conducted in the USAF National Full-Scale Aerodynamics Complex (NFAC) 40- by 80-Foot Wind Tunnel, was designed to produce unique data not available from the flight test. Overall, these experiments and flight tests provide a valuable database for researchers to validate the different analysis tools.

1.3.2 Computational Work

Early computational models [34] used a simplified set of equations, such at the potential flow equations, to model the complex flow field of a lifting helicopter rotor. This was followed by the use of the Euler equations [35] and with increase

in computational power, codes which solved the Navier-Stokes equations [36]. A common strand to all these solution schemes was the use of wake models to compute the induced effects of the rotor and these methods are also referred to as wake-coupled methods. The influence of the rotor wake on the near-blade flow is much larger in hover compared to a forward flight condition because the wake is not convected away as rapidly. Recognizing this, the next set of solution procedures, instead of using ad-hoc wake models, attempted to compute the induced effects of the vortex wake as a part of the overall flow field solution. Such methods are also referred to as wake capturing schemes. Some of the early efforts at wake capturing using a Navier-Stokes analysis include [37] and [38], using the Transonic Unsteady Navier-Stokes (TURNS) solver. The first fairly complete CFD validation effort using the data from [30] was by Baeder and Wake [39], who used the TURNS code and showed promising inboard loading comparisons but the predictions of the tip loads and wake geometry compared relatively poorly. Also, they used a single mesh system ranging from 380,000 - 950,000 points, which is considered coarse by modern day standards. More recently, Strawn and Ahmad [40] and Strawn and Djomehri [41] used a version of the RANS solver, OVERFLOW [23] with structured overset grids to compute the flow field. High resolution meshes were applied near the blade and there was a systematic variation of grid resolution near the rotor wake. The mesh systems used ranged from 10.6-64 million points. The comparisons with experiment were better compared to earlier efforts and it was noted that the solution exhibited little sensitivity to grid resolution. The tip loading however was slightly over-predicted and this was attributed to the miss distance of the first returning

14

vortex, which was shown to be passing $0.2c$ under the blade compared to about $0.4c$ in the experiments.

The prediction of hover performance, quantified in terms of rotor figure-of-merit (FM), is essential in the design of all rotorcraft. Predicting FM with a discrepancy of less than 0.02 is generally considered to be within engineering accuracy and a more realistic requirement in some phases of the rotor design, for example, weight prediction, would be a 0.01 variation in FM. None of the above mentioned analyses have been able to consistently achieve this level of predictive accuracy. One possible reason for this could be the uncertainty in the experimental data itself, in addition to the inherent limitations of the individual analysis methods. Shinoda et al. [32] summarized a comparison of several hover performance measurements, as shown in Fig. 1.7. It can be seen that there are deviations in two successive model scale experiments, where an almost identical set up was tested in two different wind tunnels. Most of the analyses compare against the model rotor tests because they are free from the extraneous factors affecting flight tests such as cross winds and also in case of the tethered hover tests, only the total engine power was available and some empirical factors were needed to isolate the rotor power.

There is very limited experimental data available for slatted rotors under hovering conditions. In the experiments of Noonan et al. [20], the slatted rotors were tested under hovering conditions at a tip Mach number of 0.627. Results showed that the slatted rotor with the slat in a moderate nose down position, referred to as the $-6°$ slat performed better than the baseline rotor at higher thrust conditions whereas the slatted rotor with the slat in the most nose down position, referred to as
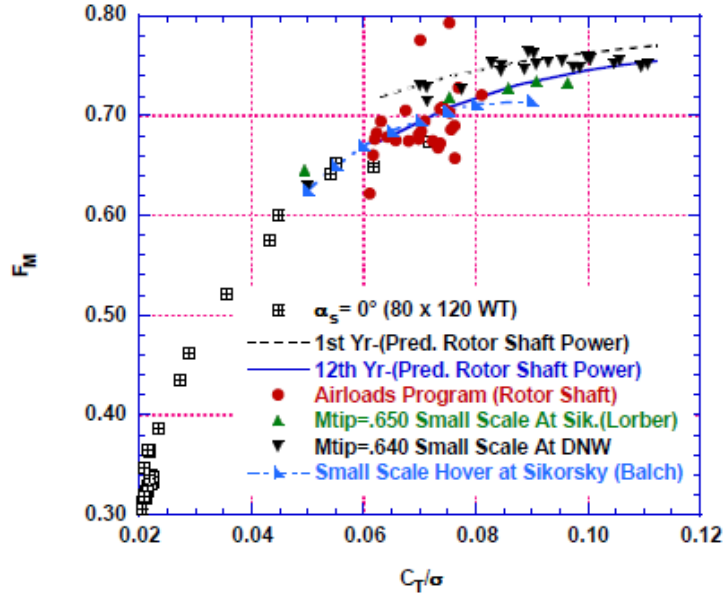
Fig. 1.7: UH-60A rotor hover FM from three full-scale helicopter tests and three model-scale rotor experiments [32]

the $-10°$ slat had the poorest performance amongst all three rotor across the thrust range. The results however might have been influenced by re-circulation effects, since the bottom wall of the wind tunnel was at a distance $z/d = 0.83$ below the rotor, where d is the rotor diameter. In addition, there was no spanwise or chordwise loading data available due to the lack of instrumentation on the rotor.

1.4 Objective

The focus of the current research is to use a high-fidelity CFD analysis to study the effects of LE slats on the performance of a UH-60A rotor in hover. The potential benefits of using LE slats to mitigate dynamic stall and expand the flight

envelope in forward flight conditions have been demonstrated in previous studies, however the hover performance of these configurations has not been quantified so far. The airfoil sections on a rotor in hover do not operate close to their static stall angle of attack values and hence the slatted rotors are not expected to provide a large improvement in the rotor lifting capability. However, it is also known that at small angles of attack, the slatted configurations incur a drag penalty, especially at higher Mach numbers, as one would encounter while moving outboard towards the tip of the rotor blade. It would be necessary to quantify this performance penalty, if any, accurately using a high-fidelity analysis tool.

Before attempting to study the slatted configurations, the existing CFD methodology is validated against the baseline UH-60A model rotor experiments described earlier. The 2-D CFD methodology is also validated against existing wind tunnel results and the flow around the slatted airfoils at low angles of attack is studied in greater details. Also, one additional drawback of previous analyses has been their inability to resolve the slat edge effects. The slat in the flow field with a finite span would generate its own root and tip vortices which would then convect over the main blade element. Modeling a slat through 2-D airfoil tables or not having adequate resolution in the mesh system in a Navier-Stokes analysis does not capture these edge effects accurately. In the present work, appropriately refined main blade element meshes are generated to capture these slat root and tip vortices and were found to have a significant impact on the performance predictions.

1.5   Organization of Thesis

The present work attempts to quantify the performance of a slatted UH-60A rotor and compare it against the baseline UH-60A rotor predictions. The present chapter described the motivation behind using LE slats on rotorcraft and also gave a background of general multi-element flow physics. Some of the previous work, both experimental and analytical, pertaining to hovering rotors was also presented. Chapter 2 described the CFD solution methodology used in this research, including the use of overset meshes for efficient wake capturing. Chapter 3 presents the validation studies, beginning with the comparison of 2-D CFD prediction of slatted airfoil sections against wind tunnel experiments, followed by the validation of the 3-D CFD framework against model scale experiments of a hovering UH-60A rotor. The results from the slatted rotor simulations using the validated CFD solver are described in Chapter 4. Detailed airloads and wake comparisons are made with the baseline UH-60A rotor and the effect of mesh refinement on the slatted rotor performance is also study. Chapter 5 summarizes some of the major observations of the present work and concludes with a discussion of some future work that can be undertaken to further understand the slatted rotor concept.

Chapter 2

Methodology

Computational Fluid Dynamics (CFD) is a powerful tool to analyze both existing and new rotorcraft configurations and can be used for detailed flow visualization and performance prediction studies around such configurations. Before using a CFD solver to analyze new configurations, it should be validated against existing experimental studies for the purpose of establishing confidence in the predicted values. This chapter details the CFD solution methodology used in the current work.

2.1 Governing Equations of Fluid Motion

The governing equations of fluid motion used in this work are the three-dimensional Navier-Stokes (NS) equations. The equations are discretized and solved at finite points on a computational grid, which is generated prior to the solution process. Initial and boundary conditions appropriate to the geometry and problem in consideration are applied during the solution process.

2.1.1 Navier-Stokes Equations

The Navier-Stokes equations are the fundamental partial differential equations (PDEs) which govern fluid motion. They are the mathematical representation of the three conservation laws of physics, i.e. conservations of mass, momentum and energy.

The Navier-Stokes equations in the strong conservation law form and Cartesian coordinates can be written as:

$$\frac{\partial Q}{\partial t} + \frac{\partial F_i}{\partial x} + \frac{\partial G_i}{\partial y} + \frac{\partial H_i}{\partial z} = \frac{\partial F_v}{\partial x} + \frac{\partial G_v}{\partial y} + \frac{\partial H_v}{\partial z} + S \qquad (2.1)$$

where Q is the vector of the conserved variables and vectors F_i, G_i and H_i are vectors of inviscid fluxes in each of the three coordinate directions. F_v, G_v and H_v represent the viscous fluxes and S is the vector of source terms that account for the centrifugal and Coriolis accelerations if the equations are formulated in a non-inertial frame of reference. The vector of conserved variables is given by

$$Q = \left\{ \begin{array}{c} \rho \\ \rho u \\ \rho v \\ \rho w \\ e \end{array} \right\} \qquad (2.2)$$

where ρ is the density, (u, v, w) are the Cartesian velocity components and e is the total energy per unit volume. The flux vectors are given by

$$F_i = \begin{Bmatrix} \rho u \\ \rho u^2 + p \\ \rho uv \\ \rho uw \\ u(e+p) \end{Bmatrix} \qquad (2.3)$$

$$G_i = \begin{Bmatrix} \rho v \\ \rho vu \\ \rho v^2 + p \\ \rho vw \\ v(e+p) \end{Bmatrix} \qquad (2.4)$$

$$H_i = \begin{Bmatrix} \rho w \\ \rho wu \\ \rho wv \\ \rho w^2 + p \\ w(e+p) \end{Bmatrix} \qquad (2.5)$$

$$F_v = \begin{Bmatrix} 0 \\ \tau_{xx} \\ \tau_{yx} \\ \tau_{zx} \\ u\tau_{xx} + v\tau_{xy} + w\tau_{xz} - q_x \end{Bmatrix} \qquad (2.6)$$

$$G_v = \left\{ \begin{array}{c} 0 \\[6pt] \tau_{xy} \\[6pt] \tau_{yy} \\[6pt] \tau_{zy} \\[6pt] u\tau_{yx} + v\tau_{yy} + w\tau_{yz} - q_y \end{array} \right\} \tag{2.7}$$

$$H_v = \left\{ \begin{array}{c} 0 \\[6pt] \tau_{xz} \\[6pt] \tau_{yz} \\[6pt] \tau_{zz} \\[6pt] u\tau_{zx} + v\tau_{zy} + w\tau_{zz} - q_z \end{array} \right\} \tag{2.8}$$

where q_x, q_y and q_z are the thermal conduction terms, which can be represented in terms of temperature (T) and coefficient of thermal conductivity (k), given by:

$$q_i = -k\frac{\partial T}{\partial x_i} \tag{2.9}$$

The pressure (p) is determined by the equation of state for a perfect gas, given by

$$p = (\gamma - 1)\left\{ e - \frac{1}{2}\rho(u^2 + v^2 + w^2) \right\} \tag{2.10}$$

where γ is the ratio of specific heats, generally taken as 1.4. For a perfect gas, $T = \frac{p}{\rho R}$, where R is the gas constant. With the assumption of Stokes' hypothesis [42], the mean stresses can be represented by:

22

$$\tau_{ij} = \mu \left[\left(\frac{\partial u_i}{\partial x_j} + \frac{\partial u_j}{\partial x_i} \right) - \frac{2}{3} \frac{\partial u_k}{\partial x_k} \delta_{ij} \right] \tag{2.11}$$

where μ is the laminar viscosity, which can be evaluated using simple algebraic Sutherland's Law [42].

2.1.1.1 Non-dimensionalization of the Navier-Stokes Equations

The equations of fluid motion are non-dimensionalized to provide solutions which have dynamic and energetic similarity for geometrically similar situations. The solutions therefore would be exactly the same for two cases with the same initial and boundary conditions and where the non-dimensional values of the dynamic and energetic parameters describing the flow are the same. The solutions thus obtained are of the order of one. Generally, a characteristic dimension of the flow, such as the chord of the airfoil is selected to non-dimensionalize the length scale. The non-dimensional variables (denoted by superscript $*$) are given below:

$$
\begin{aligned}
t^* &= \frac{t a_\infty}{c} & x^* &= \frac{x}{c} & y^* &= \frac{y}{c} & z^* &= \frac{z}{c} \\
\mu^* &= \frac{\mu}{\mu_\infty} & u^* &= \frac{u}{a_\infty} & v^* &= \frac{v}{a_\infty} & w^* &= \frac{w}{a_\infty} \\
\rho^* &= \frac{\rho}{\rho_\infty} & T^* &= \frac{T}{T_\infty} & p^* &= \frac{p}{\rho_\infty a_\infty^2} & e^* &= \frac{e}{\rho_\infty a_\infty^2}
\end{aligned}
\tag{2.12}
$$

where c is the chord of the airfoil, a is the speed of sound and subscript ∞ represents free-stream condition.

The non-dimensional parameters describing the flow are:

$$\text{Reynolds Number :} \qquad Re_\infty = \frac{\rho_\infty V_\infty c}{\mu_\infty}$$

$$\text{Mach Number :} \qquad M_\infty = \frac{V_\infty}{a_\infty}$$

$$\text{Prandl Number :} \qquad Pr = \frac{\mu C_p}{k} \qquad (2.13)$$

where C_p is the specific heat at constant pressure. For all computations in this work, $Pr = 0.72$ is assumed. V_∞ is the free-stream total velocity given by $\sqrt{u_\infty^2 + v_\infty^2 + w_\infty^2}$.

The Navier-Stokes equations in non-dimensional form can again be represented as eqn. 2.1, if the superscript $*$ is ignored. The non-dimensional inviscid and viscous flux terms will also have identical form as before. Differences arise in the non-dimensional stress and conduction terms, which now become a function of the non-dimensional parameters (Reynolds number and Prandtl number). Neglecting the superscript $*$, the non-dimensional mean stresses and thermal conduction terms, respectively, are given by:

$$\tau_{ij} = \frac{\mu M_\infty}{Re_\infty} \left[\left(\frac{\partial u_i}{\partial x_j} + \frac{\partial u_j}{\partial x_i} \right) - \frac{2}{3} \frac{\partial u_k}{\partial x_k} \delta_{ij} \right] \qquad (2.14)$$

$$q_i = -\frac{\mu M_\infty}{Re_\infty Pr(\gamma - 1)} \frac{\partial T}{\partial x_i} \qquad (2.15)$$

2.1.1.2 Equations in a Rotating Reference Frame

The governing equations, usually solved in the inertial reference frame, can alternatively be solved in a non-inertial reference frame. Although choosing non-

inertial over inertial reference frame has significant advantages in hover calculations [43, 44], it can have noticeable impact on solution convergence even in forward flight calculations. One additional advantage of solving the equations in a rotating reference frame is that the grid metrics need to be calculated only once at the start of the solution process. To account for a non-inertial reference frame, the fluxes in eqn. 2.1 become:

$$
F_i = \left\{ \begin{array}{c} \rho(u - u_g) \\ \rho u(u - u_g) + p \\ \rho(u - u_g)v \\ \rho(u - u_g)w \\ (u - u_g)(e + p) \end{array} \right\}
\tag{2.16}
$$

$$
G_i = \left\{ \begin{array}{c} \rho(v - v_g) \\ \rho(v - v_g)u \\ \rho(v - v_g)v + p \\ \rho(v - v_g)w \\ (v - v_g)(e + p) \end{array} \right\}
\tag{2.17}
$$

$$
H_i = \left\{ \begin{array}{c} \rho(w - w_g) \\ \rho(w - w_g)u \\ \rho(w - w_g)v \\ \rho(w - w_g)w + p \\ (w - w_g)(e + p) \end{array} \right\}
\tag{2.18}
$$

25

where, $U = \{u, v, w\}$ is the vector of physical velocities in the inertial frame and $U_g = \{u_g, v_g, w_g\} = \Omega \times r$ is the rotational velocity vector. Ω is the angular velocity vector $\{0, 0, \Omega_z\}$, rotating about z-axis and r is the relative position vector from the axis of rotation. Thus, $U_g = \{-\Omega_z y, \Omega_z x, 0\}$. In addition, the relative acceleration terms (due to Coriolis force) have to be included as a source term vector S in eqn. 2.1:

$$S = \left\{ \begin{array}{c} 0 \\ \rho v \Omega_z \\ -\rho u \Omega_z \\ 0 \\ 0 \end{array} \right\} \tag{2.19}$$

2.1.1.3 Transformation to Generalized Curvilinear Coordinates

The Navier-Stokes equations are generally solved on a finite computational domain or the computational mesh. Cartesian meshes may not represent the most suitable type of a mesh for solving every problem. The governing equations are therefore expressed in strong conservation law form for a general curvilinear coordinate system with the aid of the chain rule of partial derivatives. In effect, the equations after being transformed to the computational coordinates ξ, η, ζ are as follows:

$$\frac{\partial \hat{Q}}{\partial t} + \frac{\partial \hat{F}}{\partial \xi} + \frac{\partial \hat{G}}{\partial \eta} + \frac{\partial \hat{H}}{\partial \zeta} = \hat{S} \tag{2.20}$$

where,

$$\hat{Q} = \frac{1}{J}Q \tag{2.21}$$

$$\hat{F} = \frac{1}{J}\left[\xi_t Q + \xi_x(F_i - F_v) + \xi_y(G_i - G_v) + \xi_z(H_i - H_v)\right] \tag{2.22}$$

$$\hat{G} = \frac{1}{J}\left[\eta_t Q + \eta_x(F_i - F_v) + \eta_y(G_i - G_v) + \eta_z(H_i - H_v)\right] \tag{2.23}$$

$$\hat{H} = \frac{1}{J}\left[\zeta_t Q + \zeta_x(F_i - F_v) + \zeta_y(G_i - G_v) + \zeta_z(H_i - H_v)\right] \tag{2.24}$$

$$\hat{S} = \frac{1}{J}S \tag{2.25}$$

where J is the Jacobian of the coordinate transformation (i.e., $J = det\left(\frac{\partial(\xi,\eta,\zeta)}{\partial(x,y,z)}\right)$)

2.1.2 Reynolds Averaged Navier-Stokes Equations

The governing Navier-Stokes equations 2.20 are sufficient for computing inviscid or laminar flows, but present difficulties in turbulent regimes. Turbulent flows occur in a vast majority of fluid applications encountered in engineering problems, especially in external aerodynamics involving helicopter rotors. Turbulent flow is characterized by chaotic motion of molecules, leading to an increased momentum and energy exchange between the fluid layers as well as between the fluid and the wall.

The most elegant solution to any turbulent flow is through the Direct Numerical Simulation (DNS) of turbulence. Although, the turbulent fluctuations are deterministic in nature, the small spatial scales require a very large number of grid points for adequate resolution. This combined with the small temporal scales puts

the DNS method beyond the scope of most modern day computing systems. A first level of approximation for turbulent flows is achieved using the Large Eddy Simulation (LES) approach. The core idea of LES is that small scales of turbulent motion possess a more universal character than the large scales, which transport the turbulent energy. Thus the idea is to resolve the larger scales and to model the smaller scales and therefore requires lesser number of grid points compared to DNS. However, LES is inherently three dimensional and still computational very expensive and not widely used in engineering practice.

The next level of approximation and most commonly used approach for turbulent flows is the so called Reynolds Averaged Navier-Stokes (RANS) approach, which was presented by Reynolds in 1895. It is based upon the decomposition of the flow variables into mean and fluctuating parts. The motivation behind this is that in most engineering and physical processes, one is only interested in the mean quantities. Therefore, any flow variable, ϕ, can be written as:

$$\phi = \bar{\phi} + \phi'$$ (2.26)

where $\bar{\phi}$ is the mean part and ϕ' is the fluctuating part. The mean part, $\bar{\phi}$, is obtained using Reynolds averaging given by

$$\bar{\phi} = \frac{1}{\bar{\chi}} \lim_{\Delta t \to \infty} \frac{1}{\Delta t} \int_0^{\Delta t} \chi \phi(t) dt$$ (2.27)

where $\chi = 1$, if ϕ is density or pressure and $\chi = \rho$, if ϕ is other variables such as

28

velocity, internal energy, enthalpy and temperature. By definition, the Reynolds average of the fluctuating part is zero.

The decomposed variables are then inserted into the Navier-Stokes equations (eqn. 2.20) and the equations are Reynolds averaged to obtain the mathematical description of the mean flow properties. If the overbar on the mean flow variables is dropped, the resulting equations are identical to the instantaneous Navier-Stokes equations with the exception of additional terms in the momentum equation and the energy equation (not present if heat transfer is neglected). The extra terms in the momentum equation accounts for the additional stress due to turbulence and are called the **Reynolds-stress tensor**. These stresses add to the viscous stress terms given in eqn. 2.11 and are given by:

$$\tau_{ij}^{R} = -\rho \overline{u_i' u_j'} \tag{2.28}$$

However, with the introduction of the Reynolds-stress terms, we obtain six additional unknowns in the Reynolds-averaged momentum equations. In order to close the RANS equations, the Reynolds stress terms are approximated using a turbulence model. Details of turbulence modeling will be briefly discussed in section 2.3.4.

2.2   Initial and Boundary Conditions

The RANS equations described in the previous section are the general equations which are valid for any general problem. To characterize, define and solve a particular problem, the partial differential equations require a set of initial and

boundary conditions. The initial conditions refer to the state of the flow before the start of the solution procedure and the boundary conditions are the physical and numerical conditions imposed at various boundaries within the computational domain. A particular choice or combination of boundary and/or initial conditions can have a considerable influence on the accuracy or even the stability properties of a numerical scheme.

Typically for hover runs, the initial conditions for the fluid properties such as density, pressure and velocity can be set either to the freestream values or to a previously converged state. The two commonly used boundaries conditions for external aerodynamics are the wall and the farfield boundary conditions. Wall boundaries are natural boundaries within the solution domain which arise from solid surfaces being exposed to the flow. For a viscous fluid which passes over such a wall, the relative velocity between the fluid and the wall is zero. The farfield boundary condition is a consequence of the computational domain being finite and therefore certain flow quantities have to be specified at such boundaries. The farfield boundary has to satisfy two basic requirements. The first being that the truncation of the domain should have no notable effect on the flow variables as compared to an infinite domain, the second being that any outgoing disturbances should not be reflected back into the interior of the computational domain. The different boundary condition used in the present work are described in section 2.4
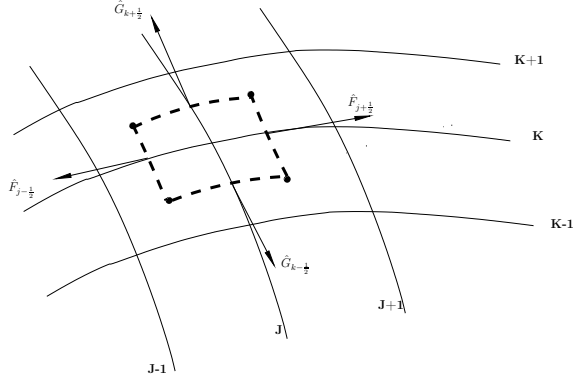
Fig. 2.1: Schematic showing the computational cell

2.3   Numerical Algorithm

Once a computational domain is generated for the problem at hand, the RANS equations are discretized and solved on this domain using a suitable numerical procedure. The solution procedure or solver used in this work is the Overset Transonic Unsteady Navier-Stokes Solver (OverTURNS) [45]. OverTURNS solves the compressible Navier-Stokes equations on two or three dimensional block structured grids. The differential eqn. 2.20 is discretized in space and time in a finite volume approach. In this approach, fictitious volumes are created around each grid point. A fictitious volume is created around a point using the midpoints of the lines joining the adjacent grid points to the grid point, as shown in Fig 2.1. The faces of this new volume lie exactly in the middle of two grid points. This volume is treated as a control volume and fluxes are evaluated at the faces of the volume, resulting in conservation equations for the volume.

The semi-discrete conservative approximation of eqn. 2.20 can be written as:

$$\frac{\partial \hat{Q}}{\partial t} = -\frac{\hat{F}_{j+\frac{1}{2}} - \hat{F}_{j-\frac{1}{2}}}{\Delta \xi} - \frac{\hat{G}_{k+\frac{1}{2}} - \hat{G}_{k-\frac{1}{2}}}{\Delta \eta} - \frac{\hat{H}_{l+\frac{1}{2}} - \hat{H}_{l-\frac{1}{2}}}{\Delta \zeta} + \hat{S}_{j,k,l} \qquad (2.29)$$

where, (j, k, l) are the indices corresponding to the (ξ, η, ζ) directions in the transformed coordinate system and $(j \pm \frac{1}{2}, k \pm \frac{1}{2}, l \pm \frac{1}{2})$ define the cell-interfaces of the control volumes as shown in Fig. 2.1 (2D cell shown for simplicity). The spatial discretization (consisting of the inviscid and viscous fluxes) reduces to evaluating the interface fluxes $\hat{F}_{j+\frac{1}{2}}, \hat{G}_{k+\frac{1}{2}}, \hat{H}_{l+\frac{1}{2}}$ for every cell (j, k, l) in the domain.

2.3.1   Inviscid Terms

The inviscid part of the interface flux is computed using upwind schemes [46]. Upwind schemes have the advantage that the wave propagation property of the inviscid equations is accounted for (albeit approximately) in the flux calculation. To evaluate the interface fluxes, the Monotone Upstream-Centered Scheme for Conservation Laws (MUSCL) [46] approach is used. This procedure involves two steps. First, the left and right states at each interface are reconstructed from the corresponding cells using piecewise cubic reconstruction with Koren's limiter [47]. Next, these right and left states are used to define a local Riemann problem and the interface flux is obtained by using Roe flux difference splitting [48]:

$$F(q^L, q^R) = \frac{F(q^L) + F(q^R)}{2} - |\hat{A}(q^L, q^R)|\frac{q^R - q^L}{2} \qquad (2.30)$$

where $\hat{A}$ is the Roe-averaged Jacobian matrix.

2.3.2   Viscous Terms

In the earlier versions of the OverTURNS code, the thin-layer approximation was used to compute the viscous terms. Under this assumption, the derivatives of the flow quantities in the wall normal direction are the only ones which are considered to be significant and the derivatives in the other two coordinate directions are not considered while computing the viscous stresses. This assumption is valid only for fully attached flows and hence in the present work, the full viscous terms are considered without the thin-layer approximation. Numerical discretization of these terms involve expressions of the form [49]:

$$\frac{\partial}{\partial \xi}\left(\alpha \frac{\partial \beta}{\partial \eta}\right) \tag{2.31}$$

These terms are computed using second order accurate central differencing. Thus, the above expression will be discretized as:

$$\frac{1}{\Delta \xi}\left(\left[\alpha_{j+\frac{1}{2},k}\frac{\beta_{j+\frac{1}{2},k+1}-\beta_{j+\frac{1}{2},k}}{\Delta \eta}\right]-\left[\alpha_{j-\frac{1}{2},k}\frac{\beta_{j-\frac{1}{2},k}-\beta_{j-\frac{1}{2},k-1}}{\Delta \eta}\right]\right) \tag{2.32}$$

where

$$\delta_{j+\frac{1}{2},k}=\frac{\delta_{j,k}+\delta_{j+1,k}}{2}, \qquad (\delta = \alpha, \beta) \tag{2.33}$$

2.3.3 Time Integration

The conservative variables in eqn. 2.29 need to be evolved in time, once the right hand side (RHS) is evaluated. Either explicit or implicit time stepping can be used. The explicit methods use information only from the previous time step(s) (depending on the order of the method) to calculate the conservative variables at the new time step. The implicit methods indirectly used the information at the new time step and require inversion of large spare matrices. Explicit methods however place restrictions on the value of the timestep that can be used based on the mesh size and the flow quantities. Most implicit methods however have no such restrictions. Hence implicit methods are used in RANS calculations where fine meshes are necessary to capture the boundary layer close to a wall surface. The OverTURNS code uses the implicit Lower Upper Symmetric Gauss Seidel Scheme (LUSGS) [50, 51] along with Newton sub-iterations [52] in order to remove factorization errors and to fully recover time accuracy.

If an index for time step is included in the semi-discrete form of the NS equations (eqn. 2.29), then an implicit scheme can be written as

$$\frac{\partial \hat{Q}^{n+1}}{\partial t} = -\frac{\hat{F}^{n+1}_{j+\frac{1}{2}} - \hat{F}^{n+1}_{j-\frac{1}{2}}}{\Delta \xi} - \frac{\hat{G}^{n+1}_{k+\frac{1}{2}} - \hat{G}^{n+1}_{k-\frac{1}{2}}}{\Delta \eta} - \frac{\hat{H}^{n+1}_{l+\frac{1}{2}} - \hat{H}^{n+1}_{l-\frac{1}{2}}}{\Delta \zeta} + \hat{S}^{n+1}_{j,k,l} \qquad (2.34)$$

In the above equations, the flow quantities and therefore the fluxes and source terms are known at time step (n) are desired at step $(n+1)$. Fluxes at $(n+1)$ time step need to be linearized and expressed in terms of fluxes and conservative variables at

step (n). The nonlinear terms are linearized in time about state $\hat{Q}^n$ by Taylor Series as:

$$\hat{F}^{n+1} = \hat{F}^n + \hat{A}\Delta\hat{Q}^n + O(h^2) \tag{2.35}$$

$$\hat{G}^{n+1} = \hat{G}^n + \hat{B}\Delta\hat{Q}^n + O(h^2) \tag{2.36}$$

$$\hat{H}^{n+1} = \hat{H}^n + \hat{C}\Delta\hat{Q}^n + O(h^2) \tag{2.37}$$

where $\hat{A} = \frac{\partial\hat{F}}{\partial\hat{Q}}$, $\hat{B} = \frac{\partial\hat{G}}{\partial\hat{Q}}$ and $\hat{C} = \frac{\partial\hat{H}}{\partial\hat{Q}}$. The source terms can also be linearized with respect to the conservative variables. Note that the linearizations are second order accurate and so if a second order time scheme is chosen (typically used in OverTURNS), the linearization would not degrade the time accuracy. With the flux linearization and assumed first order Euler implicit time discretization, $(\partial_t\hat{Q}^{n+1} = \frac{\Delta\hat{Q}^n}{\Delta t})$, the equation. 2.34 can be written in 'delta form' as:

$$\left[I + \Delta t(\delta_\xi\hat{A}^n + \delta_\eta\hat{B}^n + \delta_\zeta\hat{C}^n)\right]\Delta\hat{Q}^n = -\Delta t\left[\delta_\xi\hat{F}^n + \delta_\eta\hat{G}^n + \delta_\zeta\hat{H}^n - \hat{S}^n\right] \tag{2.38}$$

which is simplified as

$$\text{LHS } \Delta\hat{Q}^n = -\Delta t \text{ RHS} \tag{2.39}$$

The RHS represents the physics of the problem and the left hand side (LHS) the numerics. Therefore, the LHS determines the rate of convergence of the solution. In an implicit time integration method, the LHS is a large banded system of algebraic equations and is solved using LUSGS. In the LUSGS algorithm, LHS is factored into

35

three matrices, namely, lower (L), upper (U) and diagonal (D) matrices. Using first order split flux Jacobians and neglecting the viscous contribution, these matrices can be represented as:

$$L = \Delta t(-\hat{A}^+_{j-1,k,l} - \hat{B}^+_{j,k-1,l} - \hat{C}^+_{j,k,l-1}) \tag{2.40}$$

$$D = I + \Delta t(\hat{A}^+_{j,k,l} - \hat{A}^-_{j,k,l} + \hat{B}^+_{j,k,l} - \hat{B}^-_{j,k,l} + \hat{C}^+_{j,k,l} - \hat{C}^-_{j,k,l}) \tag{2.41}$$

$$U = \Delta t(\hat{A}^-_{j+1,k,l} + \hat{B}^-_{j,k+1,l} + \hat{C}^-_{j,k,l+1}) \tag{2.42}$$

This can be solved by a forward and a backward sweep using a two-factor scheme that can be written as:

$$[D + L]\Delta\bar{Q} = -\Delta t[RHS]$$

$$[D + U]\Delta\hat{Q} = D\Delta\bar{Q} \tag{2.43}$$

Further simplifications involve approximating the split flux Jacobians, e.g. $\hat{A}^\pm = \frac{1}{2}(\hat{A} \pm \sigma_\xi)$, σ_ξ being the spectral radius. This reduces D to a diagonal matrix and its inversion reduces to just a scalar inversion. The contribution of viscous fluxes can be approximated by adding a scalar term to the spectral radius (e.g. $\sigma_\xi + \sigma_\xi^v$), where

$$\sigma_\xi^v = \frac{2\mu\left(\xi_x^2 + \xi_y^2 + \xi_z^2\right)}{\rho} \tag{2.44}$$

In OverTURNS, the factorization errors due to the approximations on the LHS is removed by using Newton sub-iterations at each physical time step. This

also removes the linearization errors. Furthermore, the 2nd order backward difference in time (BDF2) is implemented by substituting $\partial_t \hat{Q}^{n+1} = \frac{3\hat{Q}^{n+1} - 4\hat{Q}^n + \hat{Q}^{n-1}}{2\Delta t}$

2.3.4   Turbulence Modeling

With the introduction of the **Reynolds stress term** (eqn. 2.28), additional variables are introduced into the RANS equation. Turbulence modeling fixes this problem by finding closure to the RANS equation by approximating the Reynolds stress term. Assuming isotropic eddy viscosity, the stress term can be represented by:

$$\tau_{ij}^R = \mu_t \left[\left(\frac{\partial u_i}{\partial x_j} + \frac{\partial u_j}{\partial x_i} \right) - \frac{2}{3} \frac{\partial u_k}{\partial x_k} \delta_{ij} \right] \tag{2.45}$$

where μ_t is the turbulent viscosity. Various turbulence models have been developed to obtain the turbulent viscosity field. The models range from zero equation algebraic turbulence models (Baldwin-Lomax [53]), four equation turbulence models ($\nu^2 - f$ model [54]) to Reynolds Stress models. The four equation $\nu^2 - f$ model by Durbin, besides incurring increased stiffness to the differential equations, demands extremely high computational time for solving the turbulent viscosity field.

OverTURNS uses the Baldwin-Lomax model, but it is restricted mostly to steady and attached flows ([43]). For more general flows, OverTURNS uses the one equation model of Spalart and Allmaras [56]. The Spalart-Allmaras (SA) model is popular in aerospace flow problems because it was developed with such applications

in mind, and therefore it is used in OverTURNS for all computations in the present work. In the SA model, the Reynolds stresses are related to the mean strain by the isotropic relation, $\overline{u_i' u_j'} = -2\nu_t S_{ij}$, where ν_t is the turbulent eddy viscosity, which is obtained by solving a one equation PDE for a related variable, $\overline{\nu}$ (and $\nu_t = f(\overline{\nu})$).

2.4   Mesh Generation

2.4.1   Blade Mesh

The CFD solution process involves applying the numerical algorithm described in the previous section at discrete "computational grid" points. This requires the generation of appropriate computational meshes or grids for the problem being solved. A well generated mesh with sufficient resolution to capture all the essential flow features such as tip vortices is crucial for a reliable CFD model. To accurately represent blade surfaces body-conforming curvilinear meshes are required. The current study uses a hyperbolic mesh generation technique   [57] is used to generate 2-D C-type meshes around airfoil sections. The C-type meshes are free from the geometric singularity that occurs for O-type meshes at the trailing edge of the airfoil. In addition, grid clustering at the trailing edge allows for efficient capturing of the shed wake. These 2-D sections are then stacked along the span of the rotor blade, as shown in Fig. 2.2(a) and taking into account the variation of geometric properties such as twist, chord (taper) and sweep along the blade span. The C-type spanwise sections are rotated and collapsed near the root and tip of the blade, to give the overall mesh a C-O topology. The details of the collapsing technique are
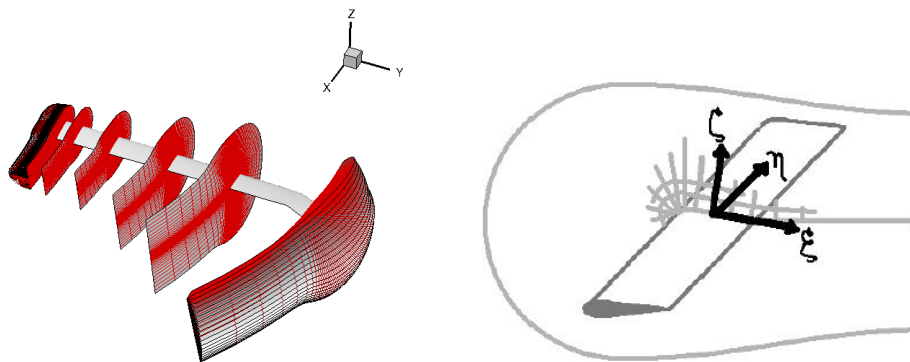
(a) 2-D C-type section stacked along the blade span

(b) Curvilinear coordinate system on blade mesh

Fig. 2.2: C-O mesh on the UH-60 blade

given in [58]. The three curvilinear coordinate directions for the blade mesh are depicted in the schematic shown in Fig. 2.2(b). The ξ direction is the tangential or "'wraparound"' direction, with the η coordinate being in the spanwise direction and the ζ being the local normal direction.

2.4.2 Overset Meshes

A common difficulty in simulating complex geometries is that a single continuous grid is not sufficient to capture all the essential flow features. For hovering rotors, it is very difficult to generate a single structured mesh that can capture the boundary layer near the blade surface as well as adequately resolve the rotor wake, especially the blade tip vortices and their evolution. In such cases the common approach is to use unstructured meshes, multiblock structured meshes or overlapped chimera stuctured (overset) meshes. Unstructured meshes are generally considered

suitable for complex configurations, but unstructured flow solvers come with additional memory requirements and are less efficient compared to structured mesh solvers. Using block structured grids requires a matching of the blocks at the grid interfaces and can make the grid generation process very complex.

One alternative to using multiple structured grids is to use grids that overlap with each other (overset grids). The overset grids or chimera grids as they are sometimes referred to were first introduced by Steger [59] in 1983. The idea here is to use multiple overlapping meshes which span the computational domain. Thus, overset meshes can be viewed as being structured locally but unstructured globally. In the regions where the meshes overlap, the solution is computed on one mesh and interpolated onto the others. There is however an additional computational expense associated with overset grids in that additional work is required to identify the points of overlap between the meshes and to perform the interpolations in these regions. Additionally, there is a possibility of loss of conservation property of the numerical scheme. However, the resulting errors can be minimized if discontinuous flow features such as shocks and shear layers do not cross the overlap region. The present work therefore employs overset meshes for efficient wake capturing. The details of the overset mesh connectivity algorithm are described in sec. 2.5
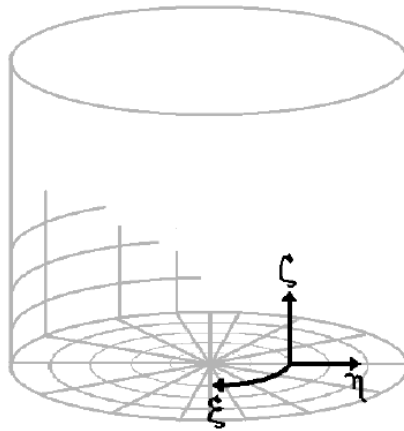
2.4.3   Background Mesh

For rotor problems, the blade mesh itself is overset in one or more background meshes, in order to resolve the rotor wake. In the current work, the background mesh consists of identical planes which are rotated in the azimuthal direction. The background mesh has appropriate refinement in the vicinity of the rotor. A sample background mesh for a 4-bladed rotor is show in Fig. 2.3. Since the flow conditions are assumed to axisymmetric, only one blade is simulated with the appropriate periodic boundary conditions at the end of the background mesh. A schematic showing the curvilinear coordinate system on the background mesh is shown in Fig. 2.3(c) . The structure and placement of the background mesh for the specific cases will be introduced in Chapter 3.

2.5   Overset Mesh Connectivity

The next step after the generation of overlapping meshes is to determine the connectivity information between the various meshes participating in the simulation. The chimera connectivity methodology involves three main steps: i)hole cutting, ii)identification of hole fringe and chimera boundary points, and iii)finding donor cells and interpolation factors. The hole cutting step involves specifying *hole* regions which define the blade surface geometries and identifying points which lie inside such regions. These points are "blanked out" and do not participate in the solution process. After obtaining the list of hole points, the list of hole fringe points, which require solution information from other grids to serve as boundary conditions, is
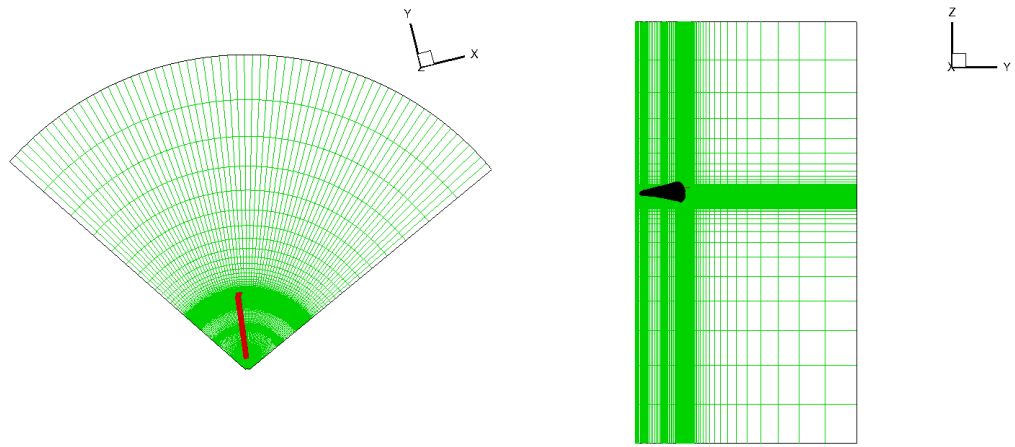
(a) Top View of the Background Mesh   (b) Side View of the Background Mesh

(c) Curvilinear coordinate system on the

background mesh

Fig. 2.3: Background mesh used in the rotor simulations

extracted. As a next step, the list of chimera boundary points, which are the points

on the boundary of one mesh, requiring solution information from another mesh,

is specified by the user. The size of the fringe and chimera boundary layers is a

function of the stencil used by the spatial scheme in the simulation. Finally, the

donor cells from the other grids and the interpolation factors are found for each type

of boundary point. The donor cell search uses the so-called "stencil walk" procedure [60].

The present work uses the Implicit Hole Cutting methodology developed by Lee and Baeder [61] and extended by Lakshminarayanan [44]. In this technique the connectivity is established without explicitly knowing, cutting and expanding the hole. The basic idea behind the IHC approach is that the solution in any region with overlapping meshes should be computed on the mesh that contains the cell with the smallest cell volume in that region. The method parses through every point in each grid to chooses the best cell in multiple overlapped regions, leaving the rest as receiver points. Hole cutting is a byproduct of this process of cell selection. A more detailed description of the workings of the IHC algorithm can be found in [44, 62]. Figure 2.4 shows a typical overset background mesh (green) with a hole. The blade mesh (red) can be seen as well.
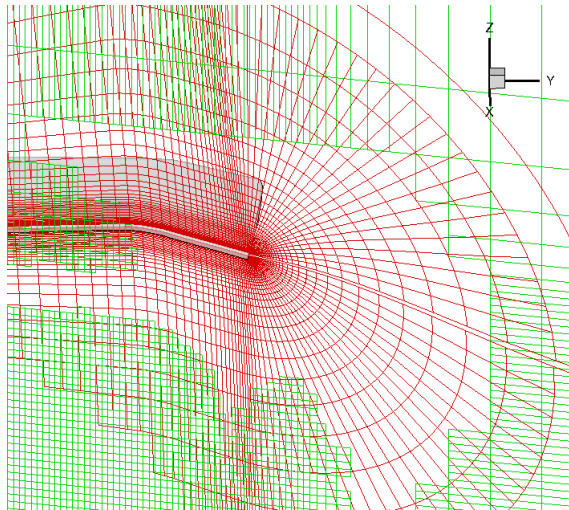
Fig. 2.4: Overset mesh connectivity

43

2.6 Blade Deformation
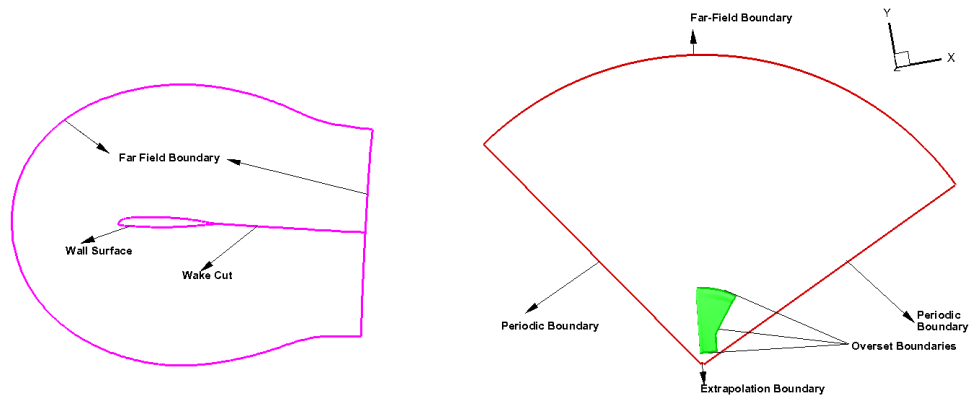
2.7 Boundary Conditions

There are several types of boundary conditions commonly encountered in the solution of the Navier-Stokes equations. Physical boundary conditions arising during the solution procedure were described in section 2.2. In addition, there are additional numerical boundary conditions that present themselves due to the grid topology. This section describes the treatment of both sets of boundary conditions. Typical boundary conditions found in the solution of the Navier-Stokes equations are shown on a 2-D schematic of a C-type mesh, Fig. 2.5(a). Additionally, one encounters the periodic boundary condition in hovering rotor simulation, as can be seen from Figures 2.5(b) and (c), which show the boundary conditions on the cylindrical background mesh. All of these boundary conditions, along with the special hover BC are discussed briefly.

Wall Boundary Condition

All solid walls in this work are treated as viscous walls. The no-slip boundary condition is therefore applied, which requires the fluid velocity at the wall to be equal to the wall surface velocity. All the solid wall, the density ρ is extrapolated (zeroth order) from the interior of the domain and the pressure p is then obtained by solving the normal momentum equation.
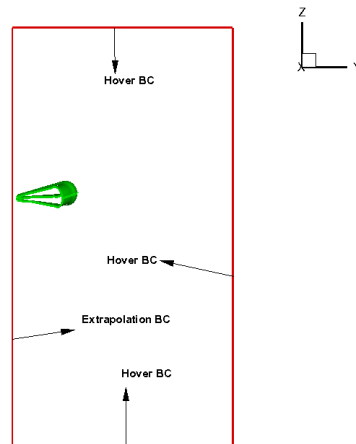
Farfield Boundary Condition

The outer boundaries at which the farfield boundary condition is applied should ideally be placed far enough (typically 20-30 chords) from body surfaces such that the prevailing conditions are close to freestream, so that no spurious wave reflections would occur at the boundary. To determine the boundary conditions, characteristic-based Riemann invariants [63] are used. In this approach, based on

(a) C Mesh Topology

(b) Top View of the Background Mesh

(c) Side View of the Background Mesh

Fig. 2.5: Boundary conditions on the overset background mesh

45

the direction of the velocity vector and the sonic velocity, the corresponding Riemann invariants are extrapolated either from the interior or the freestream.

Hover Boundary Condition

For a hovering rotor, the vortices in the rotor wake stay under the blade at all times and the resulting induced velocities can be expected to be significant at distances of a few rotor radii. For computational efficiency, the farfield boundaries are held to less than five rotor radii away from the blade surface. In this case, the linearized characteristic free-stream boundary condition cannot be used since the flow velocities are large. In this work, the point-sink boundary condition approach of Srinivasan et. al. [43] is used. A schematic of this approach is shown in Fig. 2.6. It is well known from momentum theory [4] that the asymptotic contraction of the rotor wake is approximately $\frac{R}{\sqrt{2}}$, and the non-dimensional inflow velocity resulting from the entrainment of fluid into the rotor disk at such a downstream location is $\sqrt{\frac{C_T}{2}}$, where C_T is the rotor thrust coefficient. As shown in the schematic, this velocity is used in the region marked "Outflow".

In order to satisfy global mass conservation, the rest of the farfield boundary is then assumed to be an inflow, the velocities of which are assumed to be induced by a point sink placed on the rotor hub. The magnitude of this spherically symmetric induced velocity is given by:

$$\frac{V_{induced}}{\Omega R} = \frac{1}{4}\sqrt{\frac{C_T}{2}}\left(\frac{R^2}{x^2 + y^2 + z^2}\right) \qquad (2.46)$$
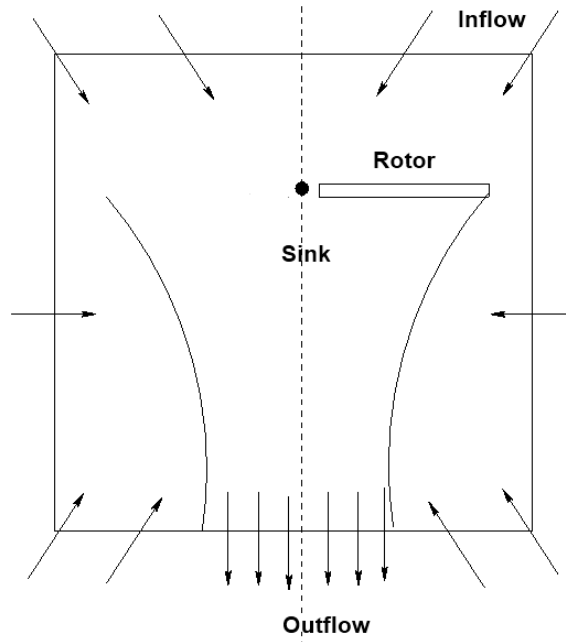
Fig. 2.6: Schematic of Point-Sink boundary condition

where x, y, z is the position vector relative to the placement of the sink. Linearized Riemann invariants are then used to determine the conserved variables at the boundary.

Wake Cut Boundary Condition

At the wake cut region, grid planes collapse on to each other. Along these planes, an explicit simple average of the solution from either side is used. Similar boundaries are present at the root and tip of a C-O grid and are treated in the same manner.

Periodic Boundary Condition

The hovering rotor calculation can be simplified by assuming periodicity, thereby performing the entire calculation by simulating just one blade. The interaction with the remaining blades is enforced via rotational periodic boundary conditions. The periodic boundary condition is implemented by creating dummy cells at the boundary, where the vector quantities are prescribed using coordinate rotation and the scalar quantities are set identical.

Interface Boundary Condition for Parallel Runs

In addition to the boundary condition arising due to the mesh topology, the actual implementation of the code can also give rise to an additional set of boundary conditions. One such instance is of the internal interface BC which is a result of the coarse grain parallelization of the solver. The need to accurately resolve the rotor wake can result in fairly large mesh sizes, which pose a severe constraint to the available memory on a single processor system. Even if reasonable meshes are generated, conforming to the memory limitations, the available processing speed also becomes a limiting factor. Thus, the OverTURNS code is parallelized to a certain extent. The parallelization is achieved by dividing the computational domain into smaller sub-domains and collaboratively solving on each sub-domain. This is called as the "domain decomposition" method. Each sub-domain is solved on a separate processor and communication between processors is implemented using the Message Passing Interface (MPI) library. The partitioning of the domain is achieved by

splitting each grid into an equal number of sub-grids in a single direction. For the blade mesh, the splitting direction is the spanwise direction and for the background mesh, the vertical direction is used. Sufficient overlap is ensured between the split meshes to maintain the spatial accuracy. An artificial internal boundary condition is created in the overlap regions, where the solution from one region is copied into the other.

2.8 Summary

In this chapter, the major steps which make up the CFD methodology have been discussed in detail. These steps are enumerated and summarized below:

- The problem is domain is first discretized by generating a computational mesh that resolves the geometry and provides sufficient resolution to capture all the essential flow features. For the rotor blades, a C-O type mesh was generated using a hyperbolic grid generator. This blade mesh was then overset within a cylindrical background mesh.

- The use of overset or chimera grids comes with the additional cost of determining connectivity information between the meshes participating in the solution process. At the overset boundary "donor" and "receiver" cells within each mesh must be identified. This is in addition to any "hole" points in the simulation. The Implicit Hole Cutting (IHC) method is used in this work to determine overset connectivity information.

- The flow solver uses the compressible Reynolds Averaged Navier Stokes (RANS)

equations, to solve for the flowfield. The one equation Spalart-Allmaras (SA) turbulence model is used for RANS closure. The equations are solved in the curvilinear coordinate system. The equations are formulated in the rotating reference frame with source terms to account for the Coriolis acceleration.

- Appropriate boundary conditions are prescribed during the solution process. Wall boundaries, farfield boundaries, wake cuts, periodic and extrapolation boundary conditions are some of the ones encountered in this work. In addition, the point-sink boundary condition is used in hover to setup the rotor inflow and to limit the size of the domain boundaries to a reasonable value.

Utilizing the steps listed above, a high-fidelity solution for the flow-field around a hovering rotor can be obtained. However, before using the code to compute the complex flow around a hovering a rotor, it should be validated against existing results. The next chapters described the validation of the flow solver and then compare the predictions for a slatted UH-60A rotor against the baseline values.

Chapter 3

CFD Validation

3.1 Overview

The objective of the current work is to use a high-fidelity CFD methodology
to analyze Multi-Element Airfoil (MEA) rotors in hover. Before the CFD solver
is applied to analyze the new rotor configuration, it needs to be validated against
available experimental data, for the purpose of establishing confidence in the results.
As stated earlier, there exists no quantitative data in open literature for MEA rotors
in hover. However, there is data from 2-D wind tunnel testing of slatted airfoil and
experimental results for a model scale UH-60A rotor in hover. The validation,
therefore, will be performed in two stages:

1. Validation of the CFD solver against available 2-D wind tunnel experiments
   of slatted airfoils.

2. Validation of the 3-D CFD solver against model scale experiments of a UH-60A
   rotor in hover.

The wind tunnel experiment for the 2-D validation study is a compressible high
Reynolds Number flow on a SC2110 airfoil. Lorber et al. [25] conducted extensive
wind tunnel studies on a SC2110 airfoil with a leading edge slat, under steady and
unsteady conditions. The tests were conducted in the UTRC Main Wind Tunnel,

using the 33in wide by 8ft high Two Dimensional Channel (TDC). The model chord was 24in. The test Mach number range was 0.2 to 0.75, but for the present work, the test data for only the Mach number of 0.3 is considered.

3.2   Steady Slatted Airfoil Validation

This section compares the CFD predictions against experimental results for 2-D slatted airfoils. Investigation of the flow physics provides an insight into the working of LE slats in extending the static stall limit compared to single element airfoils. Also, since the primary objective of this work is to analyze slatted rotors in hover, where the airfoil sections operate well below their static stall limit, special attention is paid to the slatted airfoil characteristic at low angles of attack.

The steady state computations were performed on the SC2110 baseline airfoil, with two different slat configurations, the so called S-1 and S-6. The S-6 is a high-lift configuration but incurs a large drag penalty at low angles of attack. The S-1 is a compromise between the various high-lift and minimum drag configurations developed by Lorber et al. [25]. The SC2110 airfoil is a modified version of the SC1094R8 airfoil, which is the airfoil section in the midspan region of the UH-60A rotor. The modifications were made in the leading edge region of the main airfoil element to promote better tailoring of the flow when the slat is present. Both the airfoil sections along with the two slat configurations are shown in Fig. 3.1.

Steady lift, drag and pitching moment coefficients are computed for angles of attack over the range $\alpha = [0°, 24°]$ at $Re = 4.14 \times 10^6$ and $M_\infty = 0.3$. The
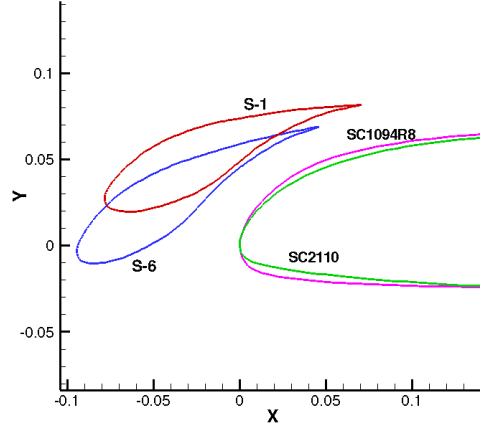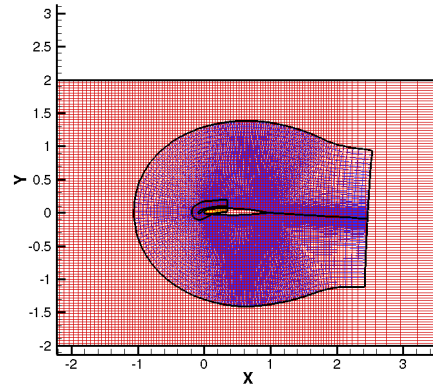
Fig. 3.1: Airfoil and Slat Configurations

computational meshes used in the simulations are shown in Figures 3.2 (a) and
(b). The C type airfoil and slat meshes are completely embedded inside a Cartesian
background wind tunnel mesh. The height of the wind tunnel wall was 4 chord
lengths. The slat mesh had 317×97 points in the wraparound (chordwise) and
normal directions respectively. The airfoil mesh had 365×138 points while the
background mesh had 151×101 points in the streamwise and normal directions
respectively. The Implicit Hole Cutting (IHC) method described in Chapter 2 is
used to determine the connectivity between the various meshes. The output mesh
system after the IHC process is shown in Figures 3.2(c) and (d).

Fig. 3.3 compares the computational predictions of lift, drag and pitching
moment for the SC2110 airfoil with and without the slats against the available
experimental data over the angle of attack range. In the figures the non-dimensional
values of C_l, C_d and C_m are obtained by normalizing the forces using the effective

53
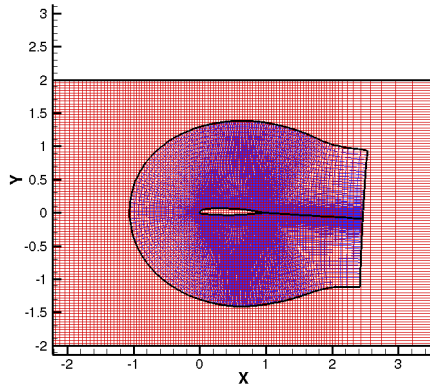
(a) Airfoil in a Wind Tunnel   (b) Airfoil and Slat in a Wind Tunnel
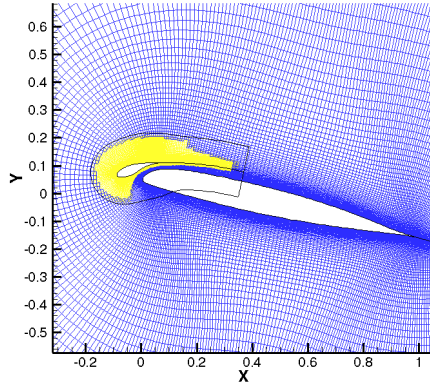
(c) Hole Cut near the Airfoil Slat Boundary (d) Hole Cut near Airfoil Wind Tunnel
Boundary
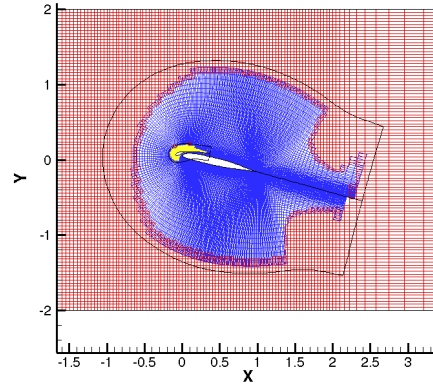
Fig. 3.2: Computational Meshes used for 2-D Validation Studies

chord for the slatted airfoil. The effective chord, as described in [25] is obtained by
joining the LE of the slat to the TE of the main element and projecting onto the
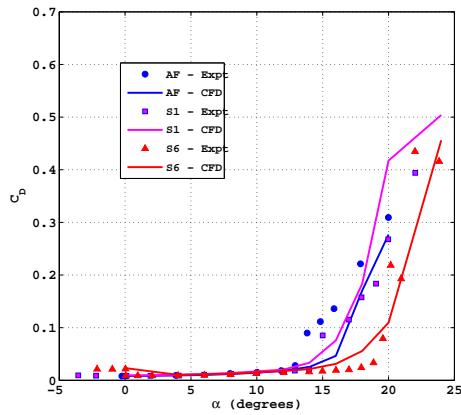chord of the main element.

The benefits of the LE slat as a high-lift device are evident from Fig. 3.3(a),
which shows the lift coefficients for the three configurations. It can be seen that the
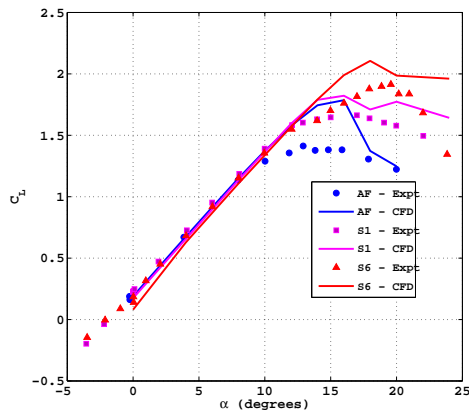
(a) Lift Coefficient
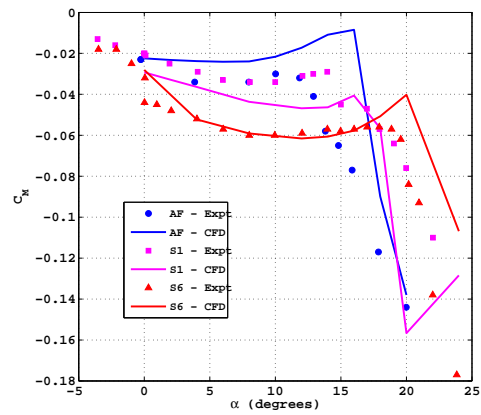
(b) Moment Coefficient

(c) Drag Coefficient
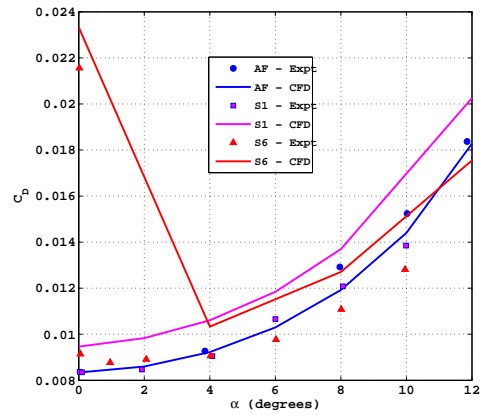
(d) Drag Coefficient at lower angles

Fig. 3.3: 2-D Steady Valdiation for SC2110 airfoil with S-1 and S-6 slats at $Re = 4.14 \times 10^6$ and $M_\infty = 0.3$

S-6 slat has the highest $C_{L_{max}}$. It is also seen that the predictions from OverTURNS agree well with the experimental values in the regions where the lift curve slope is linear. These ranges of angles of attack represent fully attached flow over the airfoil sections. OverTURNS however consistently over predicts the $C_{L_{max}}$ compared to the experiments. This is due to the inability of the code to accurately predict the

stall angle and the discrepancy is somewhat lessened for the slatted sections, where stall occurs at a higher angle compared to the single airfoil.

The high lift benefit from the S-6 slat comes at price of a large pitching moment penalty. The S-6 configuration generates about 33% more nose down pitching moment compared to the single airfoil (Fig. 3.3(b)). The delay in the computational prediction of stall is also evident from the figure with the drop in pitching moment occuring at a higher angle of attack compared to the experiments. Figures 3.3(c) and (d) show the predictions of the drag coefficient. It can be seen that the delay in stall prediction results leads to the computational values of drag being much smaller for the single airfoil compared to the experimental values, at the higher angles of attack. This also means that the computational values of drag for S-6 are larger compared to the experimental values at these same angles of attack. The flow over the slatted airfoil remains attached to a higher angle of attack compared to the single airfoil. The assumption of fully turbulent flow leads to larger values of skin friction drag in case of attached flow compared to the experiments where it is possible that there are regions of laminar flow, especially over the slat.

3.2.1   Flow Physics

To further investigate the flow over the slatted airfoils sections, it is instructive to look at pressure coefficients, streamline flow patterns and boundary layer profiles. Figures 3.4(a) and (b) shows the surface pressure coefficient on the main element and the slat respectively, at the very low angle of attack of 0°. As explained in

sec. 1.1.1, the "slat effect" is to reduce the negative pressure peak over the main airfoil element and thereby delay the onset of boundary layer separation. It is clearly seen from the figures that at this low angle of attack, the slat does not have much effect over the flow over the main element. The S-6 slat has an adverse effect on the main element pressure distribution with a larger negative pressure peak compared to the S-1 and the baseline airfoils. In addition, the slat pressure distributions suggest an almost zero contribution to lift from the S-1 slat and a negative contribution from the S-6 slat. It should also be noted that for comparison purposes the leading edges of both slats are rigidly translated to the origin, while plotting the pressure coefficient $(X' = X - X_{LE})$.
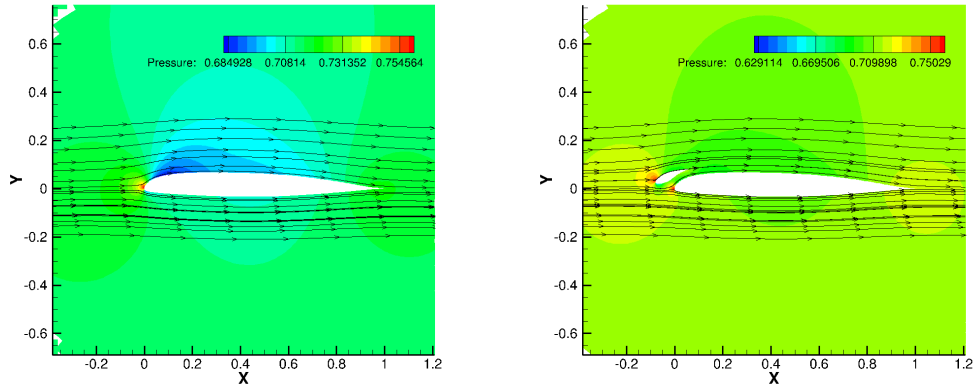

(a) Main Element Surface C_P (b) Slat Surface C_P
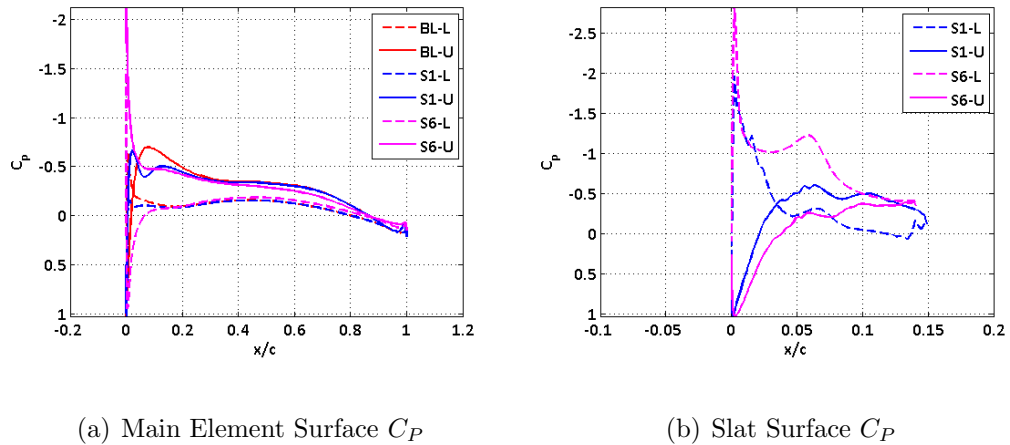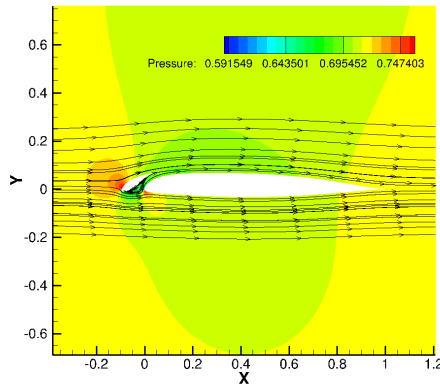
Fig. 3.4: Pressure Coefficient at $\alpha = 0°$

Figures 3.5(a), (b) and (c) show the pressure contours along with the streamline patterns on the Airfoil, S-1 and S-6 configurations respectively. As can be seen from the figures, the more nose down S-6 configuration has the stagnation point on the upper surface and separated flow on the lower surface. The separated region

on the lower surface is very close to the leading edge of the main element and is a
possible cause for the large localized negative pressure coefficient see in Fig. 3.4(a).
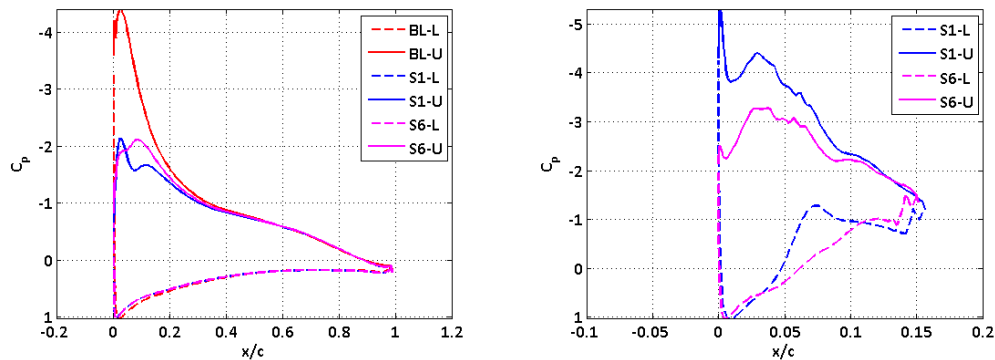

(a) BL

(b) S-1

(c) S-6

Fig. 3.5: Pressure Contours and Streamlines at $\alpha = 0°$

Figures 3.6(a)-(b) and 3.7(a)-(c), show the pressure coefficient, pressure con-
tour and streamline patterns at a 10° angle of attack.

The effect of the slat is fairly obvious from the pressure coefficient plot, with
a large drop in the negative pressure peak on the main element, for the slatted

(a) Main Element Surface C_P (b) Slat Surface C_P

Fig. 3.6: Pressure Coefficient at $\alpha = 10°$

configurations. The offset in the lift from the main element is compensated by the lift from the slats, with the S-1 slat having a large negative pressure peak by virtue of being in a more nose-up position, hence a higher effective angle of attack, compared to the S-6 slat.

Figures 3.9(a)-(b) and 3.8(a)-(c) show the pressure coefficient and pressure contours with streamlines at a 16° angle of attack. Once again, the "slat effect" is evident through the pressure coefficient plots. In addition, one can also see the onset of trailing edge separation on the baseline airfoil whereas the flow on the slatted main airfoil section stays attached.

A close up of the flow near the trailing edge of the slat 3.10 shows that the S-1 slat is starting to experience separation at the trailing edge whereas the flow over the S-6 slat is fully attached. The presence of a shock on the upper surface of the slats, as seen from the pressure contours and its interaction with the boundary layer can be a possible cause of separation.
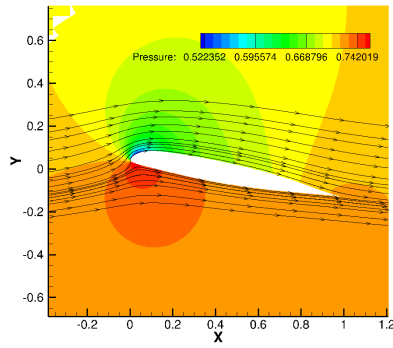
(a) BL
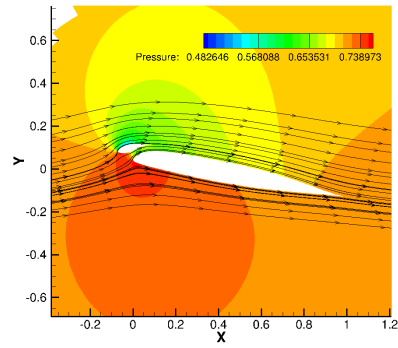
(b) S-1
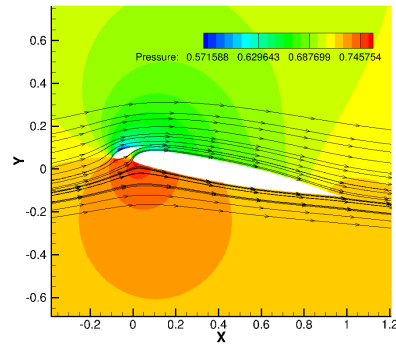
(c) S-6

Fig. 3.7: Pressure Contours and Streamlines at $\alpha = 10°$

Figure 3.11 shows the element wise contributions to the lift. It can be seen from the figure that at the lower angles of attack the S-6 slat has a negative contribution to lift whereas the S-1 slat has an almost zero contribution to the lift. The lower lift coefficient combined with the higher values of drag coefficient results in the slatted section incuring a performance penalty compared to the baseline airfoil at low angles of attack.
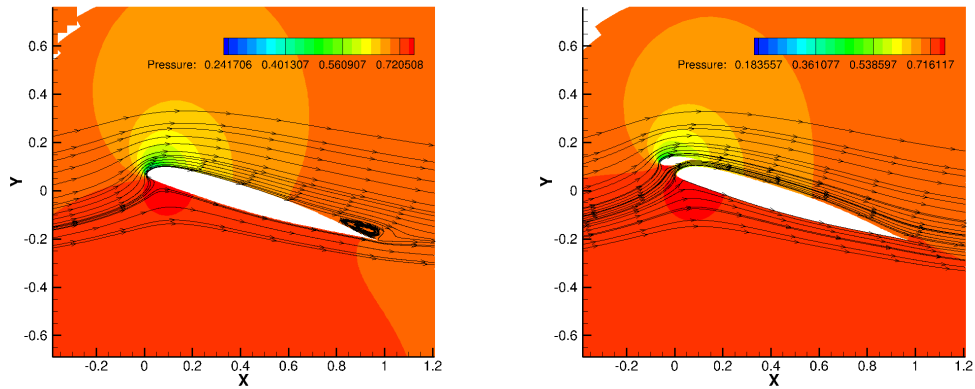
(a) BL

(b) S-1
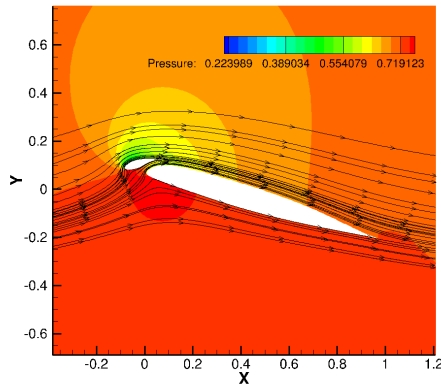
(c) S-6

Fig. 3.8: Pressure Contours and Streamlines at $\alpha = 16°$

### 3.2.2 Limitations of CFD Predictions : Transition Modeling

All the computations performed in this work are with the assumption of fully turbulent flow. This might result in incorrect physical modeling in regions of laminar flow. The slat element, with its low local Reynolds numbers is expected to have a significant region of laminar flow. One obvious consequence of this assumption is the over prediction of drag coefficients for the slatted airfoils(Fig. 3.3(d)) at low
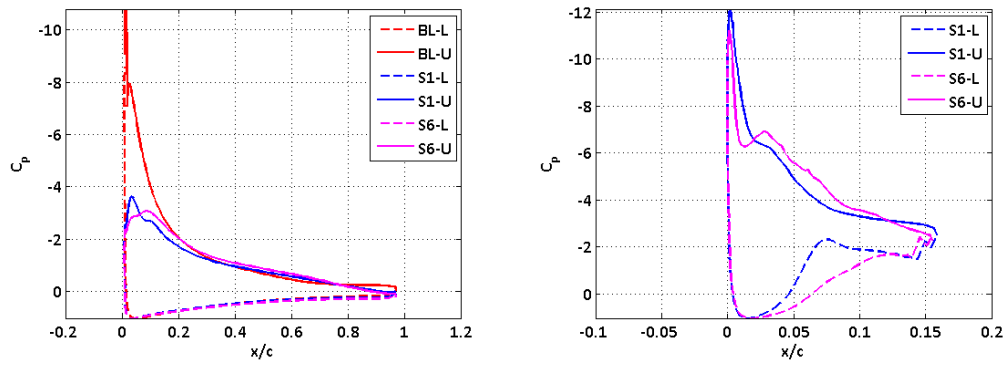
(a) Main Element Surface C_P (b) Slat Surface C_P

Fig. 3.9: Pressure Coefficient at $\alpha = 16\circ$
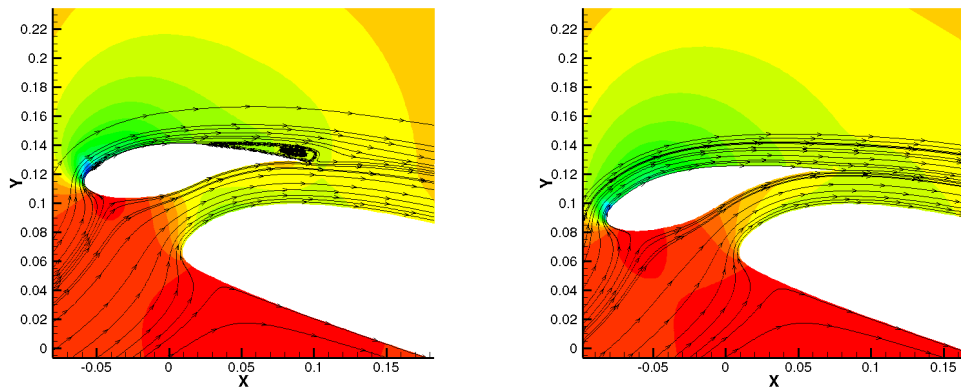
(a) S-1   (b) S-6

Fig. 3.10: Pressure Contours and Streamlines near the Slat at $\alpha = 16\circ$

angles of attack. At low angles, when the flow is fully attached, the drag is domi-
nated by the skin friction (viscous) component, which in-turn is strongly dependent
on the boundary layer profile. The lift force on the other hand is a strong func-
tion of the pressure distribution, which is essentially an inviscid effect. Hence the
predictions of lift coefficients(Fig. 3.3(a))compare reasonably well with experiments.
One additional consequence of the assumption of fully turbulent flow is the inability
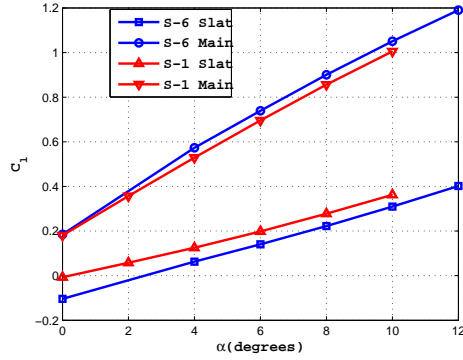
Fig. 3.11: Element wise contributions to lift

to accurately capture any laminar separation bubble that might exist, especially at higher angles of attack. The prediction of the laminar separation bubble is crucial to the accurate prediction of stall and might be one of the reasons for the delay in the CFD predictions of stall. Attempts have been made to model the laminar turbulent transition using a fixed transition point [27]. There are also ongoing attempts to develop a modification to the S-A turbulence model to account for transition [64]. Transition modeling however is beyond the scope of this present work and all the results shown are with the assumption of fully turbulent flow.

3.3   Validation of Baseline UH-60A Rotor in Hover

The ultimate objective of this work is to analyze the hover performance of slatted rotors. Before extending and using the existing CFD framework to analyze slatted rotors, predictive confidence is established by validating the 3-D CFD solver against available data. The model scale UH-60 experiments of Lorber et al. [30] are used in the present study. The data was acquired for a $9.4ft$ diameter$(1:5.73)$scale,

four-bladed model of a UH-60A rotor, which is described in the following section. The UH-60A rotor has two airfoil sections, the SC1095 in the root and tip regions and the SC1094R8 in the mid-span region. The blade has a unique twist distribution as shown in Fig. 3.12(a), varying non-linearly near the tip with a maximum twist angle of $-13.3°$(with respect to the blade root). In addition, there is also a $20°$ of rearward sweep beginning at $r/R = 0.93$ and a lack of taper. The blade planform is shown in Fig. 3.12(b).
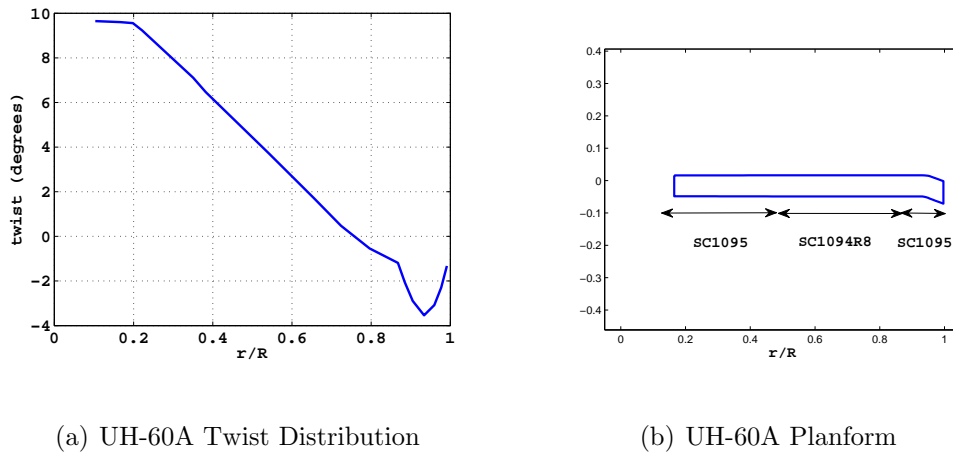

(a) UH-60A Twist Distribution   (b) UH-60A Planform

Fig. 3.12: UH-60A Rotor Geometry

3.3.1 Baseline Rotor Mesh System

The general mesh system used for rotor CFD calculations has been described in sec. 2.4.1. The mesh system used for performance comparisons consisted of a $133 \times 130 \times 61$ blade mesh (wraparound, spanwise and normal directions) C-O type mesh embedded in a $67 \times 174 \times 112$ cylindrical background mesh (azimuthal, radial and normal directions), for efficient wake capturing (Fig. 3.13). The background

mesh was clustered appropriately in regions of high gradients (near the blade), where the grid spacing spacing was $0.1c$.
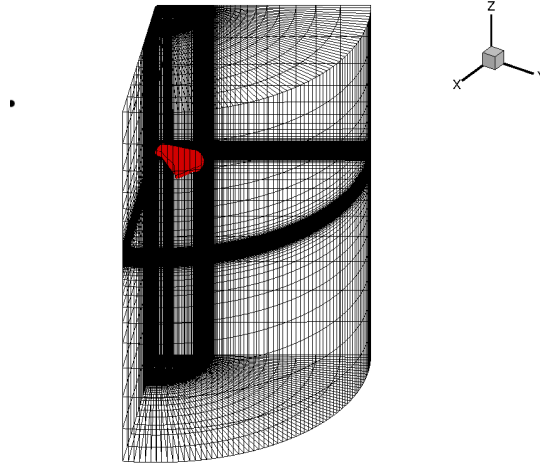

Fig. 3.13: Blade and Background Meshes used for Baseline Rotor Validation

In order to compare against the experimental results, a collective angle sweep was carried out. The exact blade structural deformations obtained in the experiments are subject to U.S Army regulations and are not available in open literature. To account for the blade deformations, the comprehensive analysis code, UMARC [65] was used. The deflections were obtained by trimming the rotor to a thrust value corresponding to $C_T/\sigma = 0.084$, which corresponds to the highest figure of merit obtained in the experiments. The blade elastic deformations obtained were then assumed to be constant across the range of collective angles for which the sweep was carried out. The elastic twist distribution is shown in Fig. 3.14(a). For each collective angle, it was observed that the simulation took about 12-14 rotor revolutions to convergence. The simulations were run in a time-accurate manner with a time step corresponding to an azimuthal discretization of $d\psi = 0.25°$, which

results in 1440 time steps per rotor revolution. Five Newton sub-iterations were run at every time step to reduce factorization errors. The thrust convergence history is shown in Fig. 3.14(b).

The slow convergence of the computations can be attributed to the close proximity of the rotor wake system to the rotor blades. It was observed during the simulations that the root vortex played an important role in the solution convergence. The root of the blade is modeled in the same manner as the blade tip and therefore the root vortex is free to convect based on the existing inflow distribution. It was observed that the root vortex was initially convected above the blade and then as the solution progressed in time and a reasonable inflow was established over the rotor disk, the root vortex was convected downwards. In practice, the root of the blade is in close proximity to the rotor hub and its associated mechanisms, which might prevent the formation or upward convection of the root vortex. Strawn and Djomehri [41] modeled the hub as a body of revolution. Aside from affecting the solution convergence rate, the root vortex does not have a noticeable impact on the rotor performance predictions.

Performance Comparison

The performance predictions obtained using the CFD solver are compared against available data for a model scale UH-60 rotor, obtained from the experiments of Lorber et al. [30]. As described in Chapter 1, there is a considerable amount of scatter in the available data for a UH-60A rotor. Fig. 3.15 shows the differences in
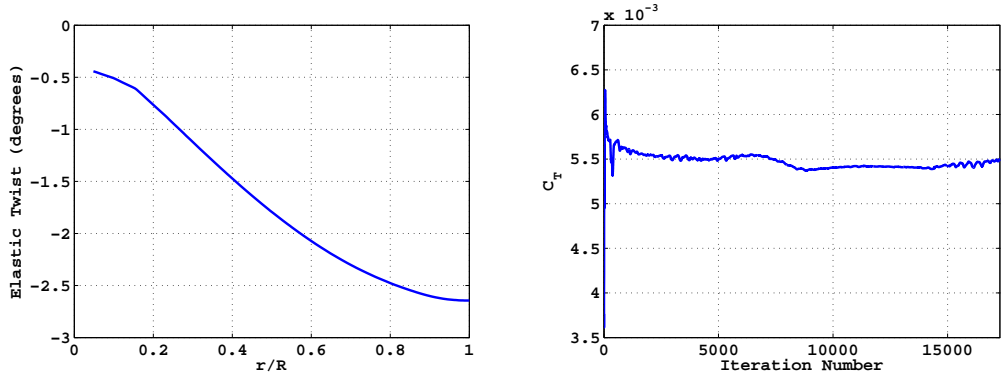
(a) Elastic Twist used in simulations

(b) Thrust Convergence History for 10° collective

Fig. 3.14: Baseline Rotor Simulations

the Figure of Merit for the UH-60 rotor obtained using different experiments and flight tests. It can be seen that there are considerable differences even among the two successive model scale experiments, which were conducted on identical rotors, but in different wind tunnels. For this reason, while plotting the CFD predictions, both sets of model scale experimental results are shown and unless stated, the default experimental values refer to those obtained from the first set of experiments [30]

Figure 3.16 compares the predictions of thrust coefficient vs power coefficient obtained using CFD against the experimental values. In general, there is good agreement between CFD and experiment, especially at the low to moderate thrust conditions. Figure 3.17 compares the predictions of the rotor figure of merit vs thrust coefficient from CFD and experiment. Once again, CFD predictions compare well with experiments at the low and moderate thrust conditions. The maximum figure of merit obtained from the simulations is about 4% higher than experiments, mainly due to the under prediction of power from CFD runs. It should be noted
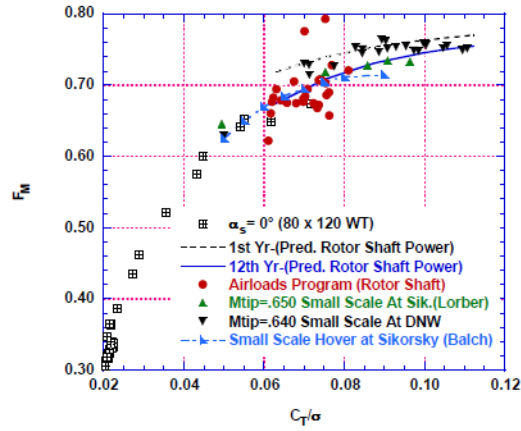
Fig. 3.15: UH-60A rotor hover FM from three full-scale helicopter tests and three model-scale rotor experiments [32]

that the figure of merit is a function of both the rotor thrust and power and any differences in the thrust and power predictions are compounded while comparing the figure of merit.
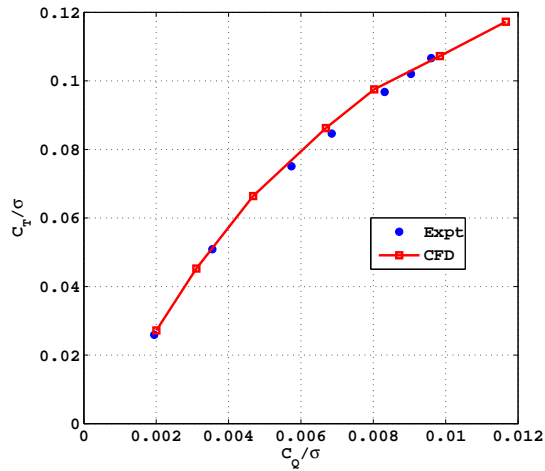

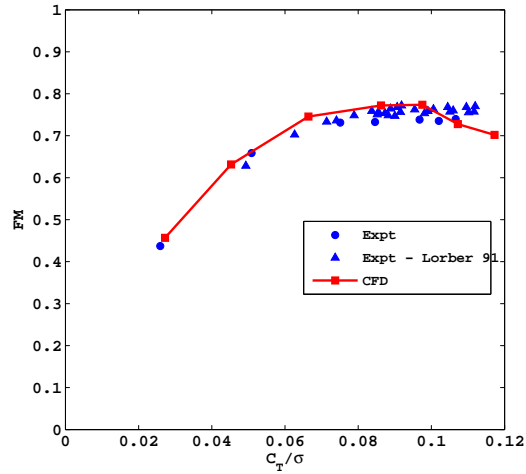Fig. 3.16: Thrust vs Power for the Baseline UH-60A Rotor

Fig. 3.17: FM vs Thrust for the Baseline UH-60A Rotor

Wake Structure and Airloads

The wake structure can have a significant effect on the rotor airloads and therefore the rotor performance. The primary effect of the rotor wake directly affects the induced inflow distribution over the rotor blade. The most important component of the rotor wake in hover is the rotor tip vortex and interaction of the tip vortex from one blade with the other blades and the free shear layer behind these blades can have significant effect on performance predictions.

Figure 3.18 shows the computed radial tip vortex trajectory, compared against experiments around the same thrust level of $C_T/\sigma = 0.085$. It should be noted that in the CFD runs, a collective sweep was carried out, therefore the CFD results have been plotted for the collective setting which results in a thrust level closest to the experiment. This corresponds to a collective angle of $12°$, which results in a C_T/σ of 0.087. To determine the effect of background mesh resolution on the solution,

the simulation was run with a fine background mesh, which had half the spacing $(0.05c)$, near the blade compared to the coarse background mesh. The dimensions of the new background mesh were $67 \times 347 \times 223$ for a total of about 5 million points. It is observed that the CFD predictions compare reasonably well with experiment up to $90°$ wake age.
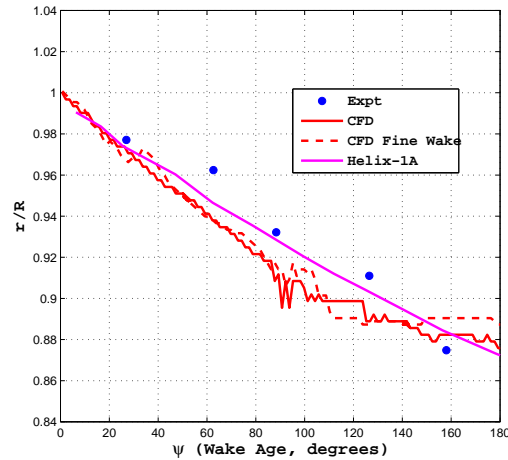

Fig. 3.18: Wake contraction for the baseline rotor at $C_T/\sigma = 0.085$

Figure 3.19 shows the computed wake trajectory (both radial contraction and vertical descent) for the baseline rotor at the collective angle of $12°$, including the experimental values. The blade leading edge is also shown for visualization purposes.

There is a considerable amount of uncertainty in the method used to determine vortex trajectories, both in the experiment and from computations. The algorithm used to compute the vortex trajectory from the computed CFD solution essentially looks for a local maximum in vorticity magnitude on the cylindrical background mesh from a given starting location. The starting point is the blade tip, where
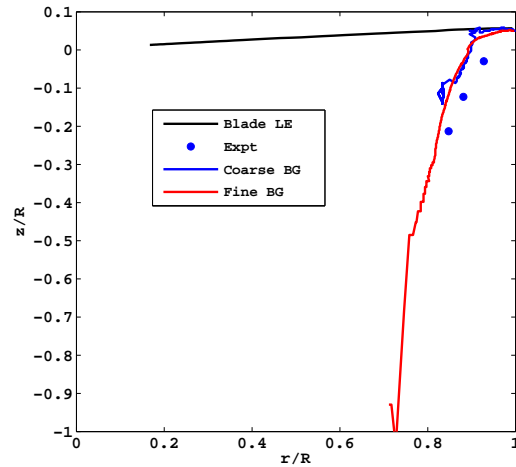
Fig. 3.19: Computed wake trajectory for the baseline UH-60 rotor at $C_T/\sigma = 0.085$

the tip vortex is generated and the algorithm proceeds by searching a finite box in the azimuthal, radial and vertical directions. The results are therefore dependent on the background mesh spacing, partly because the vorticity gets smeared on the background mesh and also because the location is only accurate to the extent of the background mesh spacing. As can be seen from the figures, there is little difference between the coarse and fine mesh results for the first 90° of the wake age, indicating that the spacing of $0.1c$ on the coarse background mesh is adequate to capture the effects of the first returning vortex. Because of periodicity in the simulation and the use of only a 90° background mesh, tracking the tip vortex at later wake ages would require searching in regions further below the blade, where the background mesh starts to stretch (to keep the total number of points at a reasonable value). It is here that one starts to notice difference between the coarse and the fine meshes.

Also shown in Fig. 3.18 are predictions of the wake contraction from a hybrid CFD solver called Helix-1A [66], which uses a near body RANS solver coupled with a vorticity embedding potential flow solver for the wake flow field. The results are interesting because all computations were performed without any elastic deformations and yet they seem to be in better agreement with experiments compared to the present full RANS CFD methodology. The fact that grid refinement did not make a significant effect on the results suggests the use of approximate elastic twist from the comprehensive code is one of the major reasons for the differences between the experimental and computed wake trajectories.

Figure 3.20 shows the vorticity in the wake close to the blade. Since the region of interest is close to the blade, the vorticity is computed using only the solution on the blade mesh. It can be seen that for the case with the coarse background mesh, the first returning vortex cuts through the blade whereas for the fine background mesh, the first returning vortex passes further underneath the blade. It is known from experiments that the first returning vortex passes $0.4c$ below the blade. Also noticeable is the effect of the interaction of the returning vortex with the blade shear layer, which leads to the formation of vorticity which is opposite in sense to the returning vortex.

Figure 3.21 shows the spanwise distribution of the airloads obtained using both the coarse and fine background meshes. It is known from previous computational results [41, 38] that Navier-Stokes simulations tend to over predict the thrust loading near the tip of the UH-60A rotor. From the figure, it is clear that using the fine background mesh has an effect on the blade loading distribution, with slightly lower
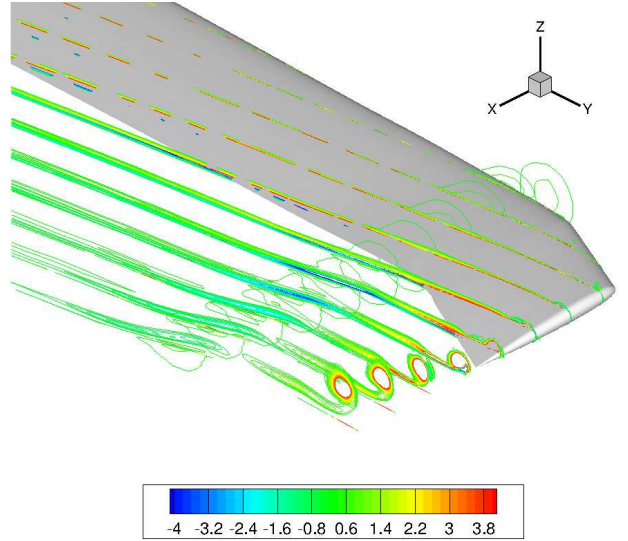
(a) Coarse Wake Mesh
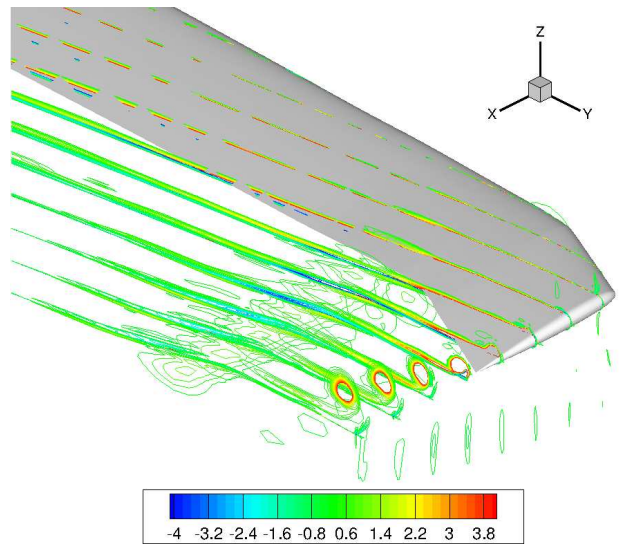
(b) Fine Wake Mesh

Fig. 3.20: Surface vorticity near the blade for two different mesh resolutions

values being predicted outboard and slightly higher values inboard. This is most probably due to differences in strength and trajectory of the first returning vortex on the fine mesh compared to the coarse mesh. The spanwise distribution of the chord force also demonstrates a similar trend. Although the changes in grid density

73

affect the blade-tip loading, these tip-loading changes do not substantially change the overall blade performance, as evidenced in Table. 3.1
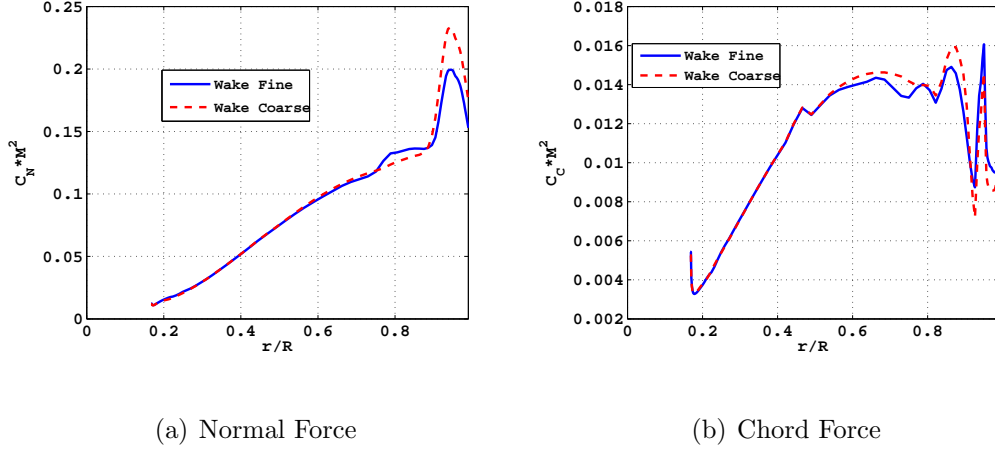

(a) Normal Force

(b) Chord Force

Fig. 3.21: Baseline airloads comparison using Coarse and Fine Background meshes

Mesh	C_T/σ	C_Q/σ	FM
Fine	0.086	0.0067	0.746
Coarse	0.087	0.0069	0.761

Table 3.1: Computed Performance Coefficients using Coarse and Fine Background Meshes

3.4 Summary

This chapter provided a detailed validation of the CFD methodology. The CFD solver was validated for 2-D slatted configurations against available wind tunnel data. It was observed that CFD predictions of lift, drag and pitching moment coefficients showed good agreement with experimental values at low angles of attack.

There is a delay in the CFD prediction of stall resulting in higher maximum lift co-efficients compared to experiments, however the essential trends are captured well in CFD, with the slatted airfoils stalling later compared to the baseline airfoil and thereby achieving higher values of $C_{L_{max}}$. The 3-D CFD solver was then validated against available model experimental data for a hovering UH-60A rotor. Predicted values of performance quantities agreed well with experimental measurements at low and moderate thrust conditions. Predicted values for the tip vortex trajectory also showed good agreement with experiments up to a 90° wake age, after which the coarsening of the background mesh combined with the vortex tracking algorithm kick in as the limiting factors. It was also observed that refining the background wake mesh fourfold improved the tip vortex trajectory but did not make a significant difference to the performance predictions. This study establishes confidence in the predictive capabilities of the CFD methodology, which is then used to study the performance of hovering slatted rotor, the results of which are presented in the next chapter.

Chapter 4

Slatted Rotor Simulations

4.1   Overview

The CFD solution methodology described in Chapter 2 and validated in Chapter 3 is now used to study the performance of slatted rotors in hover. The two slat configurations studied are the S-1 and S-6, used in the study of Lorber et al. [25]. The effect of the leading slat on the rotor performance is explained through the spanwise airload and pressure distribution, in addition to the wake structure and surface streamline plots. The effect of the slat root and tip vortices convecting over the main blade element is captured through the use of appropriately refined meshes.

4.2   Slatted Rotor Geometry and Mesh System

A leading edge slat is added to the $50 - 90\%$ spanwise locations of the main rotor blade of the UH-60A helicopter. As mentioned earlier, the UH-60A main rotor has the SC1094R8 airfoil section in the midspan region. The leading edge slat configurations from the experiments were tested in forward flight with a blade having the SC2110 airfoil section in the mid-span region, which was generated from the SC1094R8 by making modifications to the leading edge portion, as shown in Fig. 3.1. The slatted rotor simultions in the current chapter are however performed

on a slatted rotor blade, which is generated by adding a leading slat to the desired spanwise extent of the baseline UH-60A rotor.

Figures 4.1 show results from 2-D CFD simulations of the baseline SC2110 and SC1094R8 airfoil along with the S-1 and S-6 slats. As can been seen from the figures, the minor differences in the airfoil geometry seen in Fig. 3.1, do not cause significant changes to the aerodynamics of the slatted configurations. In addition, it is also seen that the difference in the aerodynamic parameters for the two baseline airfoils are also negligible at the low moderate angles of attack, which one expects to encounter in a hovering flight condition.

The 2-D simulations are performed with all the airfoil sections assumed to be operating under freestream conditions, unlike inside a wind tunnel, as modeled in Chapter 3. The freestream Mach number was 0.3, which is the Mach number around the mid-span region of the UH-60A rotor. The S-A turbulence model was used in all the calculations and the Reynolds number was 4.14 million.

Figure 4.2(a) shows the top view of the slatted rotor geometry. The slat extends from $0.5R - 0.9R$ of the main. blade. Figure 4.2(b) shows the two slat elements along with the main blade element. The slats are given the same geometric blade twist as the main UH-60A rotor blade (Fig. 3.12).

The slat mesh has a C-O topology, shown in Fig. 4.3(a), with $129 \times 77 \times 65$ points in wraparound, spanwise and normal directions respectively. The main blade and background meshes are unchanged from the validation study for the baseline UH-60A rotor (Sec. 3.3.1). The top view of the slat, blade and background meshes is shown in Fig. 4.3(b). During the course of the simulation, the Implicit Hole
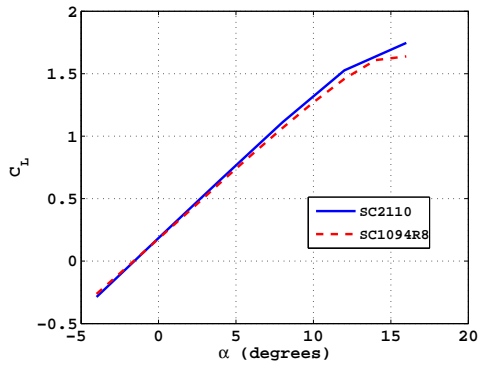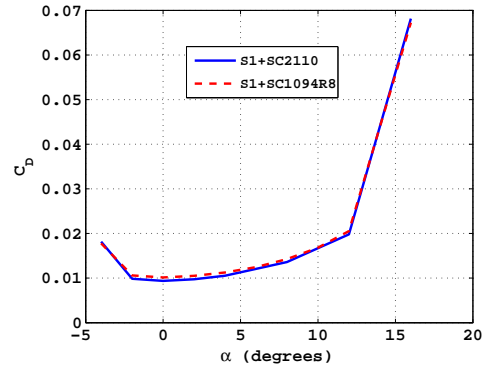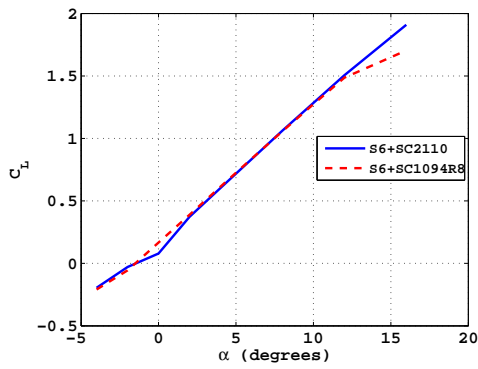
(a) C_L comparison for Airfoils alone
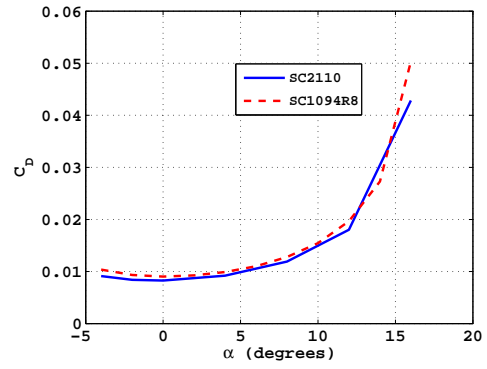
(b) C_D comparison for Airfoils alone
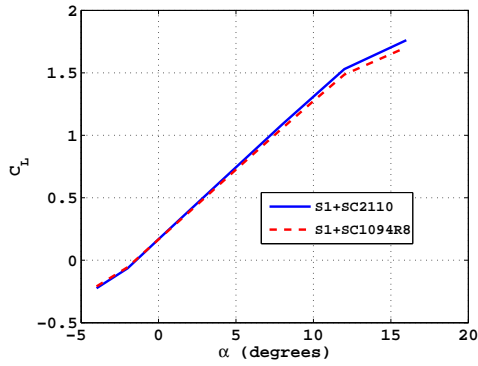
(c) C_L comparison for Airfoils with S-1 Slat (d) C_D comparison for Airfoils with S-1 Slat
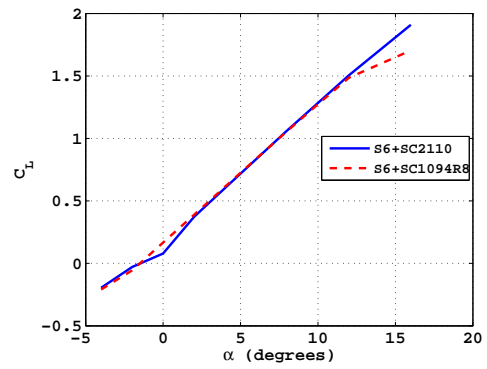
(e) C_L comparison for Airfoils with S-6 Slat (f) C_L comparison for Airfoils with S-6 Slat

Fig. 4.1: Comparison of S-1 and S-6 with SC2110 and SC1094R8 Main Airfoil Sections
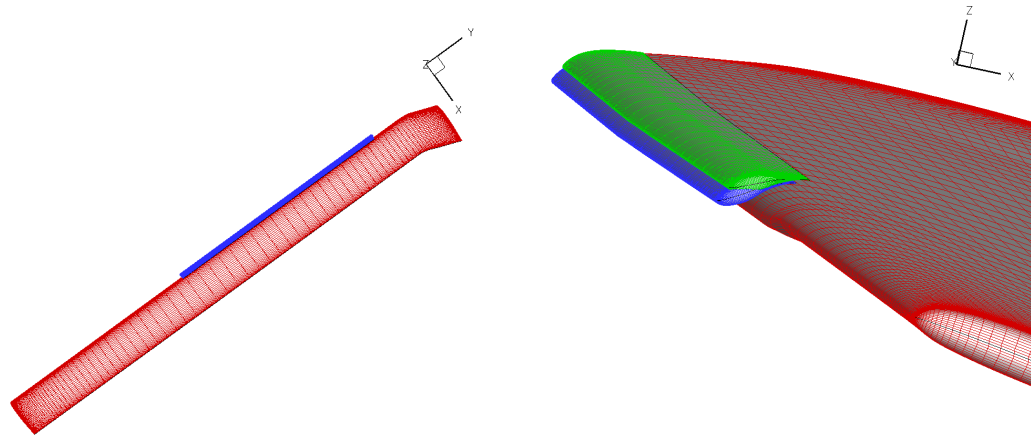
(a) Top view of Slatted Rotor   (b) S-1(Green) and S-6(Blue) Slats

Fig. 4.2: Slatted Rotor Geometry

Cutting (IHC) algorithm determines the connectivity between the various meshes participating in the solution process.

(a) C-O Mesh System on the Slat   (b) Top View of the Mesh System Blue:Slat

Red:Blade Black:Background

Fig. 4.3: Slatted Rotor Mesh System

4.3   Slatted Rotor Performance Comparison

A collective angle sweep similar to the baseline rotor validation is carried out for the slatted rotor with the S-6 slat. The structural deformations used are the same as described in Sec. 3.3.1. The deformations are applied to the slat in the sam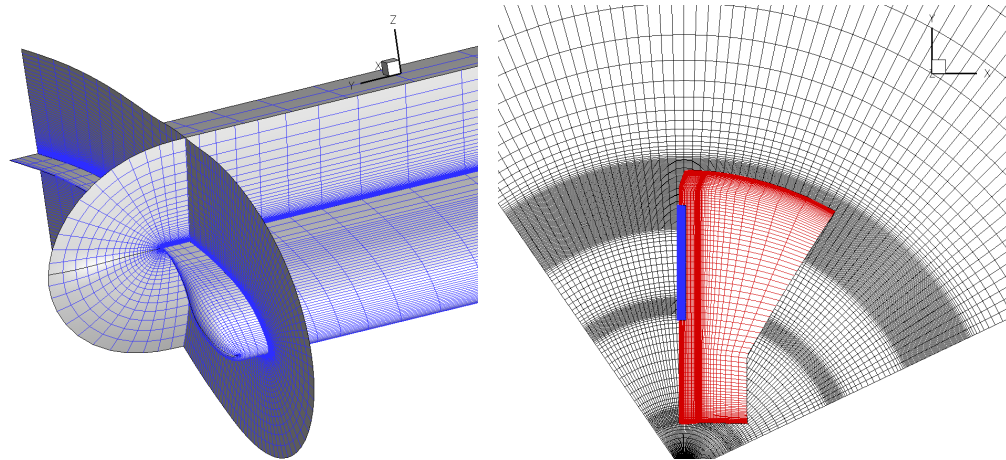e manner as the main blade element and therefore for the purpose of deformations, the slat and the main blade element behave as a single entity.

Figure 4.4 shows the predicted performance of the S-6 slatted rotor compared against predictions for the baseline UH-60A rotor. The calculations show that the slatted rotor, for the same collective angle as the baseline rotor, produces a slightly lower thrust coefficient while incurring a power penalty. It is also observed that the power penalty is larger at lower collective angles, which is consistent with the performance of the S-6 slat at very low angles of attack. The overall result is that there is a significant deterioration in the FM for the slatted rotor at every collective angle. Interestingly, the slatted rotor is also unable to provide any improvement even at the higher collective angles (15°) and shows the same drop-off in performance as the baseline rotor. At this point it would be instructive to investigate the spanwise distribution of airloads to further understand the predictions for the slatted rotor.

Airloads Computation For Slatted Rotors

For the purpose of airloads computation, the forces and moments are transferred from the slat element onto the main blade element. The reference axes for the airloads is the elastic axis (E.A) of the main blade element, about which all the
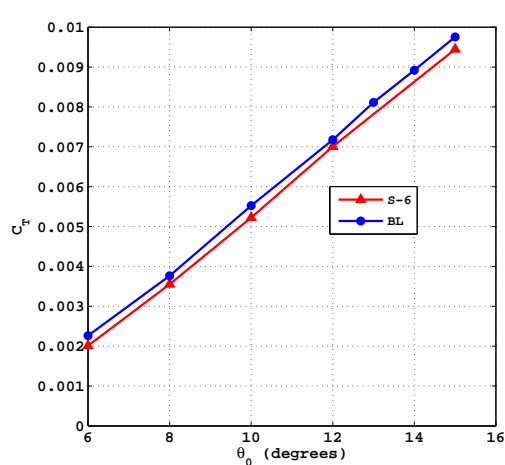
(a) C_T vs Collective Angle
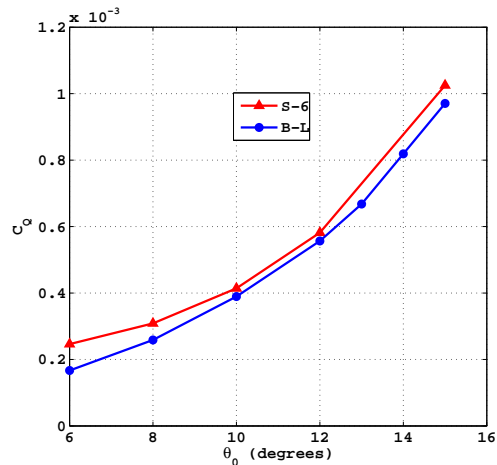
(b) C_Q vs Collective Angle
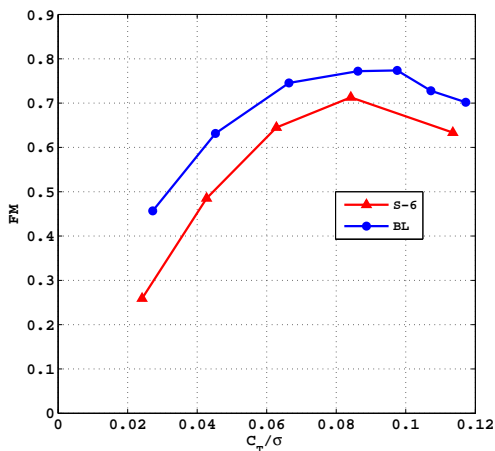
(c) FM vs C_T/σ

Fig. 4.4: S-6 slatted rotor performance predictions using the baseline main element mesh

airloads (forces and moments) are computed. The airloads transfer from the slat to the main element is achieved by transferring the forces and moments from the slat onto the appropriate spanwise location of the main blade. For every spanwise location on the main blade that lies between two spanwise lcoations of the slat, the

airloads are linearly interpolated. Once the slat airloads are transfered to the main blade, this contribution is added to that of the main blade itself and the appropriate transformation matrix is then applied to convert the loads from the deformed frame to the undeformed reference. The procedure is described in greater detail in [27].

Airloads Comparison at 10° Collective

Figures 4.5 (a) and (b) compare the spanwise distribution of the normal (lift/thrust) and chord wise (drag) forces for the baseline and slatted rotors at a 10° collective angle. From the spanwise distribution of the normal force, it can be seen that the slatted rotor produces a lesser amount of lift compared to the baseline rotor near the slat root and tip $(r/R = 0.50, r/R = 0.90)$. In addition, there is also a loss in lift outboard of the slat tip, in the region of the main blade tip. However, away from the slat root and tip, the slatted rotor has a similar lift distribution as the baseline rotor. The spanwise drag force on the other hand shows that the slatted rotor consistently has higher drag values in the slatted region, with the largest increment being near the slat root and tip.

The large increase in the drag and decrease in lift near the slat root and tip merits closer study. The flow field on the main blade, near the slat root and tip is influenced by the vortices trailed from the slat and accurately capturing these vortices and their interaction with the main blade element is essential for airload predictions. The mesh refinement studies undertaken during the course of this work are detailed in the next section.
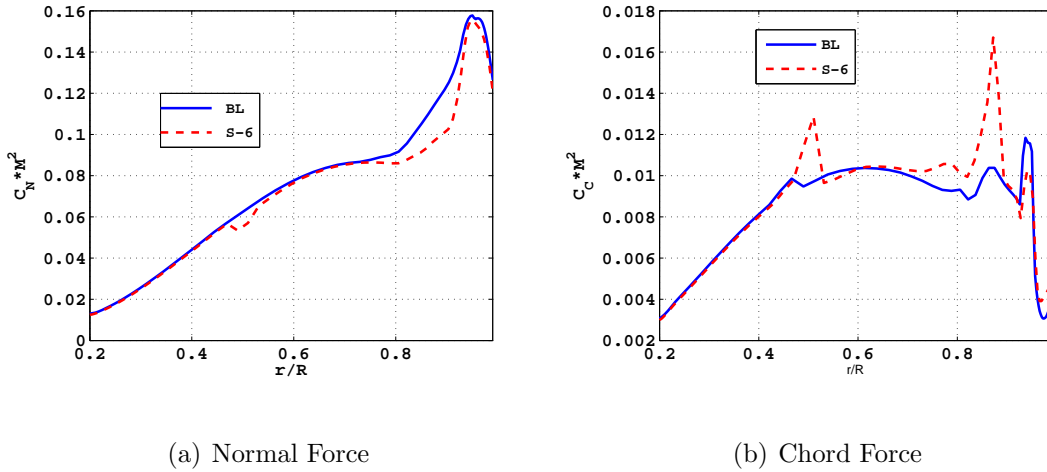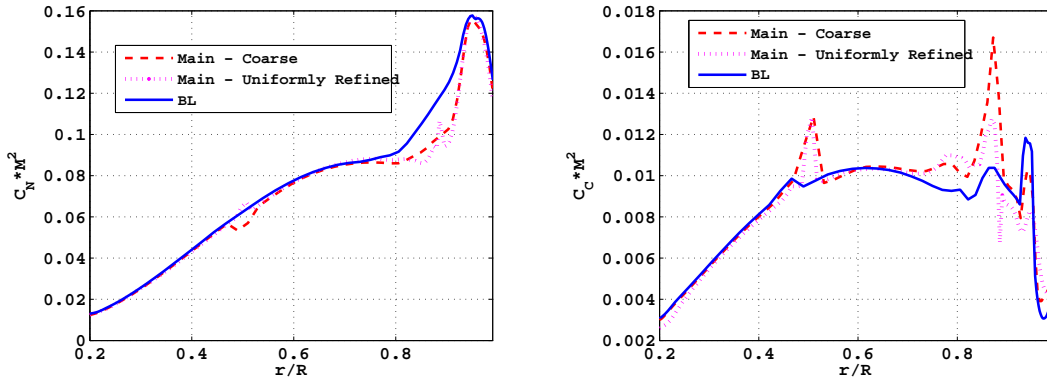
(a) Normal Force   (b) Chord Force

Fig. 4.5: Airloads comparison for S-6 and Baseline rotors at 10° collective

4.3.1 Uniformly Refined Main Blade Mesh

As a first attempt to better capture the slat root and tip vortices, a uniformly refined main element mesh, with double the number of points in each direction was generated. This new mesh has dimensions $265 \times 259 \times 121$ in the wraparound, spanwise and normal directions respectively. Fig. 4.6 compares the airloads distribution obtained using the coarse and fine main element meshes. Also shown are the airloads for the baseline UH-60A rotor. It can be seen that the effect of the slat root and tip vortex is more localized on the uniformly refined mesh compared to the coarse mesh. Also, the effect of refinement is more profound on the chord force compared to the normal force and the general trend of the slatted rotor producing less thrust in the outboard slatted regions, compared to the baseline rotor and a corresponding increase in power in these regions is maintained by the uniformly refined mesh.

Fig. 4.7 shows the contours of the X vorticity behind the blade and the slat, in the region of the blade and slat tips. As can be seen, the slat tip vortex on the

(a) Normal Force   (b) Chord Force

Fig. 4.6: Airloads comparison for S-6 at 10° collective with coarse and uniformly refined main element mesh

coarse mesh is distorted considerably and does not have the tight structure of the blade tip vortex. It should be noted that even on the coarse main element mesh, the spacing near the blade tip is at least one order of magnitude lower than over the rest of the blade, allowing the tip vortex to be resolved accurately. The uniformly refined mesh with its smaller spacing compared to the coarse mesh resolves the slat tip vortex better, both in the spanwise and chordwise directions, but is still unable to match the profile of the blade tip vortex.

The spacing on the slat mesh near the slat tip is of the order of the blade tip spacing. However, during the course of the solution, when the mesh system switches from the slat mesh onto the main element mesh, the spanwise spacing increases by at least one order of magnitude. Although, not shown here, a similar situation occurs near the slat root. This leads to the smearing of the slat tip and root vortices, both on the coarse and uniformly refined main element meshes. The
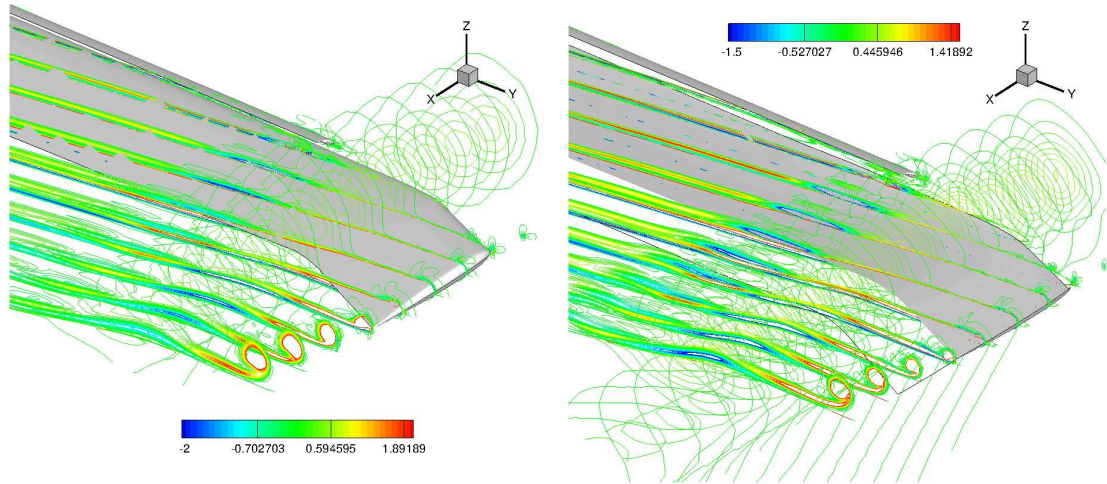
(a) Coarse Main Element Mesh   (b) Uniformly Refined Main Element Mesh

Fig. 4.7: X Vorticity Contours for S-6 at 10° collective with coarse and uniformly refined main element mesh

spacing in the normal direction on the coarse mesh is fine enough and there is no additional advantage to be gained by refining in this direction. From the discussion in this section, it is clear that to appropriately capture the effect of the slat root and tip vortices, the spacing on the main blade element in these locations has to be the same as that near the blade/slat tip. A main element with this grid spacing is generated and the results on this mesh are discussed in the next section.

4.3.2   Slat Root and Tip Refined Main Blade Mesh

As discussed in the previous section, a main blade mesh with refinement near the slat root and tip is generated. The spanwise spacing on the various main element meshes used in the slatted rotor simulations is shown in Fig. 4.8. As can be seen from the figure, the spacing on the original coarse main element mesh is very large,

not only near the slat root and tip, but also in the slatted regions, compared to the spacing on the slat. The information transfer at the slat/blade interface therefore takes place between two cells, which are vastly different in their sizes, with one cell belonging to the slat mesh and the other to the blade mesh. In regions of high gradients, this can lead to incorrect information transfer between the meshes. The refined mesh was therefore built not only to have very fine spacing near the slat root and tip but also to have comparable spacing to the slat, in the slatted regions to have accurate information transfer.
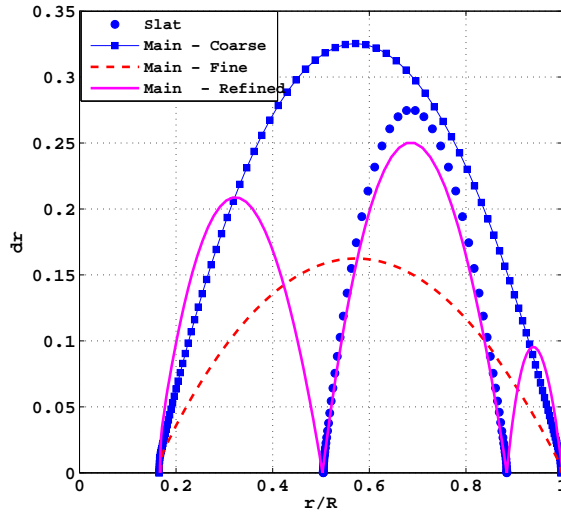
Fig. 4.8: Spanwise spacing on the various meshes used for slatted rotor runs

Figure 4.9 shows the main element and slat surface meshes near the slat tip. The restriction of having a reasonable stretching ratio in the spanwise direction for the refined meshes pushes the total number of points in the spanwise direction to 309. The number of points in the wraparound and normal directions remains unchanged from the coarse mesh. The number of points used in each mesh in the

slatted rotor simulations is summarized in Table 4.1.
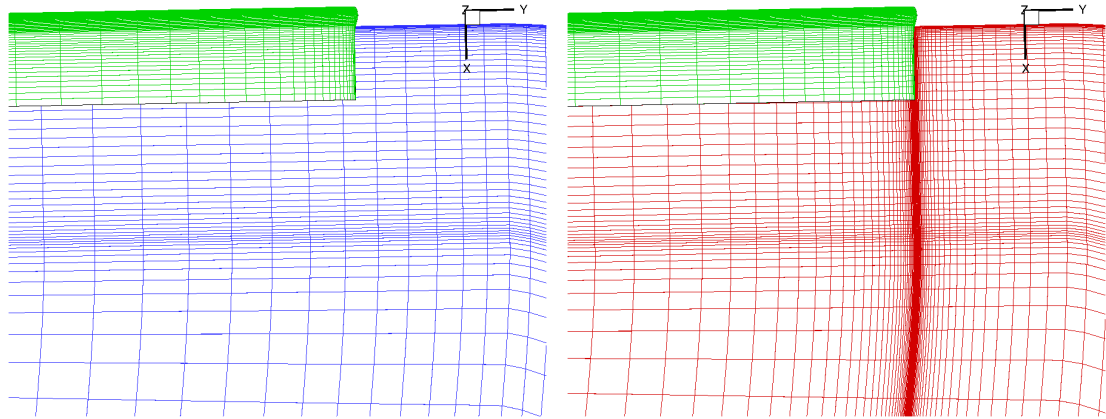
(a) Coarse Main Element Mesh   (b) Refined Main Element Mesh

Fig. 4.9: Coarse and Refined main element meshes near the slat tip

Mesh	Dimensions	Mesh points (in millions)
Baseline	133×130×61	1.05
Baseline - Uniformly Refined	265 × 259 × 121	8.3
Baseline - Root and Tip Refined	133×309×61	2.5
Slat	129×77×65	0.65
Background	67×174×112	1.3

Table 4.1: Number of points used in the various meshes

A collective angle sweep similar to those described earlier was carried out for both the S-1 and S-6 slatted rotors using the refined mesh. The results are described in the next section.

4.3.3 Performance Comparison with the Refined Main Element Mesh

Figures 4.10- 4.12 show the computed performance coefficients for the S-1 and S-6 slatted rotors compared against the values of the baseline UH-60A rotor. Also shown are predictions for the S-6 rotor using the coarse main element mesh. It can be seen that the use of the refined mesh improves the predictions significantly.
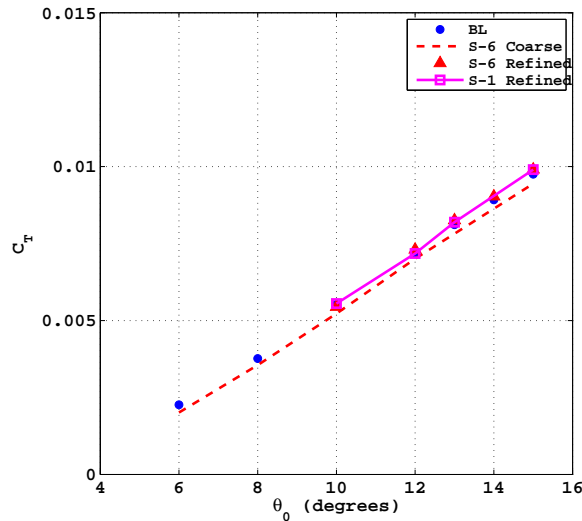
Fig. 4.10: C_T vs Collective angle comparison using the refined main element mesh

It is seen that at the lower collective angle of 10°, the S-1 slatted rotor has a slightly larger thrust coefficient compared to the baseline rotor and that the S-6 slatted rotor has a slightly lower thrust coefficient. The differences are not very apparent from the figure, but a look at the actual computed values, shows differences to the tune of 2% between the various rotors. At the collective angle of 12°, which is close to the point of maximum FM for all rotors, both the slatted rotors and the baseline rotors are seen to be producing the same amount of thrust and as the

collective angle is increased beyond this point, the slatted rotors result in slightly larger thrust coefficients, with the S-6 slatted performing better than the S-1 at these higher angles. Throughout the collective angle range, the refined mesh predicts larger values of C_T for the S-6 rotor compared to the coarse mesh.
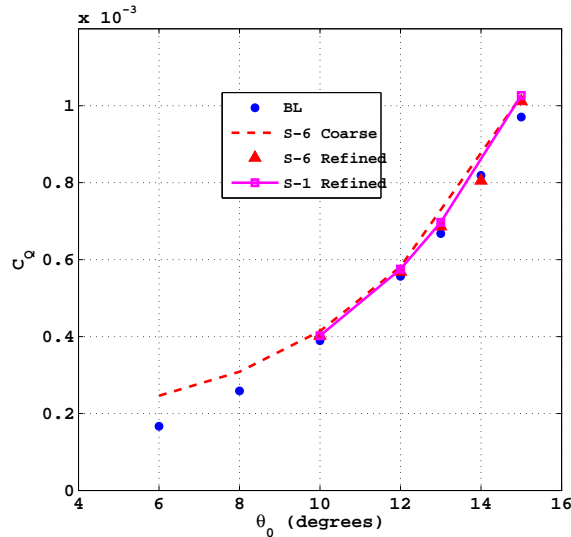
Fig. 4.11: C_Q vs Collective angle comparison using the refined main element mesh

From the variation of the power coefficient with collective angle (Fig. 4.11), it is seen that at the lower collective angle of $10°$, the S-6 has the largest value for the power coefficient. At the higher collective angles, the slatted rotors have slightly higher values compared to the baseline rotor, with the S-6 slat performing better compared to the S-1 slat. The values predicted by the refined mesh are smaller compared to the coarse mesh values across the collective angle range.

The small differences in C_T and C_Q for every collective angle, between the coarse and refined meshes, combined to produce a significant change in the computed value of FM. It is seen that at the lower collective angle of $10°$, the baseline rotor
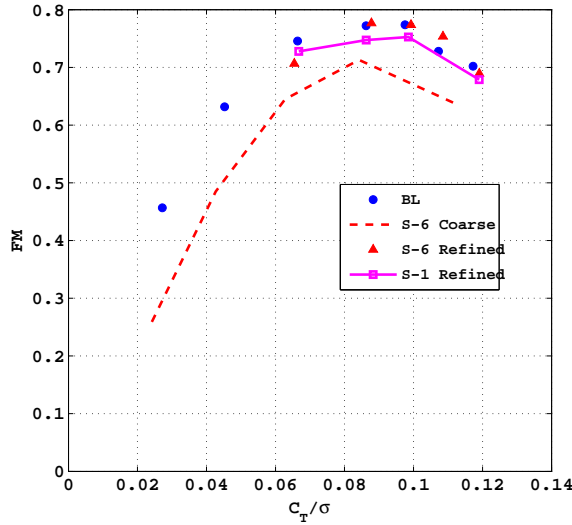
Fig. 4.12: FM vs C_T/σ comparison using the refined main element mesh

has the highest figure of merit, followed by the S-1 and then the S-6 slatted rotors. As the collective angle increases, the performance of the S-6 and the baseline rotors becomes comparable. The S-1 rotor however has lower values of FM compared to the other two at all angles except 10°. The drop in FM at a collective angle of 15°, which was observed with the coarse mesh, is also present with the refined mesh and for both the slatted rotors and is probably a consequence of the aerodynamic behavior in regions without the slat.

Tables 4.2 and 4.3 list the thrust and power coefficients at the moderate and higher collective angles, obtained for the different rotors and meshes used in the simulations.

The effect of mesh refinement on the spanwise airloads is analyzed in the next section. Also computed and shown are the spanwise distribution of inflow and effective local angle of attack. The effective angle of attack is obtained by adding to

θ_0	Baseline	S-6 Coarse	S-6 Refined	S-1 Refined
10	0.00552	0.00522	0.00544	0.00561
12	0.00718	0.00700	0.00730	0.00718
15	0.00975	0.00945	0.00991	0.00990

Table 4.2: Computed thrust coefficients for different rotors

θ_0	Baseline	S-6 Coarse	S-6 Refined	S-1 Refined
10	3.89×10^{-4}	4.14×10^{-4}	4.02×10^{-4}	4.02×10^{-4}
12	5.57×10^{-4}	5.82×10^{-4}	5.68×10^{-4}	5.74×10^{-4}
15	9.70×10^{-4}	1.03×10^{-3}	9.99×10^{-4}	1.03×10^{-4}

Table 4.3: Computed power coefficients for different rotors

the geometric angle of attack at each section, the elastic twist and the induced angle due to the inflow. The inflow shown is obtained by first averaging the z component of velocity at two planes on the background mesh, which are located $0.1c$ above and below the rotor and then over the azimuth to account for the presence of the blade.

4.3.4 Airloads Comparison with the Refined Main Element Mesh

Fig. 4.13 shows the spanwise distribution of the normal and chordwise force for the S-6 slatted rotor obtained using the baseline (coarse) and refined main element meshes. It can be seen that the refined main element captures the effect of the slat root and tip vortices in a more localized manner compared to the baseline mesh. The sharp variation in airloads near r/R = 0.5 and r/R = 0.9 using the refined
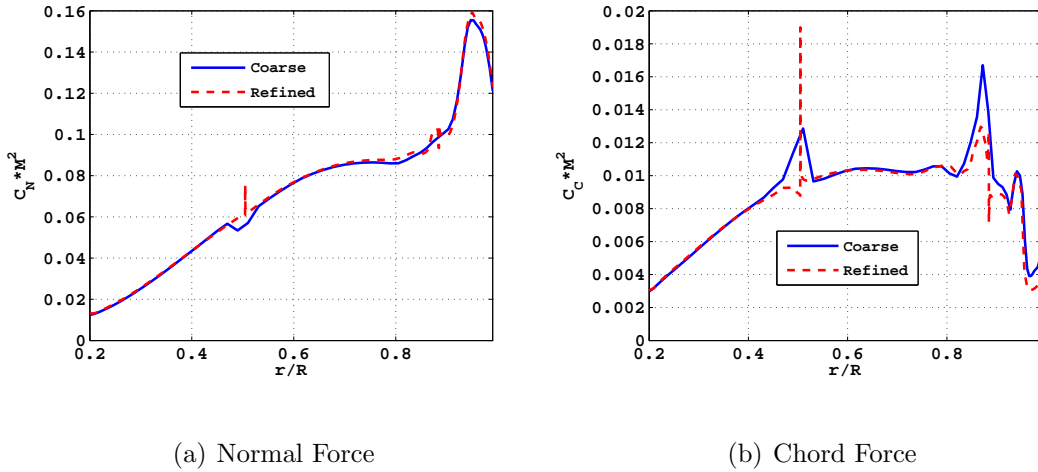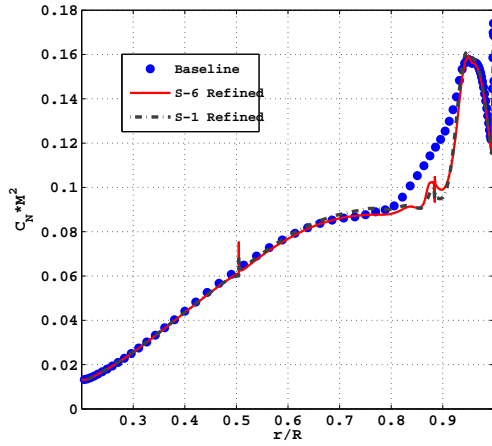
(a) Normal Force   (b) Chord Force

Fig. 4.13: S-6 rotor airloads comparison using baseline and refined meshes at 10°
collective

meshes shows that the slat root and tip vortices are being resolved more accurately
compared to the baseline mesh. Therefore, all the subsequent airloads comparisons
in this section, where the slatted rotors (S-1 and S-6) are compared against the
baseline UH-60 rotor are made using the refined main element mesh.

Fig. 4.14 shows the airloads and the inflow distribution for the baseline and
the slatted rotors at the 10° collective angle. A drop in the thrust levels is observed
(Fig. 4.14(a)) for the slatted rotor in the outer regions of the slat. The drop in
thrust is also accompanied by an increase in the drag (chord force) in these re-
gions(Fig. 4.14(b)). Fig. 4.14(c) shows the inflow distribution along the span for
both the slatted and the baseline rotors. Fig. 4.14(d) shows the variation of the ef-
fective angle of attack for the S-6 rotor with the refined mesh. From the figure it can
be seen that the slatted regions operate at small positive angles of 4°-7°. The small
local angle of attack explains the loss in thrust in the outboard slatted regions and is

92

(a) Normal Force
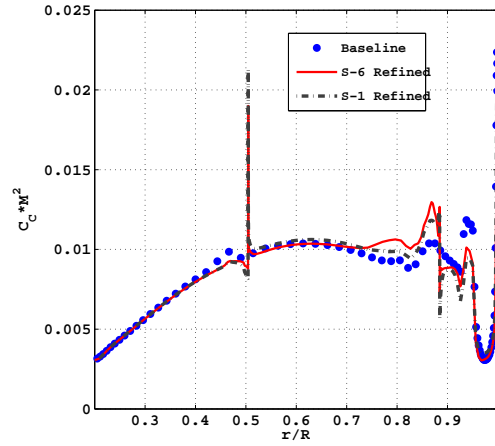
(b) Chord Force
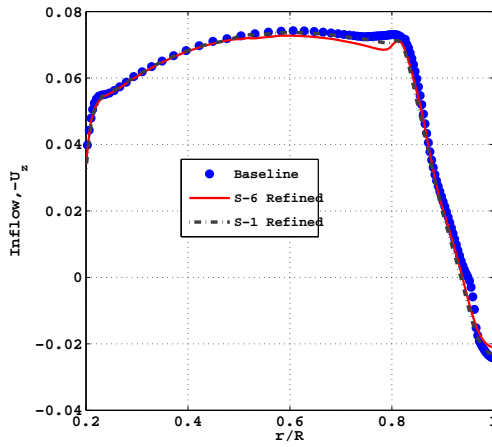
(c) Inflow

(d) Effective AoA

Fig. 4.14: Airloads Comparison at 10° collective

consistent with 2-D predictions for the slatted airfoils, where the slat was negatively loaded at the lower angles and in addition it is also known from experiments that the slatted airfoils had a higher drag coefficient compared to the baseline airfoil at these lower angles.

Fig. 4.15 compares the airloads and inflow for the two rotors at 12° collective
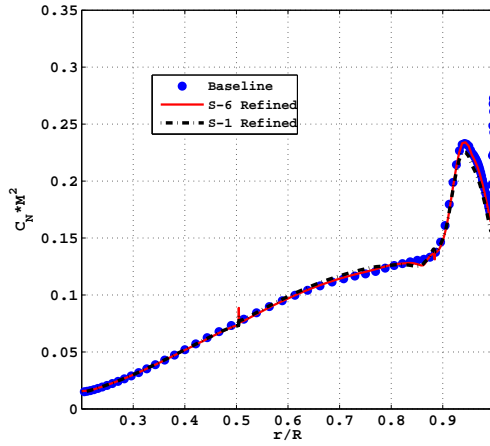
(a) Normal Force
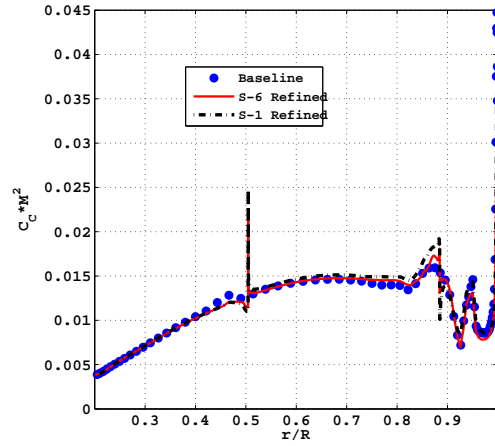
(b) Chord Force
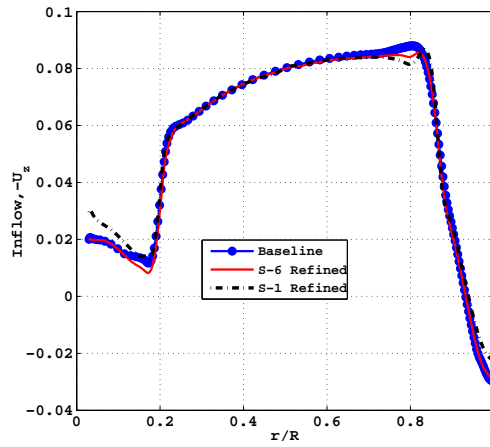
(c) Inflow
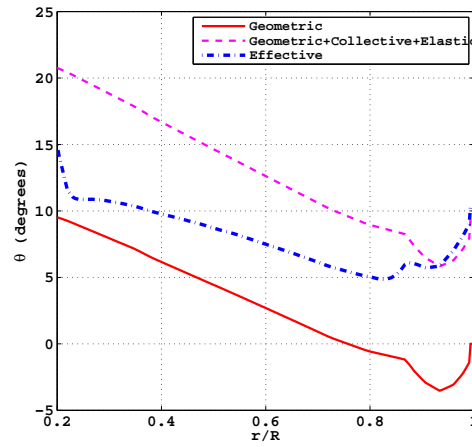
(d) Effective AoA

Fig. 4.15: Airloads Comparison at 12° collective

angle. This collective setting also corresponds to the thrust condition around which the maximum FM is observed. The distribution of the normal force (Fig. 4.15(a)) shows that both the slatted and the baseline rotor are producing roughly the same thrust and the values predicted using the baseline and refined meshes for the S-6 configuration are in very close agreement. The distribution of the chordwise force

also shows a slight increase in drag for the S-1 slatted in the outboard slatted regions, which leads to a drop in the figure of merit for the S-1 slatted rotor.
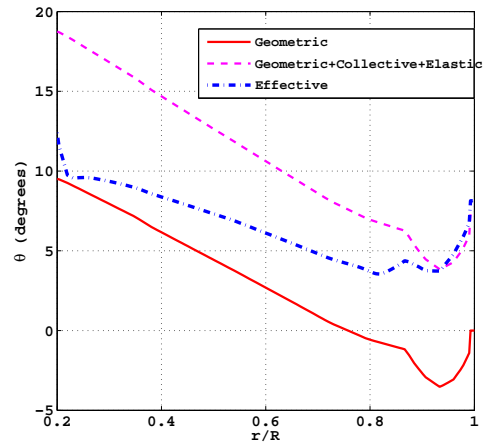

(a) Normal Force

(b) Chord Force

(c) Inflow

(d) Effective AoA

Fig. 4.16: Airloads Comparison at 15° collective

Airloads at the highest collective setting of 15° are shown in Fig. 4.16. The normal force distributions for all the rotors are very similar as can be seen from Fig. 4.16(a). A slight drop in thrust inboard of the slat tip and a small increase in

thrust outboard of the same is observed. This is due to the presence of a stronger slat tip vortex at this larger thrust (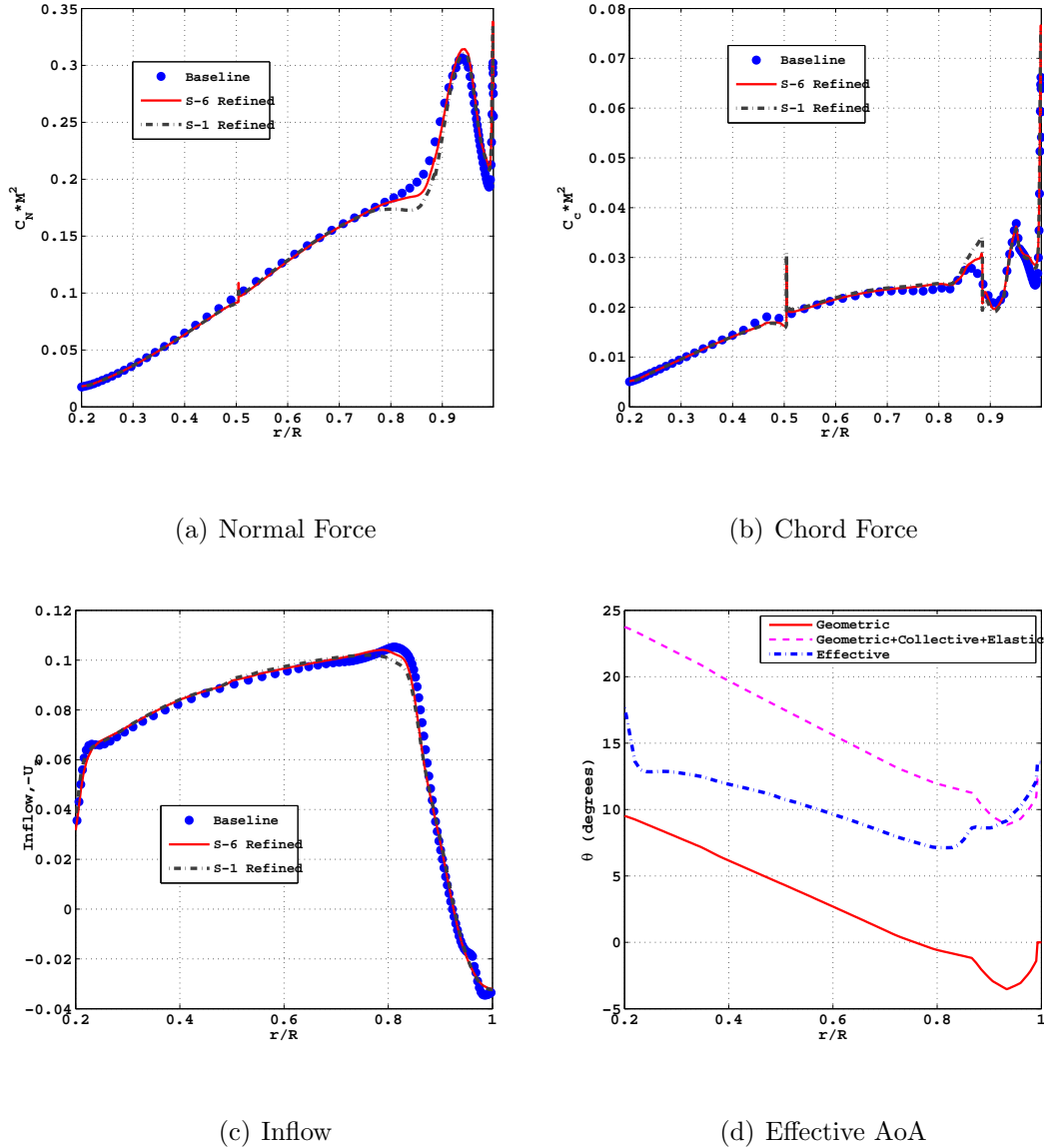collective) compared to the earlier cases. It is also seen that the drop for the S-1 slat is larger compared to the S-6 slat. There is a steep increase in the chord force (drag) in the tip region (r/R = 0.9-1.0) for the baseline rotor (Fig. 4.16(d)) over the previous collective setting of 12°. This accounts for the drop in the FM (Fig. 4.12). A similar trend is observed for the slatted rotor using the refined mesh, with a slightly larger increment than for the baseline rotor. The increase in drag in the tip region is due to shock induced separation, which occurs due to a combination of large local Mach numbers and the increase in the local angle of attack owing to the increased collective setting. An investigation of the wake structure, pressure distributions and surface streamline pattern in the subsequent sections confirms the occurrence of flow separation.

4.3.5 Pressure Distribution Plots

The non-dimensional pressure coefficient C_p is plotted for the various rotors at four different radial locations and at collective angles of 10° and 15°. The radial locations are chosen to lie in the slatted region, with r/R = [0.55,0.675,0.775,0.865].

Figures 4.17 and 4.18 show the pressure distribution on the main element for the baseline, S-1 and S-6 rotors. The 'slat effect' is one of the five major multi-element effects identified by Smith [16] and the effect of the LE slat is to lower the effective angle of attack over the main element which results in a smaller pressure peak over the main element of a multi-element airfoil. It can be observed from the

(a) 10°, r/R = 0.55   (b) 15°, r/R = 0.55

(c) 10°, r/R = 0.675   (d) 15°, r/R = 0.675

Fig. 4.17: Main Element Pressure Distributions at the two inboard sections for 10° and 15° collective angles. BL Upper - Purple, BL Lower - Blue, S-6 Upper - Green, S-6 Lower - Red, S-1 Upper - Green dash, S-1 Lower - Red dash

figure that at the 10° collective setting, there is hardly any reduction in pressure peak over the main element and in fact there is a larger negative C_p on the main element in the outboard sections. This further suggests that at this moderate collective setting, there is no 'slat effect'.

At the 15° collective setting, there is a significant reduction in the pressure peak at all the radial locations except the one closest to the slat tip. At the radial location closest to the slat tip (r/R = 0.865), there is a large negative value for the

(a) 10°, r/R = 0.775 (b) 15°, r/R = 0.775

(c) 10°, r/R = 0.865 (d) 15°, r/R = 0.865
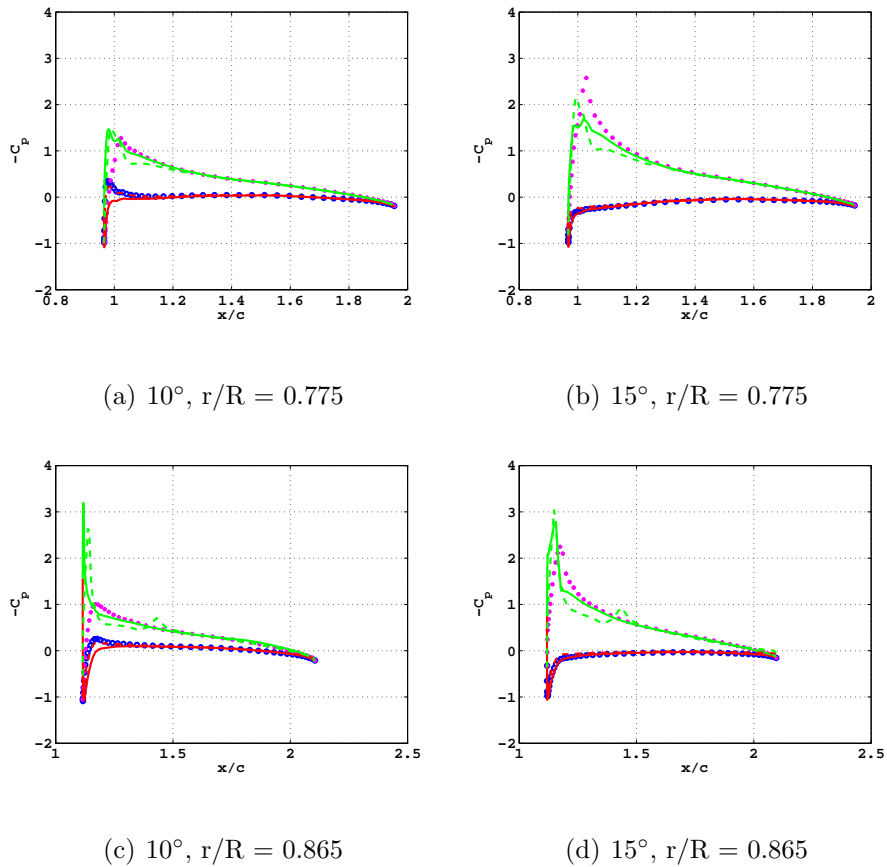
Fig. 4.18: Main Element Pressure Distributions at the two outboard sections for 10° and 15° collective angles. BL Upper - Purple, BL Lower - Blue, S-6 Upper - Green, S-6 Lower - Red, S-1 Upper - Green dash, S-1 Lower - Red dash

pressure coefficient accompanied by a sharp drop. This adverse pressure gradient is more severe for the slatted rotor compared to the baseline rotor.

The pressure distributions on the slat are shown in Figures 4.19 and 4.20. It can be seen that at the lower collective angle the S-6 slat is producing close to zero lift (the contribution of the skin friction force to the lift is negligible) in the inboard regions and negative lift in the outboard regions. At the 15° collective angle, there is a significant improvement in the lifting characteristics of the inboard sections. In
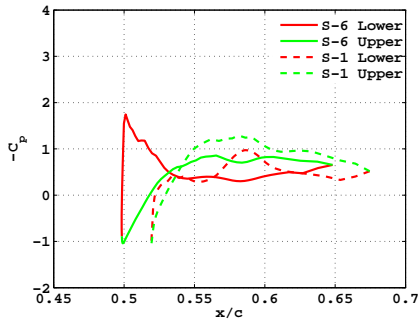
(a) 10°, r/R = 0.55   (b) 15°, r/R = 0.55
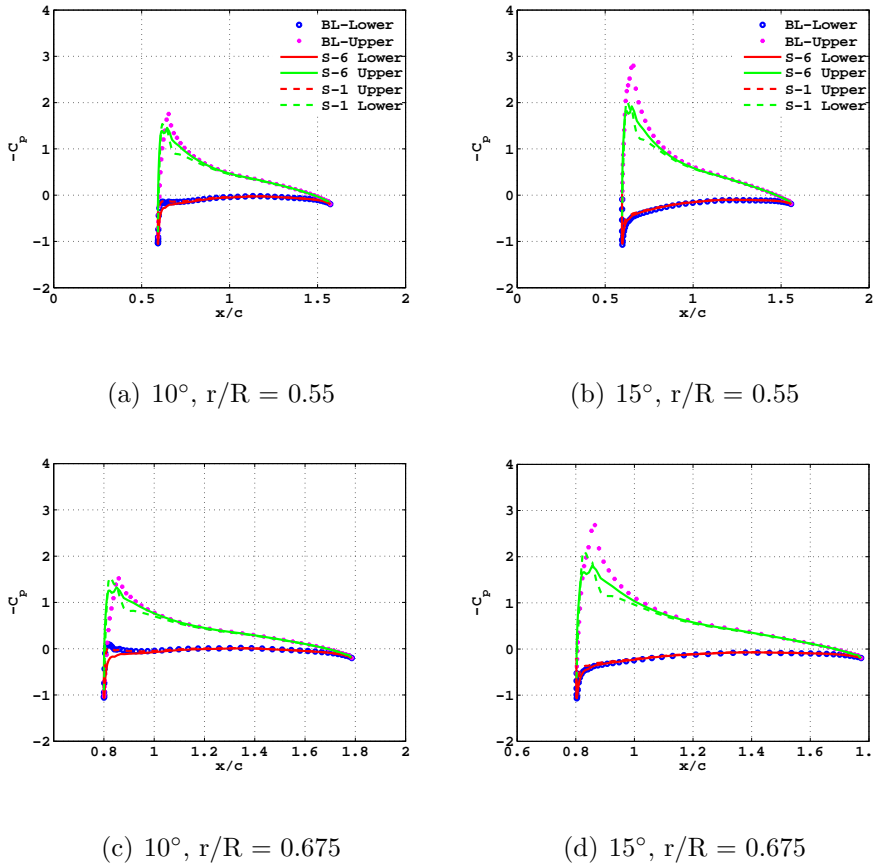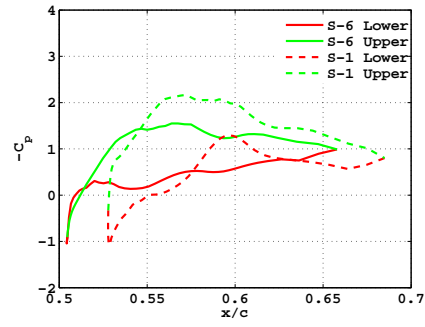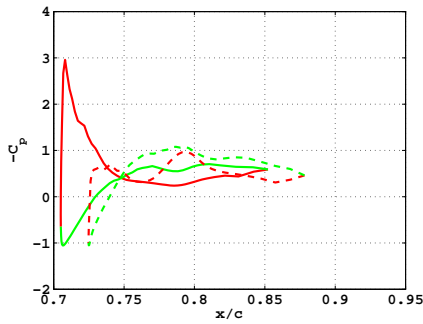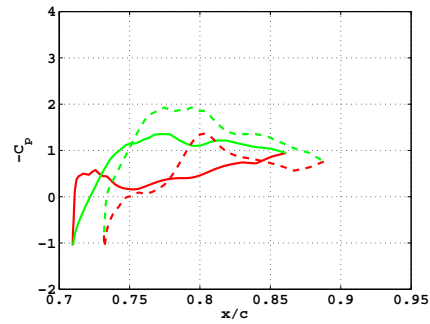
(c) 10°, r/R = 0.675   (d) 15°, r/R = 0.675

Fig. 4.19: Slat Pressure Distributions at the two inboard locations for 10° and 15° collective angles. S-6 Upper - Green, S-6 Lower - Red, S-1 Upper - Green dash, S-1 Lower - Red dash

addition, at the 10° collective angle, there is an adverse pressure gradient on the lower surface of the slat, in the outboard sections. This leads to a region of separated flow on the lower surface of the S-6 slat and is consistent with the 2-D predictions for this configuration at low angles of attack.

(a) 10°, r/R = 0.775   (b) 15°, r/R = 0.775

(c) 10°, r/R = 0.865   (d) 15°, r/R = 0.865
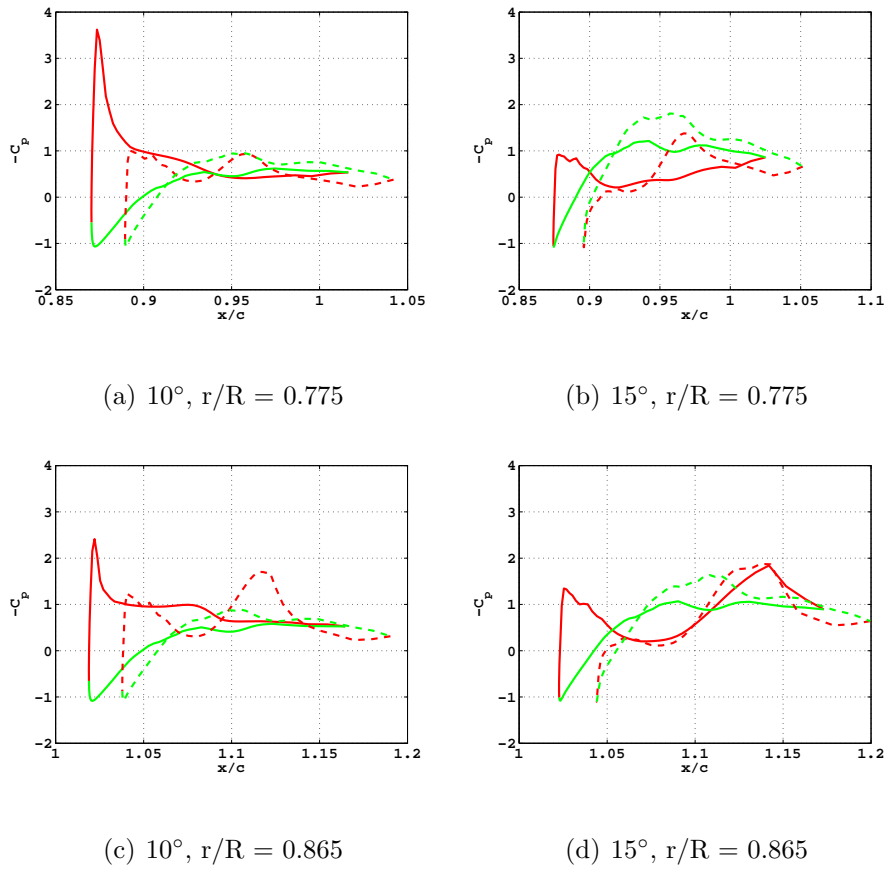
Fig. 4.20: Slat Pressure Distributions at the two outboard locations for 10° and 15° collective angles. S-6 Upper - Green, S-6 Lower - Red, S-1 Upper - Green dash, S-1 Lower - Red dash

4.3.6 Surface Streamlines and Wake Structure

Surface Streamlines

Fig. 4.21 shows the upper surface streamline patterns at 10° and 15° collective angles for the baseline, S-1 and S-6 slatted rotors respectively. The streamline patterns are very similar for all the three rotors and this is consistent with observed trends in airloads, performance quantities and the pressure distributions.

The streamline patterns indicate the presence of a re-circulation zone near the blade tip for the 15° collective angle. This is an outcome of the shock-induced separation in the region, which occurs due to a combination of high local Mach number (M_{tip} = 0.65) and relatively large local angle of attack due to the high collective setting.

The limiting factor for the UH-60A rotor in hover, therefore, is the shock induced flow separation which occurs in the tip region. This also inhibits the ability of the LE slats to raise the stall boundary, like in the case of forward flight, where the slats can achieve this by preventing dynamic stall. One possibility to have the leading edge slats extend all the way to the tip of the blade. However, with the high local Mach numbers near the tip, the drag on the slatted sections might become prohibitively large. A detailed study of transonic flow around slatted airfoil sections might provide insights into the possible benefits of extending the LE slats to the tip of the rotor blade.

Surface Vorticity Contours

Figure 4.22 shows the contours of X vorticity near the slat root and tip. It can be seen that using the refined mesh on the main element captures a tighter vortex structure near the slat root and preserves it for longer compared to the coarse and uniformly refined meshes (4.7). The observations near the slat tip are also similar, with the slat tip vortex being captured while it convects over the main blade element. However, the profile of the slat tip vortex is not as well defined compared to the root vortex. This is probably due to the interaction of the slat tip vortex with the
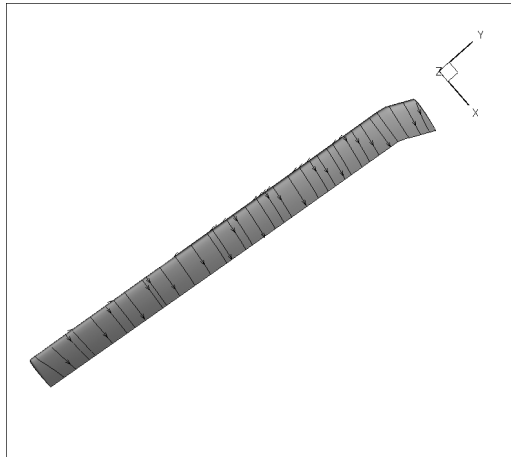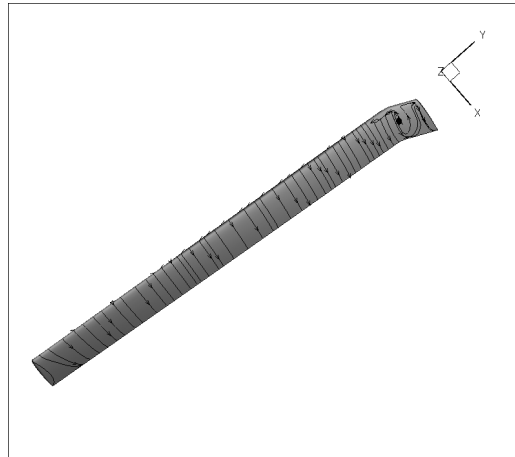
(a) BL at 10°   (b) BL at 15°
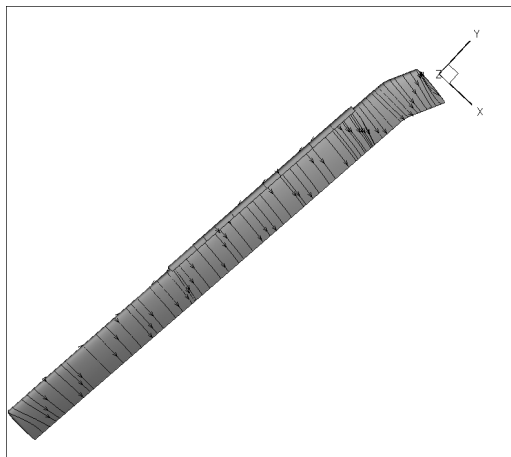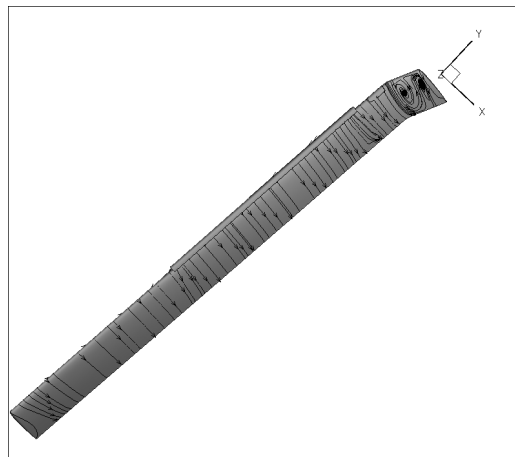
(c) S-1 at 10°   (d) S-1 at 15°
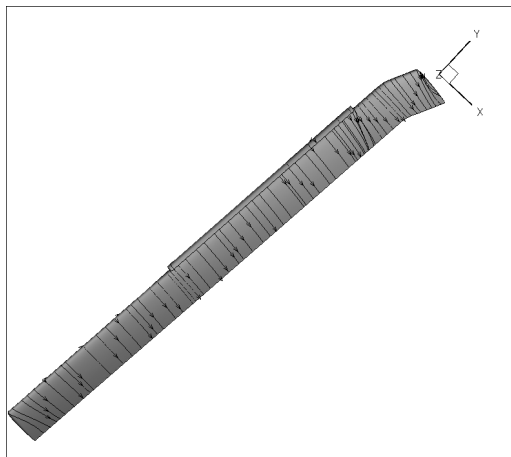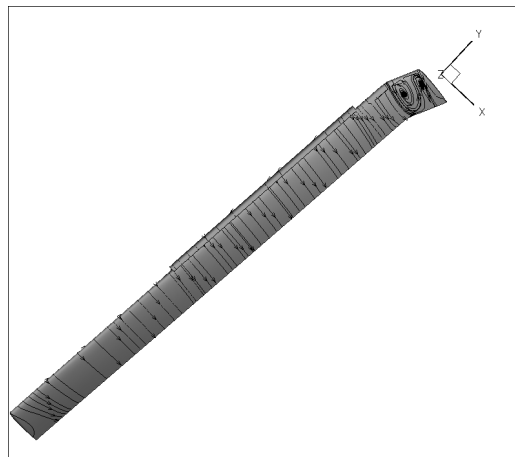
(e) S-6 at 10°   (f) S-6 at 15°

Fig. 4.21: Upper Surface Streamlines at 10° and 15° collective angles

first returning vortex of the preceding blade. Also seen is the interaction of slat tip and first returning vortex with the blade wake, which gives rise to vorticity of the opposite sense.
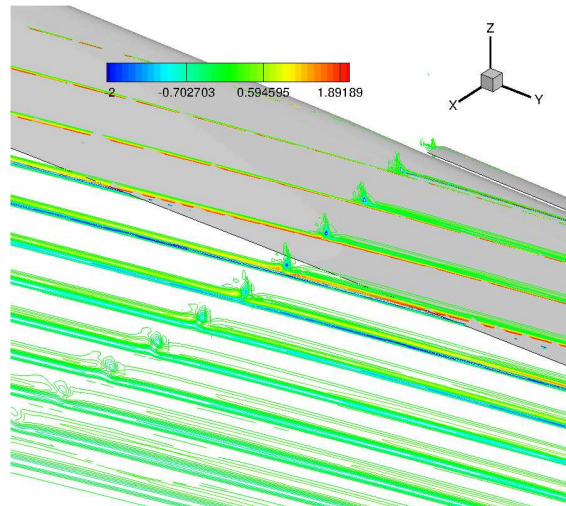
(a) Slat Root
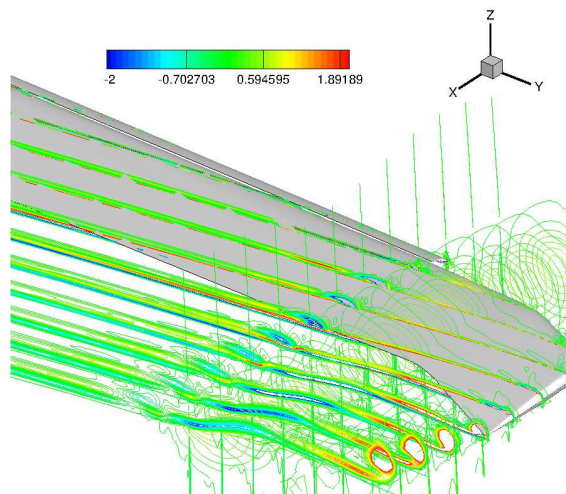
(b) Slat Tip

Fig. 4.22: Surface Vorticity near the Slat Root and Tip for S-6 slat at 12° collective

4.4 Summary

This section analyzed the performance of slatted UH-60A rotors using CFD predictions. A detailed analysis of the airloads was conducted and some of the specific observations are listed below.

- The slatted rotor performance was comparable to that of the baseline rotor at the higher collective angles. Between the two slat configurations analyzed, the S-6 slatted rotor had a better performance compared to the S-1 slat. At the moderate and low collective angles, the slatted rotors performed slightly worse compared to the baseline UH-60A rotor.

- The coarse and uniformly refined main element meshes predicted a performance penalty for the slatted rotors across the entire collective angle range. Analysis of the airloads and surface vorticity showed that these meshes smeared out the slat root and tip vortices over a larger spanwise region. A mesh with refinement near the slat root and tip, with spacing comparable to the slat and blade tips, captured the localized effect of the slat root and tip vortices more accurately.

- It was observed that at the moderate collectives, the S-6 slat has a negative contribution to the rotor lift whereas the S-1 slat has an almost zero contribution. This was due to the low local effective angle of attack, which is a combination of the collective, elastic twist and induced inflow angles. As the collective angle was increased, both the slats contributed positively to the lift.

- The limiting phenomena for the UH-60A rotor in hover is the shock induced stall which occurs near the blade tip at the higher thrust (collective) settings. As a consequence, the drag in this region increases, which pushes the power up and therefore the figure of merit drops. Since the stall occurs outboard of the slatted regions, even slatted rotors are limited by this phenomenon.

Chapter 5

Conclusions

In their quest to expand the existing flight envelope, rotorcraft designers have to overcome limitations which are inherent in the design of current generation helicopter blades. One such limitation is due to the phenomenon of *dynamic stall*, which occurs on the retreating side of the rotor disk. The objective of mitigating dynamic stall has resulted in many new blade concepts. Active control of dynamic stall by employing methods of active flow control, although very effective, is more complex to implement compared to concepts such as variable geometry or multi-element airfoil concepts.

Leading Edge (LE) slats are one of the two multi-element airfoil concepts under consideration, the other being Trailing Edge Flaps (TEFs). LE slats have found extensive use on fixed wing aircraft as a device to enhance lift at low speeds. LE slats increase the maximum lift coefficient of an airfoil section by delaying the onset of stall. Early wind tunnel testing of slatted rotorcraft airfoil sections demonstrated significant improvements to the static lift coefficient over the baseline airfoil section. Recent wind tunnel testing and analysis using comprehensive analysis codes and subsequent coupled CFD-CSD predictions demonstrated the effectiveness of LE slats in the mitigation of dynamic stall. One consistent trend observed across all the analyses and experiments was the increase in drag for the slatted sections at low

angles attack. Most of the analyses of slatted rotors have tended to focus on forward flight performance. Hover is an equally important flight condition which merits a thorough analysis.

The current work sought to analyze the performance of LE slats applied to the baseline UH-60A rotor, using a high-fidelity CFD solver. The analysis was conducted across a range of thrust settings and used overset meshes for efficient wake capture. A detailed analysis of the spanwise distribution of airloads and wake structure for both the baseline rotors was conducted, in addition to performance comparisons. The following sections of this chapter provide a brief summary of the analysis approach adopted in this work and then list the specific observations obtained from the CFD analysis. The chapter concludes with a brief discussion of the future research which can further the understanding of the aerodynamics of slatted rotors.

5.1   Summary

The objective of the present work was to use a high fidelity CFD solver to analyze the performance of LE slats applied to a UH-60A rotor in hover. To accomplish this, an existing Reynolds-Averaged Navier-Stokes (RANS) solver, Over-TURNS (Overset Transonic Unsteady RANS), was used during the simulations. The slat configurations were chosen from the study of Lorber et al. Of the many slat configurations proposed in the study, two configurations, the so called S-1 and S-6 were chosen. The S-6, with the slat being in a more nose down position, is a

high-lift configuration, which incurs a drag penalty at low angles of attack. The S-1 represents a compromise between the high-lift of S-6 and minimizing drag at low angles.

The CFD solver was first validated against two dimensional wind tunnel results for a SC2110 airfoil with and without the LE slats. CFD predictions of lift, drag and pitching moment coefficient compared well with the experimental values at moderate angles of attack, where the lift curve slope is linear and the flow stays completely attached over both the main element and the slat. CFD however, showed a delay in the stall prediction as compared to the angle measured from experiments. The observation was consistent across the simulations for both the baseline and the slatted airfoils. The essential slatted airfoil flow physics was however captured, with the stall angle for the slatted airfoil being higher compared to the baseline airfoil. In addition, it was also observed that CFD over-predicted drag at low angles for the slatted airfoil sections. One possible reason for the delay in stall prediction and the higher drag at low angles could be the assumption of fully turbulent flow. Turbulent boundary layers have the ability to withstand larger adverse pressure gradients, which explains the delay in the stall predictions. However, turbulent boundary layers also have a higher skin friction drag component compared to laminar boundary layers and at low angles of attack, the skin friction force is the major component of airfoil drag. The assumption of turbulent flow, especially over the slat, with its smaller chord (1/6 of main element chord) could possibly be a source of error in the drag predictions and requires further examination.

Following the 2-D validation study, the CFD solver was validated against avail-

able experiments for a four bladed UH-60A rotor in hover. The experimental data set chosen was from the model scale experiments of a hovering UH-60A rotor by Lorber et al. From an aerodynamic perspective, hover is a challenging flight condition, mainly because of the close proximity of the rotor wake to the rotor blade. To accurately capture the wake beneath a hovering rotor, the C-O type blade mesh was completely overset inside a cylindrical background mesh. The assumption of periodicity allowed for the simulation of a single blade and significantly reduces the computational expense. The implicit hole cutting (IHC) methodology was used to determine the connectivity information and perform overset interpolations at the boundaries of the participating meshes.

Comparisons of performance predictions against the experimental values showed good agreement at the low and moderate thrust conditions. It was also observed that the predictions were within the experimental error band as measured using data from two successive model scale experiments. The maximum computed figure of merit from simulations was slightly higher as compared to the measured value from the experiments. One possibly reason could be the use of approximate elastic twist, obtained from a comprehensive analysis code with lower order aerodynamic modeling, since the exact elastic twist of the experiments was not available in the public domain. Comparisons of tip vortex wake trajectory showed reasonable agreement with experimental values upto a 120° wake age. A mesh refinement study, with a doubly fine background mesh, showed a change in the airloads near the tip of the blade but did not affect the values of the performance parameters by a large amount.

5.2   Specific Observations

Having established confidence in the predictive capabilities of the CFD solver, a collective angle sweep was carried out for the slatted rotors, with the S-1 and S-6 slats extending from $50 - 90\%$ span of the rotor blade. Detailed conclusions from the slatted rotor simulations are enumerated below:

1. The slatted rotor simulations with the same main element mesh as the baseline rotor simulations, showed a significant performance penalty for the slatted rotors. An analysis of the spanwise distribution of airloads revealed a slight drop in thrust near the slat root and tip accompanied by an increase in drag (power), across the slatted region.

2. The use of a uniformly refined main element mesh showed improvements in the performance predictions, with the difference in thrust and power for the slatted rotor being more localized. Wake visualization studies showed the slat root and tip vortices having a tighter structure on the uniformly refined mesh as compared to the coarse mesh, where they were smeared over a larger region due to the larger spanwise spacing.

3. Based on the results with the uniformly refined mesh, a refined mesh was generated which had spacing near the slat root and tip on the main blade comparable to the blade and slat tip spacing. The objective was to capture the slat root and tip vortices in a more accurate manner. The number of points in the normal and wraparound directions for this refined mesh remained the

same as for the coarse mesh, to limit the computational expense.

4. Results with the refined mesh showed that the performance of the slatted rotors compared favorably with that from the baseline UH-60A rotor at the higher collective angles while incurring a slight performance penalty at a moderate collective setting. Among the two slat configurations, the S-6 performed better at the higher collectives while the S-1 had a higher figure of merit at the moderate collective angle. The slatted rotor can therefore be operated with the slat in the S-1 position at low thrust conditions and with the slat moved to the S-6 position when there is a requirement for high thrust.

5. It was observed that at the moderate collectives, the S-6 slat had a negative contribution to the rotor lift whereas the S-1 slat has an almost zero contribution. This was due to the low local effective angle of attack, which is a combination of the collective, elastic twist and induced inflow angles. As the collective angle was increased, both the slats contributed positively to the lift. This combined with the slightly higher drag in the slatted regions for both the slats, explained the observed performed degradation at the moderate to low collectives.

6. A drop in figure of merit was observed for all rotors at the highest collective setting, as expected. An investigation of the surface streamlines revealed the presence of a shock induced flow separation near the blade tip, outboard of the slat tip. The tip separation combined with the operation of the slatted sections at angles of attack of well below the static stall angle of the baseline

airfoil limits the effectiveness of LE slats to improve performance or extend stall boundaries in hover.

5.3   Future Work

The existing CFD framework is a reliable tool to predict the aerodynamics of hovering rotors. However, there remains a significant amount of work that needs to be undertaken to completely evaluate the LE slat as a viable rotorcraft concept. Some of the suggestions in this section are applicable both for forward flight analysis as well as hover.

- The LE slats are attached to the main blade element by some form of strut supports. To accurately quantify the effect of the LE slats on rotor aerodynamics, it is essential to accurately model the strut supports. Lorber et al. [25] state that the strut supports can add significantly to the rotor drag and account for this by using estimates obtained from 2-D drag coefficient for simple cross sections. However, in addition to the strut profile drag, there is also an interactional drag component between the strut and airfoil/slat, which can be significant in yawed flow. To accurately capture all of these effects, the strut attachment should ideally be modeled as another component in the CFD solution process, similar to the slat/main element.

- It was observed that the assumption of fully turbulent flow resulted in over-prediction of drag at low angles of attack and a delay in stall prediction, for the 2-D slatted sections. It is reasonable to expect that the same assumption

in 3-D can have an impact on the rotor power computations, given that a significant portion of the flow over the slat is expected to be laminar and the 40% spanwise extent of the slat. Accurate prediction of laminar-turbulent transition is an active research topic in the field of external aerodynamics and it is expected that incorporating a validated transition model into the CFD solution process can have a significant bearing on the results.

- In addition to affecting the spanwise distribution of normal force (lift) and chord force (drag), the LE slats also affect the pitching moment distribution across the rotor span. It was observed in the 2-D simulations that the increased maximum lift from slatted sections comes at the price of an increased nose-down pitching moment across the angle of attack range. Such differences in aerodynamic force distribution between the baseline and slatted rotors can result in significantly different structural response as well. Therefore, it is suggested that future simulations be run in a fully coupled CFD-CSD mode, preferably with modifications to the structural model to account for the presence of the LE slat. This would also allow for a more meaningful comparison between the two rotors, since the coupled simulation usually requires trimming the rotors to achieve a desired flight condition.

- The effect of the slat root and tip vortices on the main blade element is not restricted to hovering flight. The leading edge slats were envisioned as a device to mitigate the phenomenon of dynamic stall and therefore to more accurately quantify the capabilities of LE slats, it is suggested that refined mesh, similar

to ones employed in this work, be used for forward flight analysis as well. Using these refined meshes and performing a series of thrust and advance sweeps would quantify the effect of the LE slats on the helicopter flight envelope.

Bibliography

[1] Bousman, W. G., "Airfoil Dynamic Stall and Rotorcraft Maneuverability," NASA/TM-2000-209601, AFDD/TR-00-A-008, NASA Technical Memorandum, July 2000.

[2] McHugh, F.J., "What Are The Lift and Propulsive Force Limits at High Speed For the Conventional Rotor," American Helicopter Society International 34th Annual Forum Proceedings, 1978.

[3] McCloud, J. L. III and McCullough, G. B., "Wind-Tunnel Tests of a Full-Scale Helicopter Rotor with Symmetrical and with Cambered Blade Sections at Advance Ratios from 0.3 to 0.4," NASA TN 4367, September 1958.

[4] Leishman, J. G., "Principles of Helicopter Aerodynamics," Cambridge University Press, 2002.

[5] McCroskey, W. J., McAlister, K. W., Carr, L. W. and Pucci, S. L., "An Experimental Study of Dynamic Stall on Advanced Airfoil Sections Volume 1. Summary of Experiments," NASA TM 84245, July 1982.

[6] McAlister, K. W., Pucci,S. L., McCroskey,W. J. and L. W. Carr, "An Experimental Study of Dynamic Stall on Advanced Airfoil Sections Volume 2. Pressure and Force Data," NASA TM 84245, September 1982.

[7] Carr, L.W, McCroskey, W. J., McAlister, K. W., Pucci, S. L. and Lambert, O., "An Experimental Study of Dynamic Stall on Advanced Airfoil Sections Vol-

ume 3. Hot-Wire and Hot-Film Measurements," NASA TM 84245, December 1982.

[8] Martin, P. B., McAlister, K. W., Chandrasekhara, M. S., and Geissler, W., "Dynamic Stall Measurements and Computations for a VR-12 Airfoil with a Variable Droop Leading Edge", American Helicopter Society 59th Annual Forum, Phoenix, Arizona, May 6-8, 2003.

[9] Chandrasekhara, M. S.,"Fluid Mechanics of Compressible Dynamic Stall Control using Dynamically Deforming Airfoils," Final Report, U.S. Army Research Office, NAVAL Postgraduate School, Monterey, CA, Dec 4, 2001.

[10] Sahin, M., Sankar, L. N., Chandrasekhara, M.S., and Tung, C., "Dynamic Stall Alleviation Using a Deformable Leading Edge Concept–A Numerical Study," *Journal of Aircraft*, Vol. 40, No. 1, Jan. – Feb., 2003, pp. 77–85.

[11] Ekaterinaris, J. A., "Numerical Investigations of Dynamic Stall Active Control for Incompressible and Compressible Flows," *Journal of Aircraft*, Vol. 39, No. 1, Jan. – Feb., 2002, pp. 71–78.

[12] Karim, M., and Achyara, M., "Control of the Dynamic Stall Vortex Over a Pitching Airfoil by Leading Edge Suction," AIAA Paper 1993- 3267, July 1993.

[13] Gerontakos, P., and Lee, T., "Dynamic Stall Flow Control via a Trailing-Edge Flap," *Journal of Aircraft*, Vol. 44, No. 3, Mar., 2006, pp. 469–480.

[14] Davis, G., Feszty, D., and Nitzsche, F., "Trailing edge flow control for the mitigation of dynamic stall effects," 31st European Rotorcraft Forum, European Rotorcraft Forum, Florence, Italy, September 12-16 2005.

[15] Mishra, A. and Sitaraman, J. and Baeder, J. and Opoku, D. G., "Computational Investigation of Trailing Edge Flap for Control of Vibration," 25th AIAA Applied Aerodynamics Conference, Miami, Florida, June 25-28, 2007.

[16] Smith, A. M. O., "High-Lift Aerodynamics," *Journal of Aircraft*, Vol 12, No. 6, June 1975, pp. 501–530.

[17] McAlister, K. W., and Tung, C., "Suppression of Dynamic Stall with a Leading-Edge Slat on a VR-7 Airfoil," NASA Technical Paper 3357 and ATCOM Technical Report 92-A0-013, March 1999.

[18] Carr, L. W., and McAlister, K., "The Effect of a Leading Edge Slat on the Dynamic Stall of an Oscillating Airfoil," AIAA/AHS Aircraft Design Systems and Operation Meeting, 1983, AIAA-83-2533.

[19] Noonan, K. W., Allison, D. O., and Stanaway, S., "Investigation of a Slotted Rotorcraft Airfoil at Mach Numbers from 0.20 to 0.88 at Full-Scale Rotor Reynolds Number.," AHS Aeromechanics Specialist's Conference, San Francisco, CA, January 1994.

[20] Noonan, K. W., Yeager, J. W. T., Singleton, J. D., Wilbur, M. L., and Mirick, P. H., "Evaluation of Model Helicopter Main Rotor Blade with Slotted Airfoils

at the Tip," Proceedings of the 55th Annual Forum of the American Helicopter Society, Montreal,Quebec, Canada, May 25-27 1999.

[21] Carr, L. W., Chandrasekhara, M. S., Wilder, M. C., and Noonan, K. W., "Effect of Compressibility on Suppression of Dynamic Stall using a Slotted Airfoil," *Journal of Aircraft*, Vol. 38, No. 2, April 2001, pp. 296–301.

[22] Narramore, J., McCroskey, W. J., and Noonan, K. W. "Design and Evaluation of Multi-Element Airfoils for Rotorcraft," Proceedings of the 55th Annual Forum of the American Helicopter Society, Montreal, Quebec, Canada, May 25 - 27 1999.

[23] Buning, P.G., Jesperson, D.C., Pulliam, T.H., Chan, W.M., Slotnick, J.P., Krist, S.E., and Renze, K.J., "OVERFLOW User's Manual, Version 1.8g," NASA Langley Research Center, Moffet Field, CA., March 1999.

[24] Yeo, H., and Lim, J. W., "Application of a Slotted Airfoil for UH-60 A Helicopter Performance," Proceedings of The American Helicopter Society Aerodynamics,Aeroacoustics, and Test and Evaluation Technical Specialists Meeting, San Francisco, CA, January 23-25 2002.

[25] Lorber, P. F., Bagai, A., and Wake, B. E., "Design and Evaluation of Slatted Airfoils for Improved Rotor Performance," 62nd Annual Forum and Technology Display of the American Helicopter Society International, Phoenix, AZ, May 9-11 2006.

[26] Cole, S. R., and Rivera, J. R., "The New heavy Gas Testing capabilities in the NASA Langley Transonic Dynamics Tunnel," Royal Aeronautical Society Wind Tunnel and Wind Tunnel Test Techniques Forum, Paper 4, April 1997.

[27] Mishra, A., "A Coupled CFD/CSD Investigation of the Effects of Leading Edge Slat on Rotor Performance," Ph.D. Dissertation, Department of Aerospace Engineering, University of Maryland at College Park, 2012.

[28] Bousman, W. G. and Kufeld, R. M., "UH-60A Airloads Catalog," NASA/TM-2005-212827, August 2005.

[29] Kufeld, R. M., D. L. Balough, J. L. Cross, K. F. Studebaker, C. D. Jennison, and W. G. Bousman, "Flight Testing the UH60A Airloads Aircraft," 50th Annual Forum of the American Helicopter Society International, Washington, D.C., 1994.

[30] Lorber, P.F., Stauter, R.C., and Landgrebe, A.J., "Comprehensive Hover Test of the Airloads and Airflow of an Extensively Instrumented Model Helicopter Rotor," Proceedings of the 45th Annual American Helicopter Society Forum, Boston, MA, May 1989.

[31] Lorber, P.F., "Aerodynamic results of a Pressure-Instrumented Model Rotor Test at the DNW," *Journal of the American Helicopter Society*, Vol. 41, No. 1, January 1996, pp. 7-17.

[32] Shinoda, P.M., Yeo, H., and Norman, T.R., "Rotor Performance of a UH-60 Rotor System in the NASA Ames 80-by 120-Foot Wind Tunnel," Proceedings

119

of the 58th Annual American Helicopter Society Forum, Montreal, Canada, June 11-13, 2002.

[33] Norman, T.R., Shinoda, P., Peterson, R.L., and Datta, A., "Full-Scale Wind Tunnel Test of the UH-60A Airloads Rotor", 67th Annual Forum of the American Helicopter Society, Virginia Beach, VA, May 2011

[34] Egolf, T.A., and Sparks, S.P., "A Full Potential Flow Analysis with Realistic Wake Influence for Helicopter Rotor Airload Prediction," NASA CR-4007, 1987.

[35] Agarwal, R.K., and Decse, J.E., "Euler Calculations for a Flowfield of a Helicopter Rotor in Hover," *Journal of Aircraft*, Vol. 24, No. 4, April 1987, pp. 231-238.

[36] Wake, B.E., and Sankar, N.L., "Solutions of the Navier-Stokes Equations for the Flow About a Rotor Blade," *Journal of the American Helicopter Society*, Vol. 34, No. 2, April 1989, pp. 13-23.

[37] Srinivasan, G.R., Baeder, J.D., Obayashi, S., and McCroskey, W.J., "Flowfield of a Lifting Hovering Rotor - A Navier-Stokes Simulation," Proceedings of the Sixteenth European Rotorcraft Forum, Glasgow, Scotland, September 1990.

[38] Srinivasan, G.R., Raghavan, V., Duque, E.P.N., and McCroskey, W.J., "Flowfield Analysis of Modern Helicopter Rotors in Hover by Navier-Stokes Method," AHS Specialists Meeting on Rotorcraft Acoustics and Rotor Fluid Dynamics, Philadelphia, PA, October 1991.

[39] Wake, B.E., and Baeder, J.D., "Evaluation of a Navier-Stokes Analysis Method for Hover Performance Prediction," *Journal of the American Helicopter Society*, Vol. 41 No.1, January 1996, pp. 1-17.

[40] Strawn, R.C., and Ahmad, J., "Computational Modeling of Hovering Rotors and Wakes," 38th AIAA Aerospace Sciences Meeting and Exhibit, Reno, NV, 10-13 January 2000, AIAA Paper 2000-0110.

[41] Strawn, R.C., and Djomehri, M.J., "Computational modeling of Hovering Rotor and Wake Aerodynamics," *Journal of Aircraft*, Vol. 39 No. 5, Sept-Oct 2002. pp. 786-794.

[42] White, F. M., "Viscous Fluid Flow," McGraw-Hill, 1991.

[43] Srinivasan, G. R., and Baeder, J. D., "TURNS: A Free-wake Euler/ Navier-Stokes Numerical Method for Helicopter Rotors," *AIAA Journal*, Vol. 31, No. 5, May 1993, pp. 959–961.

[44] Lakshminarayan, V. K., "Computational Investigation of Micro-Scale Coaxial Rotor Aerodynamics in Hover," Ph.D. Dissertation, Department of Aerospace Engineering, University of Maryland at College Park, 2009.

[45] Duraisamy, K., Sitaraman, J., and Baeder, J.D., "High Resolution Wake Capturing Methodology for Accurate Simulation of Rotor Aerodynamics," 61st Annual Forum of the American Helicopter Society, Dallas, Texas, June 8-11, 2005.

[46] Van Leer, B., "Towards the Ultimate Conservative Difference Scheme V. A Second-Order Sequel To Godunov's Method," *Journal of Computational Physics,* Vol. 135, No. 2, August 1997, pp. 229–248.

[47] Koren, B., "Upwind Schemes, Multigrid and Defect Correction for the Steady Navier-Stokes Equations," Proceedings of the 11th International Conference on Numerical Methods in Fluid Dynamics, Willamsburg, VA, June 1988.

[48] Roe, P., "Approximate Riemann Solvers, Parameter Vectors and Difference Schemes," *Journal of Computational Physics,* Vol. 135, No. 2, August 1997, pp. 250–258.

[49] Hoffman, K. A., and Chiang, S. T., "Computational Fluid Dynamics, Vol. 2," EES Books, 2000.

[50] Jameson, A., and Yoon, S., "Lower-Upper Implicit Schemes with Multiple Grids for Euler Equations," *AIAA Journal,* Vol. 25, No. 7, July 1987, pp. 929-935.

[51] Yoon, S. and Jameson, A., "Lower-Upper Symmetric-Gauss-Seidel Method for Euler and Navier-Stokes Equations," AIAA Journal, Vol.26, 1988, pp. 1025-1026.

[52] Pulliam, T., "Time Accuracy and the use of Implicit Methods," 11th AIAA Computational Fluid Dynamics Conference, AIAA Paper 1993-3360, Orlando, FL, July 1993.

[53] Baldwin, B., and Lomax, H., "Thin Layer approximation and Algebraic Model for Separated Flows," 16th AIAA Aerospace Sciences Meeting, AIAA paper 1978-257, Huntsville, AL, January 1978.

[54] Durbin, P., "A Reynolds Stress Model for Near Wall Turbulence," *Journal of Fluid Mechanics,* Vol. 249, 1993, pp. 465-498.

[55] Srinivasan, G.R., Ekaterinaris J. A., and McCroskey, W.J., "Evaluation of Turbulence Models for Unsteady Flows of an Oscillating Airfoil," *Computers and Fluids,* Vol. 24, No. 7, 1995, pp. 833–861.

[56] Spalart, P. R. and Allmaras, S. R., "A One Equation Turbulence Model for Aerodynamics Flow," AIAA Paper 1992-0439, 1992.

[57] Steger, J.L., and Chausee, D.S., " Generation of Body-Fitted Coordinates using Hyperbolic Partial Differential Equations," *SIAM Journal of Scientific and Statistical Computing*, Vol. 1, No. 4, December 1980, pp 431-437.

[58] Sitaraman, J., "CFD Based Unsteady Aerodynamic Modeling for Rotor Aeroelastic Analysis," Ph.D. Dissertation, Department of Aerospace Engineering, University of Maryland at College Park, 2003.

[59] Steger, J.L., Dougherty, F.C. and Benek, J.A., "A Chimera Grid Scheme," Advances in Grid Generation, ASME FED-Vol. 5, June, 1983.

[60] Gupta, V., "An Investigation of Quad Tilt Rotor Aerodynamics in Helicopter mode", Ph.D. Dissertation, Department of Aerospace Engineering, University of Maryland at College Park, 2005.

[61] Lee, Y., "On Overset Grids Connectivity and Automated Vortex Tracking in Rotorcraft CFD," Ph.D. Dissertation, Department of Aerospace Engineering, University of Maryland at College Park, 2008.

[62] Jose, A.I., "Investigation into the Aerodynamics of Swashplateless Rotor usign CFD-CSD Analysis," Ph.D. Dissertation, Department of Aerospace Engineering, University of Maryland at College Park, 2012.

[63] Hirsch, C., "Numerical Computation of Internal and External Flows, Volume 2," Wiley Publishers, 1990.

[64] Medida, S., and Baeder, J.D., "Numerical Prediction of Static and Dynamic Stall Phenomena using the $\gamma - \overline{Re_{\theta t}}$ Transition Model", 67th Annual Forum of the American Helicopter Society, Virginia Beach, VA, May 3-5 2011.

[65] Chopra, I. and Bir, G., "University of Maryland Advanced Rotor Code: UMARC," American Helicopter Society Aeromechanics Specialists Conference, San Francisco, January, 1994.

[66] Schmitz, S., Bhagwat. M., Moulton, M.A., Caradonna, F.X., and Chattot, J.J., "The Prediction and Validation of Hover Performance and Detailed Blade Loads," *Journal of the American Helicopter Society*, Vol. 54, No. 3, July 2009.